UNIVERSITY OF CALIFORNIA

SANTA CRUZ

HIGH-PEAK AND AVERAGE POWER DEEP ULTRAVIOLET ULTRASHORT PULSE FIBER LASER SYTEM

A thesis submitted in partial satisfaction
of the requirements for the degree of

MASTER OF SCIENCE

in

ELECTRICAL ENGINEERING

by

Madison Wayne Perry

June 2018

The Thesis is approved:

_____
Professor Marco Rolandi

_____
Professor Holger Schmidt

_____
Professor Ali Yanik

_____
Tyrus Miller
Vice Provost and Dean of Graduate Studies

Table of Contents

Abstract

HIGH-PEAK AND AVERAGE POWER DEEP ULTRAVIOLET ULTRASHORT PULSE FIBER LASER SYTEM

Madison Wayne Perry

The overall aim of this project was to design, develop and demonstrate the highest average and peak power, Ultrashort-Pulse, Deep Ultraviolet Fiber Laser system. Our objective was to combine the robustness of a fiber laser with the production of deep UV radiation by fourth harmonic generation. By producing >100 MW class pulses with a M^2<1.3 at a repetition rate of >100 kHz, such a system provides a new and unique capability for nonlinear optics, femtosecond (non-thermal) laser machining and other nonlinear phenomena. The deep UV output enables a host of processes resulting from the ability to achieve high irradiance with 4.7 eV photons. The development, theoretical description, and performance of the entire laser system including operation at the fundamental, 2^{nd}, and 4^{th} harmonics is described. While we could achieve an average power exceeding 5.4 W, pulse broadening in the UV resulted in lower peak power. Our highest average power while maintaining a peak power above 100 MW was 4.8 W at 100 kHz with 400 fsec pulses at 262 nm. To our knowledge, this is the highest peak power fiber laser system operating below 300 nm ever reported.

Initial beam quality was excellent but would degrade after minutes of operation due to the formation of color centers. A number of limitations were observed including two-photon absorption (giving rise to color centers), self-phase modulation, continuum generation and filamentation. These phenomena are investigated and the impact on achieving an operational system are discussed.

The first two chapters of this thesis outline the system as a whole and give a comparison to solid state lasers using bulk gain material. Chapter 3 starts with the fiber seed oscillator that begins the chirped-pulse amplification (CPA) system. It presents all the starting parameters for modeling the pulse train and seed characteristics as well as spectral bandwidth etc. Design considerations at 1030nm vs 1047nm for the CPA system are discussed. Chapter 4 presents theory, modeling and simulation of fiber dispersion and amplification including the use of photonic crystal amplifiers. Chapter 5 discusses compressor design. This includes various compressor grating mounting schemes and analysis and comparison of different compressor options. Chapter 6 focuses on harmonic generation at 2ω and 4ω as well as crystal selection and phase matching analysis. Decisions between critical and noncritical phase matched harmonic generation is considered. Various crystals are also considered and an analysis of BBO, LBO and CLBO is presented for nanosecond and femtosecond pulses. The remaining chapters provide experimental measurements of pulse train, laser output power, pulse spectrum, pulse duration, etc. Experimental measurements are compared to numerical models throughout.

Acknowledgements

Thank you to all my professors over the years who have helped push me and open doors for me to gather as much knowledge and experience as possible. I am grateful for the all support I received to enable this project. Prof. Joel Kubby and Marco Reinig taught me adaptive optics and supported this thesis effort. With great sadness, Prof. Kubby passed away in the last few months of this work. He worked with me and provided advice to the last week. Prof Shaya Feinman and Andrew Grieco provided the laboratory and technical support at UCSD. Special thanks to the scientists at the Fraunhofer Institute and Active Fiber Systems (AFS) for their help and advice on fiber lasers. AFS, MenloSystems and the Fraunhofer Institute provided many of the components used in the fiber section.

My family made my education and this work possible. My appreciation for their continuing support over these many years is beyond words. Mom was always there for me with disregard for my many transgressions. Austin, Summer and Amanda would always pick me up in times of despair. I would especially like to thank my dad who pushed me to learn and excel. He has taught me more than anyone about physics, optics and science in general my entire life. He taught me the value of integrity, hard work and to always strive for quality.

Finally I would like to thank my girlfriend, Amanda and our many dogs for helping me hold fast through the years to get here today. The completion of this thesis has been possible only through your support.

1. Introduction to High Power Laser

Fiber lasers have also undergone remarkable advancement over the past 2 decades. Diode-pumped single-mode, continuous wave (CW) fiber lasers have now reached >2 kW output. (1) However, the application of fiber lasers to high-peak power is limited by laser damage and a number of nonlinear processes: self-phase modulation, Raman generation, Stimulated Brillouin Scattering (SBS). (2) Similar to bulk gain media, the application of Chirped Pulse Amplification to fiber lasers enables amplification to the nonlinear limit of the *stretched* pulse with the fiber. (3,4) An external pulse compressor then increases the peak power by compressing the pulse to (ideally) the transform limit of the spectrum emerging from the fiber. With this method pulses > 100uJ and <100 fsec duration have been achieved. (5-8) Recently, photonic crystal amplifiers exhibiting effective core diameters >40 microns have emerged which increase the output of these "quasi-fiber" systems to 500 uJ per pulses. At 100 kHz, repletion rate, these systems can achieve 50 W class average power. (9-11)

In parallel with the revolution in fiber and photonic crystal amplifiers has been the revolution in diode-pumped (bulk) solid-state lasers. CW lasers approaching 150 kW have been produced with good beam quality. (17) Using such lasers as amplifiers of fiber and photonic crystal based chirped-pulse amplification systems offers the potential for kilowatt class average power ultrashort-pulsed laser systems with peak power exceeding a terawatt. The high-peak power of such systems enables a new approach to the generation of high-average power, short-wavelength coherent radiation by harmonic conversion.

In this project, I design, model and build a fiber/photonic crystal based "Front-End" of such a system. This front-end system consists of a fiber master oscillator, pulse stretcher, fiber amplifier, optical relay, multi-stage fiber amplifier, multi-stage photonic crystal amplifier, pulse compressor and output adaptive optics system. We then utilize this system to generate deep ultraviolet radiation at an average and peak power not previously achieved. With the high beam quality, we achieve the highest average power irradiance produced from a fiber laser to date.

2. Theory of Nonlinear Optics

All electromagnetic phenomena are governed by Maxwell's equations. (12-21)

$$\nabla \times \vec{E} = -\frac{\partial \vec{B}}{\partial t}$$

$$\nabla \times \vec{H} = \vec{J} + \frac{\partial \vec{D}}{\partial t}$$

$$\nabla \cdot \vec{D} = \rho_f$$

$$\nabla \cdot \vec{B} = 0$$

Here ***E*** and ***H*** are the electromagnetic field vectors and ***D*** and ***B*** are the corresponding displacement and magnetization fields. ***D*** and ***B*** are often referred to as the macroscopic fields because they reflect the effect from matter and electromagnetic microscopic field interaction. $\boldsymbol{J}_f$ and ρ_f are the current and charge densities, respectively. For conventional propagation in dielectric media there are no free charges so we will set ρ_f and $\boldsymbol{J}_f$ to zero. Therefore we have the following equations:

$$\nabla \times \vec{H} = \frac{\partial \vec{D}}{\partial t}$$

$$\nabla \cdot \vec{D} = 0$$

Displacement and magnetic fields, also known as Flux densities ***D*** and ***B*** arise as a response to the electric and magnetic fields ***E*** and ***H*** propagating inside the medium and are related by:

$$\vec{D} = \epsilon_o \vec{E} + \vec{P}$$

$$\vec{B} = \mu_o \vec{H} + \vec{M}$$

where ε_o is the vacuum permittivity and, μ_o is the vacuum permeability. ***P*** and ***M*** are the induced electric and magnetic polarizations. In this case ***M*** = 0 because we are working with nonmagnetic media. By taking the curl of the curl of the electric field and combining it with the result of the curl of the magnetic field we can obtain,

$$\nabla \times \nabla \times \vec{E} = \nabla \times (-\frac{\partial \vec{B}}{\partial t})$$

$$\nabla \times \nabla \times \vec{E} = \frac{\partial (\nabla \times \mu_o \vec{H})}{\partial t}$$

$$\nabla \times \nabla \times \vec{E} = \frac{\partial}{\partial t}(\mu_o \frac{\partial \vec{D}}{\partial t})$$

If we recall that the displacement field ***D*** arises as a response to electric fields, then we can substitute the electric and polarization vectors ***E*** and ***P*** into ***D***. We must also remember that divergence of ***D*** can be written as the divergence of the sum of the electric field and polarization vectors which allows us to make this substitution.

$$\nabla \cdot \vec{D} = \nabla \cdot (\epsilon_o \vec{E} + \vec{P}) = 0$$

Pushing the second time derivative into the parenthesis, using $\varepsilon_o \mu_o = 1/c^2$, and noting the time-independence of the vacuum permeability, we obtain,

$$\nabla \times \nabla \times \vec{E} = -\frac{1}{c^2}\frac{\partial^2 \vec{E}}{\partial t^2} - \mu_o \frac{\partial^2 \vec{P}}{\partial t^2}$$

We can write the electric field as a summation of multiple monochromatic plane waves, also known as the monochromatic wave approximation. The polarization can also be written in a series separating the linear and nonlinear parts.

$$\vec{E}(r,t) = \sum_{n=0}^{\infty} \vec{E_n} \cdot e^{i(k_n \cdot r - \omega_n t)}$$

$$\vec{P}(r,t) = \vec{P_{Linear}}(r,t) + \vec{P_{Nonlinear}}(r,t)$$

$$\sum_{n=0}^{\infty} \vec{P_n}(r,t) = \sum_{n=0}^{\infty} \vec{P_L} \cdot e^{i(k_n \cdot r - \omega_n t)} + \sum_{n=0}^{\infty} \vec{P_{NL}} \cdot e^{i(k_n \cdot r - \omega_n t)}$$

Utilizing the identity,

$$\nabla \times \nabla \times \vec{E} = -\nabla^2 \vec{E} + \nabla(\nabla \cdot \vec{E})$$

we obtain,

$$\nabla^2 [\sum_{n=0}^{\infty} \vec{E_n} \cdot e^{i(k_n \cdot r - \omega_n t)}] + \frac{1}{c^2} \frac{\partial^2}{\partial t^2} [\sum_{n=0}^{\infty} \vec{E_n} \cdot e^{i(k_n \cdot r - \omega_n t)}] = -\mu_o \frac{\partial^2}{\partial t^2} [\sum_{n=0}^{\infty} P_N(\vec{r}, t)$$

where $\boldsymbol{P_n}$ represents the nonlinear polarization of the medium. (15) We can write $\boldsymbol{P_n}$ as a nonlinear polarization from the product of $E_1 + \ldots E_n$. This produces a series of n equations for n fields. It should be noted that while $\omega = \omega_v$ due to photon energy conservation in steady state, $\boldsymbol{k}_n$ need not be exactly equal to $\boldsymbol{k}$ since wave momentum conservation is not strictly required in a finite medium (13). The various waves $\boldsymbol{E_n}$ are coupled through the nonlinear polarization (e.g., nonlinear wave mixing in crystals and propagation in fibers). Through nonlinear coupling, energy can be transferred back and forth between waves. The larger $\boldsymbol{P_{NL}}$ is, the larger the effect will be. This approach of

coupled wave interaction was first addressed by Armstrong et al for describing wave interaction in nonlinear optics.

Taking the above derivatives and using the plane wave approximation, we obtain,

$$\nabla^2 \vec{E_n}(r,\omega) = -\omega^2 \mu_o \cdot (\epsilon_o \vec{E_n}(r,\omega) + \vec{P_n}(r,\omega))$$

As mentioned above, this equation is for a summation over *n* many plane waves. Focusing on a single term, we have,

$$\nabla^2 \vec{E}(r,\omega) = \omega_o^2 \mu_o [\epsilon_o \vec{E}(r,\omega) + \vec{P}_{NL}(r,\omega)]$$

Noting that the polarization may be written,

$$\vec{P}(r,\omega) = \vec{P}_{Linear}(r,\omega) + \vec{P}_{Nonlinear}(r,\omega)$$

$$\vec{P}(r,\omega) = \epsilon_o \chi^{(1)} \cdot \vec{E}(r,\omega) + \vec{P}_{Nonlinear}(r,\omega)$$

$$\epsilon = \epsilon_o (1 + \chi^{(1)})$$

Where the permittivity of the medium is the sum of the vacuum permittivity and the linear response of the medium. (15) The linear refractive index, $n = [\varepsilon/\varepsilon_o]^{1/2} = [1+ \chi^1]^{1/2}$. These varying orders give rise to effects like harmonic generation, dispersion, self-phase modulation, self-focusing etc.

$$\nabla^2 \vec{E}(r,\omega) = -\omega^2 \mu_o [\epsilon \cdot \vec{E}(r,\omega) + \vec{P}_{Nonlinear}(r,\omega)]$$

$$\vec{P}_{Nonlinear}(r,\omega) = P^{(2)} + P^{(3)} + P^{(4)} + P^{(5)} + \ldots$$

$$\vec{P}_{Nonlinear}(r,\omega) = \sum_{n=2}^{\infty} P^{(n)}(r,\omega,k_n) = \sum_{n=2}^{\infty} \chi^{(n)} : E_1 E_n$$

Rewriting the nonlinear polarization in a power series expansion of ***E*** and substituting it back into the nonlinear wave equation we obtain the following equation:

$$\nabla^2 \vec{E}(r,\omega) = -\omega^2 \mu_o [\epsilon \cdot \vec{E}(r,\omega) + \sum_{n=2}^{\infty} \chi^{(n)} : E_1 E_n]$$

Linear susceptibility is responsible for the linear optical properties of the medium such as refraction, dispersion, absorption, and birefringence. Second and third order nonlinear susceptibilities describe three and four wave mixing, respectively. Second order susceptibility is responsible for second harmonic generation, sum and difference frequency generation, and optical parametric amplification. These effects all are based on the combining of two waves to produce a third wave. The equations below describe monochromatic plane wave mixing which we will use as the start for later chapters where we adapt a more accurate slowly varying amplitude pulse approximation. In this notation ***E₁ E₂*** are the first two red waves with ***E₃*** being the resulting blue wave. These three equations govern nonlinear mixing within crystals that lack inversion symmetry. Parametric amplification can also be derived from these equations. (16) In this process the bluer stronger wave (pump) is split into two signal and idler beams conserving energy and momentum with $\omega_3 = \omega_2 + \omega_1$.

$$\vec{P}(\omega_3) = \epsilon_o \chi(-\omega_3;\omega_3) \cdot \vec{E}(\omega_3) + \epsilon_o \chi(-\omega_3;\omega_1,\omega_2) \cdot \vec{E}_1(\omega_1)\vec{E}_2(\omega_2)$$

$$\nabla^2 \vec{E}_1 = \omega_1^2 \mu_o [\epsilon \cdot \vec{E}_1 + \epsilon_o \chi^{(2)}(-\omega_1;\omega_3,-\omega_2) \cdot \vec{E}_3 \vec{E}_2^*]$$

$$\nabla^2 \vec{E}_2 = \omega_2^2 \mu_o [\epsilon \cdot \vec{E}_2 + \epsilon_o \chi^{(2)}(-\omega_2;\omega_3,-\omega_1) \cdot \vec{E}_3 \vec{E}_1^*]$$

$$\nabla^2 \vec{E}_3 = \omega_3^2 \mu_o [\epsilon \cdot \vec{E}_3 + \epsilon_o \chi^{(2)}(-\omega_3;\omega_1,\omega_2) \cdot \vec{E}_1 \vec{E}_2]$$

Third order nonlinearities include effects such as third harmonic generation, optical Kerr effect, Raman effects and Brillouin scattering. The last two effects are taken from the imaginary terms when absorption is considered. In general, similar to second order effects, three waves will interact to produce a fourth wave. χ^3 is therefore also considered a four photon process. Optical Kerr effect is an intensity dependent refractive index effect that arises from third order nonlinearity. This effect has been utilized by many researchers and companies in the development of Kerr lens mode locking (KLM). In high intensity beams the nonlinear refractive index can be the source of optical damage because it can lead to self-focusing and small-scale ripple growth. (16)

$$\vec{P}(\omega_4) = \epsilon_o \chi^3 \vec{E}(\omega_3)\vec{E}(\omega_2)\vec{E}(\omega_1)$$

$$n_2 = n_0 + (12\pi/n_0)\chi^3 \vec{E}_{av}^2$$

Stimulated Raman Scattering and Brillouin Scattering also arise as effects from third order nonlinearity. Raman scattering results from the interaction of a laser beam with molecular vibrations. In the presence of a strong external electric field, the charge distribution of a molecule is polarized. (16) The molecule then acquires a dipole that will interact with the driving electric field. The resulting field radiates at $\omega = \omega_o \pm \omega_s$ where ω_s is the frequency of the molecular polarization (Stokes shift). Brillouin scattering deals with the process of an optical beam interacting with an acoustic wave in the medium. The acoustic wave is associated with the propagation of pressure in the medium which leads to periodic density fluctuations. Electrostriction provides the coupling mechanism between the acoustic wave and the electromagnetic wave resulting in a local compression

of the medium in response to the strength of the electric fields. The Brillouin shift is given by, (16)

$$v_B = \frac{2nv_a}{\lambda}$$

Self-phase modulation will also become increasingly important when we discuss photonic crystal amplifiers in later chapters. This is one of the consequences of the optical Kerr effect where a wave in a fiber experiences a nonlinear phase delay resulting from its own intensity. Self-phase modulation is given by, (2)

$$\omega = \omega_o - \frac{\partial \phi}{\partial t}$$

where the phase, $\phi(t)$ is, itself a function of the incident intensity,

$$\phi(t) = \frac{2\pi}{\lambda} \int \gamma I(r,t) dz$$

and γ is the nonlinear refractive index. The integral is often referred to as the B-Integral. (2) The nonlinear refractive index gives rise to both self-phase modulation (time-derivative of the phase) and self-focusing. Self-focusing results from the spatial distribution of intensity, I(r), which leads to a position-dependent phase.

2.a. Nonlinear Fiber Optics

In the previous section we derived the nonlinear wave mixing equations to describe the effects of the χ^2 polarizations. Here we will derive the χ^3 nonlinear propagation equations and discuss the various effects that a pulse undergoes as it propagates down an optical fiber. Most nonlinear effects in optical fibers usually involve pulse durations ranging from ~10fs to 10ns. (1-81) As the pulse propagates in a fiber it

will undergo dispersive and nonlinear effects that will both effect of the spectrum and duration of the pulse. Direct third-order harmonic conversion, $3\omega_o$ is negligible in optical fibers due to the low value of χ^3 $(3\omega{:}\omega_o, \omega_o, \omega_o)$ and the requirement for phase matching.

Starting with the nonlinear wave equation we have: (15)

$$\nabla^2[\sum_{n=0}^{\infty}\vec{E_n}\cdot e^{i(k_n\cdot r-\omega_n t)}]+\frac{1}{c^2}\frac{\partial^2}{\partial t^2}[\sum_{n=0}^{\infty}\vec{E_n}\cdot e^{i(k_n\cdot r-\omega_n t)}]=-\mu_o\frac{\partial^2}{\partial t^2}[\sum_{n=0}^{\infty}P_N(\vec{r},t)$$

where we have the nonlinear polarization written only in terms of the 3rd order nonlinearity:

$$\vec{P}(\omega_4)=\epsilon_o\chi^3\vec{E}(\omega_3)\vec{E}(\omega_2)\vec{E}(\omega_1)$$

Phase matching and crystal symmetry is not of concern in optical fibers so we can neglect all mixing terms, χ^3 $(\omega{:}\omega_o, \omega_o, \omega_o)$, and write the nonlinear polarization as:

$$P_{NL}=\epsilon_0\epsilon_{NL}E(r,t)$$

Where the nonlinear contribution to the dielectric constant is:

$$\epsilon_{NL}(r,t)=\frac{3}{4}\chi^{(3)}|E(r,t)|^2$$

From here it will be more convenient to work in the Fourier domain due to the frequency dependent nature of the third order nonlinearities. In this case we are concerned for the intensity dependent refractive index as well which will govern the nonlinear responses. We can then write the nonlinear wave equation as the following Helmholtz equation:

$$\nabla^2\widetilde{E}+\epsilon(\omega)k_0^2\widetilde{E}=0$$

that is satisfied with:

$$\epsilon(\omega)=1+\widetilde{\chi}^{(1)}(\omega)+\epsilon_{NL}$$

This is partial differential equation that can be solved with separation of variables where we can assume the traveling pulse has a slowly varying amplitude such that the frequency domain is the Fourier transform of the pulse envelope: (16)

$$\widetilde{E}(r,\omega-\omega_0)=\int_{-\infty}^{\infty}E(r,t)exp[i(\omega-\omega_0)t]dt$$

With the propagation of pulse along the direction z written as:

$$\widetilde{E}(r,\omega-\omega_o)=A(z)exp[ikz]exp[i(\omega-\omega_o)t]$$

We can now take the above equation and plug it into the Helmholtz equation to get the following second order differential equation that describes the varying amplitude of a propagating pulse:

$$\frac{\partial^2A(z)}{\partial z^2}+2ik\frac{\partial A(z)}{\partial z}=-\frac{\omega^2}{\epsilon_0c^2}exp[i(\omega-\omega_o)t]\cdot P_{NL}(z,\omega)exp(-ikz)$$

This is where the slowly varying amplitude approximation is taken such that the second derivative of the change in amplitude with distance is significantly smaller than its first order derivative:

$$|\frac{\partial^2A(z)}{\partial z^2}|<<|2k\frac{\partial A(z)}{\partial z}|$$

Setting $\omega-\omega_o$ equal to a perturbed wavenumber to account for index of refraction variation between the various frequencies. This means that each spectral component within the pulse acquires a varying phase shift with a magnitude which depends on frequency and intensity. Rewriting the slowly varying amplitude approximation in terms of perturbed wavenumber,

$$\frac{\partial A(z)}{\partial z} = i[\beta(\omega) + \Delta\beta(\omega) - \beta_0]A(z)$$

β(ω) is commonly expressed in a Taylor series expanded around the central frequency of the pulse. This expansion is written as:

$$\beta(\omega) = \beta_0 + (\omega - \omega_0)\beta_1 + \frac{1}{2}(\omega - \omega_0)^2\beta_2 + \frac{1}{6}(\omega - \omega_0)\beta_3 + ...$$

This reduces the slowly varying amplitude equation to only the first order derivative in the equation above. Taking the inverse Fourier Transform we can then put the slowly varying amplitude back into the time domain.

$$A(z,t) = \frac{1}{2\pi}\int_{-\infty}^{\infty} \tilde{A}(z, \omega - \omega_0)exp[-i(\omega - \omega_0)t]d\omega$$

When taking the Fourier Transform we can replace w-w_o with the imaginary partial derivative with respect to time operator resulting in an equation for the varying amplitude as a function of distance and time. (14)

$$\frac{\partial A}{\partial z} + \beta_1\frac{\partial A}{\partial t} + \frac{i\beta 2}{2}\frac{\partial^2 A}{\partial t^2} = i\triangle\beta_0 A$$

The Δβ(ω) on the right hand side can be rewritten as a nonlinear term that is dependent on the input intensity, effective area, and frequency and refractive index,

$$\Delta\beta_0 = \gamma(\omega_0)|A^2|, \gamma = \frac{\omega_0 n_2}{cA_{eff}}$$

and we obtain:

$$\frac{\partial A}{\partial z} + \beta_1\frac{\partial A}{\partial t} + \frac{i\beta 2}{2}\frac{\partial^2 A}{\partial t^2} + \frac{\alpha}{2}A = i\gamma(\omega_0)|A^2|A$$

Up until now the Nonlinear Schrodinger equation has been limited to pulses where the spectral width is far smaller than the carrier frequency (slowly-varying amplitude approximation). Chromatic dispersion in the fiber is represented through the parameters

β_1 and β_2, and fiber losses through α. The Kerr effect/nonlinear refractive index is represented by γ. The pulse envelope moves with group velocity equal to $1/\beta_1$ with a dispersion given by β_2. Group Velocity Dispersion (GVD) can be either positive or negative depending on whether the carrier frequency is smaller or larger than the "zero-dispersion" value. In standard silica fibers for example the wavelengths in the visible spectrum will undergo positive group dispersion from ~250 to 1300 nm. Beyond ~1300 nm group-velocity dispersion is negative.

Neglect of wavelength dependent absorption: Limit of $\alpha_1 = 0$

The final limitation is to neglect the wavelength dependence of absorption,

$$\alpha(\omega) = \alpha(\omega_o) + \frac{\partial \alpha}{\partial \omega}\Delta\omega = \alpha(\omega_o) + \alpha_1(\omega_o)\Delta\omega$$

In practical terms, this restricts our analysis to pulses with carrier frequency away from any specific absorption lines in the medium. This results in a third order Nonlinear Schrödinger Equation including where time is connected to the pulse traveling in the medium, (14)

$$T = t - \beta_1 z$$

$$i\frac{\partial A}{\partial z} + \frac{i\alpha}{2}A - \frac{\beta_2}{2}\frac{\partial^2 A}{\partial T^2} = -\gamma|A|^2 A$$

This equation is valid for propagation in dispersive media at irradiance less than the damage threshold (<~10 GW/cm^2) and away from absorption features. This "cubic" nonlinear Schrodinger equation includes first, second, and third order nonlinear polarization effects for both nonlinear crystals and fibers. I will use this NLSE in modeling all parts of the system.

3. Overview of the system

Ultrashort-pulse lasers were first created in dyes in the 1980's followed by femtosecond pulse propagation in fibers. The development of chirped-pulse amplification enabled the creation of terawatt and even petawatt peak power pulses (23-28). Chirped pulse enables amplification to the nonlinear limit of the stretched pulse in the gain material followed by compression to the transform-limit of the spectrum outside of the gain medium. When applied to fiber lasers, CPA has enabled pulses with energy > 250 uJ and durations < 100 fs having been achieved to date. (35) These systems can operate at repetition rates as high as 100kHz resulting in an average power of tens of watts.

Chirped-Pulse Amplification (CPA) in lasers was first demonstrated by the Mourou group at the University of Rochester in 1985 (3). While the bandwidth and energy storage of solid-state lasers offered the potential for Petawatt pulses, the achievable peak power was limited by self-focusing in the solid-state material. Radar amplifiers had experienced peak power limitations due to Child-Langmuir limitations on electric current. This was overcome in the 1970's by the development of chirped-pulse radar amplifiers. In radar CPA, the radiofrequency pulse is stretched in time to enable amplification of a relatively long (microsecond pulse). Following amplification, the pulse is compressed to the nanosecond class. Strickland and Mourou applied the same idea to overcome the self-focusing and damage problem associated with amplifying high peak power, picosecond pulses in solid-state laser materials. (3)

Their experiment started with 150ps pulses at 82MHz from a mode-locked Nd:YAG laser with 5 Watts of average power. The pulses are inserted into a ~1 km long, single-mode silica fiber. The single-mode nature of the fiber prevents self-focusing but

allows self-phase modulation (time-derivative of the nonlinear phase) to occur. (3) The pulse exited the fiber with a spectrum broadened to >3 nm by self-phase modulation and a duration broadened to 700 psec by group velocity dispersion (GVD) in the fiber. The average power was reduced to 2.3 W at the exit of the fiber. The ~30 nJ pulse entered a Nd:glass regenerative amplifier. The regenerative amplifier enabled multi-pass amplification to ~2 mJ. Gain narrowing in the regenerative amplifier limited the pulse spectrum to ~1.5 nm and reduced the stretched pulse duration to 300ps. The stretched pulses were then sent to a grating pair with 1700 lines/mm groove spacing used in Littrow condition. The use of the double pass grating system also allows for final retrieval of a circular beam profile. With this compressor they achieved 1.5ps pulses, two orders of magnitude smaller than they had started with, and a peak power exceeding 1 GW. The average power was very low (20 mW) as a result of a repetition rate of only 10 Hz. (3)

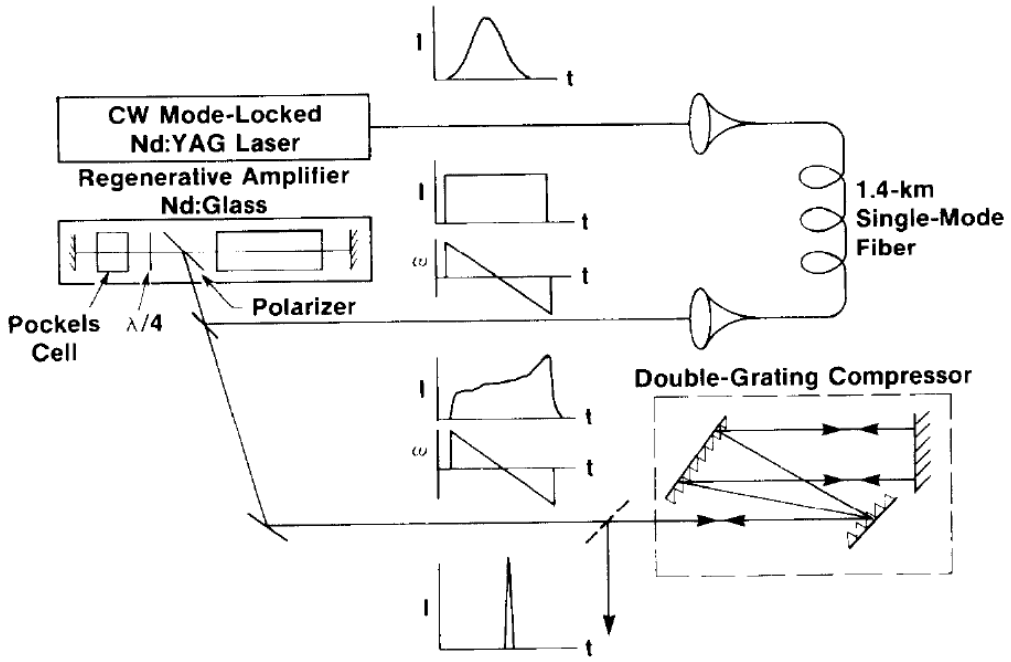

Figure 3.1. *Compression of amplifier chirped optical pulses.* D. Strickland and G. Mourou July 1985. Optics Communications. The system produced 2ps pulses with 1mJ pulse energy.

Although the initial demonstration achieved modest performance, the CPA technique offered the potential for a revolutionary advance in peak power. The Perry group at LLNL improved on the technique and rapidly achieved 1 and 10 Terawatt peak power lasers. (24,26,28) The seminal paper "Terawatt to Petawatt Lasers (25)" introduced the technology and applications to a wide audience. The world's first Petawatt (1000 TW) laser was demonstrated in 1996. (23) Today, all countries have significant research into ultrafast and ultra-intense laser phenomena with more than $1 B spent worldwide annually. Separate from the academic research, the non-thermal mechanism of material removal for pulses less than ~10 psec has created an entirely new industry in precision machining (29). The intense x-rays and high energy particle creation by petawatt class lasers have applications from inertial confinement fusion, biology, materials science, and, even nuclear weapon research. (23)

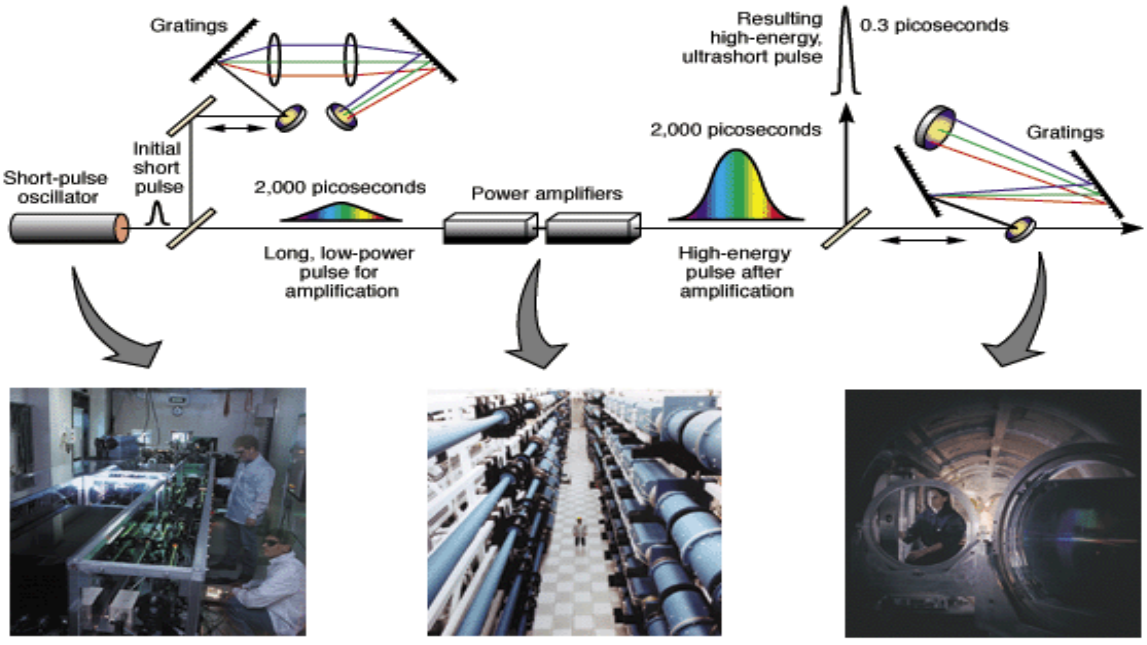

The chirped-pulse amplification technique makes it possible for the Petawatt laser's high-power pulses to pass through laser optics without damaging them. Before amplification, low-energy laser pulses are passed through diffraction gratings to stretch their duration by as much as 25,000 times. After amplification, the pulses are recompressed back to near their original duration. Because the pulses pass through the laser optics when they are long, they cause no damage.

Figure 3.2: Original Petawatt Laser at Lawrence Livermore National Laboratory

While large scale, multi-petawatt, peak power systems are being pursued at national laboratories throughout the world (LLNL, LLE, ILE, ELI, CEA), more immediate, practical applications require the combination of high peak power with high average power. Industrial and biologic processes require the sub-micron precision of the individual pulse interaction but can only achieve practical application by operating at very high repetition rate. Finally, solid-state lasers are limited to operation from ~750 to 2000 nm. (7) Many applications require shorter wavelength visible or even ultraviolet radiation.

The objective of the this thesis work is to design and build a state of the art, high average power fiber/CPA system producing diffraction-limited output in order to explore the creation of high average and high-peak power deep ultraviolet radiation by harmonic generation. The specific, quantitative goals were the creation of a 40 W average power, 1 GW peak power system at 1047 nm and 100 kHz. Followed by frequency conversion to the second and fourth harmonic with the objective of 500 MW and 100 MW peak power, respectively. The selection of the 1047 nm is to enable further amplification in Nd:YLF in a later project.

The system starts with a commercial nonlinearly mode-locked Yb:Silica fiber laser at 1045 nm. This oscillator (MenloSystems YLMO) produces pulses of 150 fsec duration at a repetition rate of 50MHz. The oscillator produces 1 nJ pulses for an average power of 0.05 W and a pulse spectrum with a FWHM= 10.7 nm. The 50 MHz pulse train is then amplified in single-mode commercial Yb:Silica fiber amplifiers to produce 10 nJ pulses at 50 MHz and an average power of 0.5 W.

The output of the fiber preamp is coupled to a 2km silica fiber to stretch the pulse from 150fs to ~1ns. The output of the fiber stretcher is passes through an Acousto-optic modulator (AOM) pulse picker to reduce the repetition rate from 50MHz to 100kHz. A second AOM can be externally triggered to generate gated pulse windows, or bursts of the 100 kHz pulse train. The external AOM can also be used to control the amplitude of the pulses. The pulse train then goes to two Yb doped photonic crystal amplifiers which raise the pulse energy from 10nJ to 300uJ. The pulse train the leaves the fiber amplifiers to enter a double grating compressor resulting in pulse durations to <400fs and energy output >300uJ at 100kHz. The stretcher is seeded with 3.3mW at 150fs and the mini-compressor receives 8.1mW at ~1ns. The pre-amplifier is seeded by 1.25mW. The main amplifier is seeded by 1.25W after the double pass of the pre-amplifier. 33W is measured pre-compression out of the stretched port resulting in 330uJ pulses. The amplifiers are cooled with DI water in a closed loop with a water to air heat exchanger to maintain a stable operating temperature of 22 ± 0.5 ^{o}C.

The pulse train then leaves the compressor and enters the Harmonic Generator Assembly (HGA). Separate from the HGA is a diagnostics suite containing an autocorrelator, grating spectrometer, fast photodiode and energy meter. Within the HGA are CMOS cameras to constantly monitor the fundamental and all harmonic paths (1ω, 2ω, 3ω, 4ω). These cameras are used both to align the incident beam into the crystal and to monitor the output for any laser damage, diffraction from edge clipping, etc. Each of the elements of the system are described in detail in the following chapters.

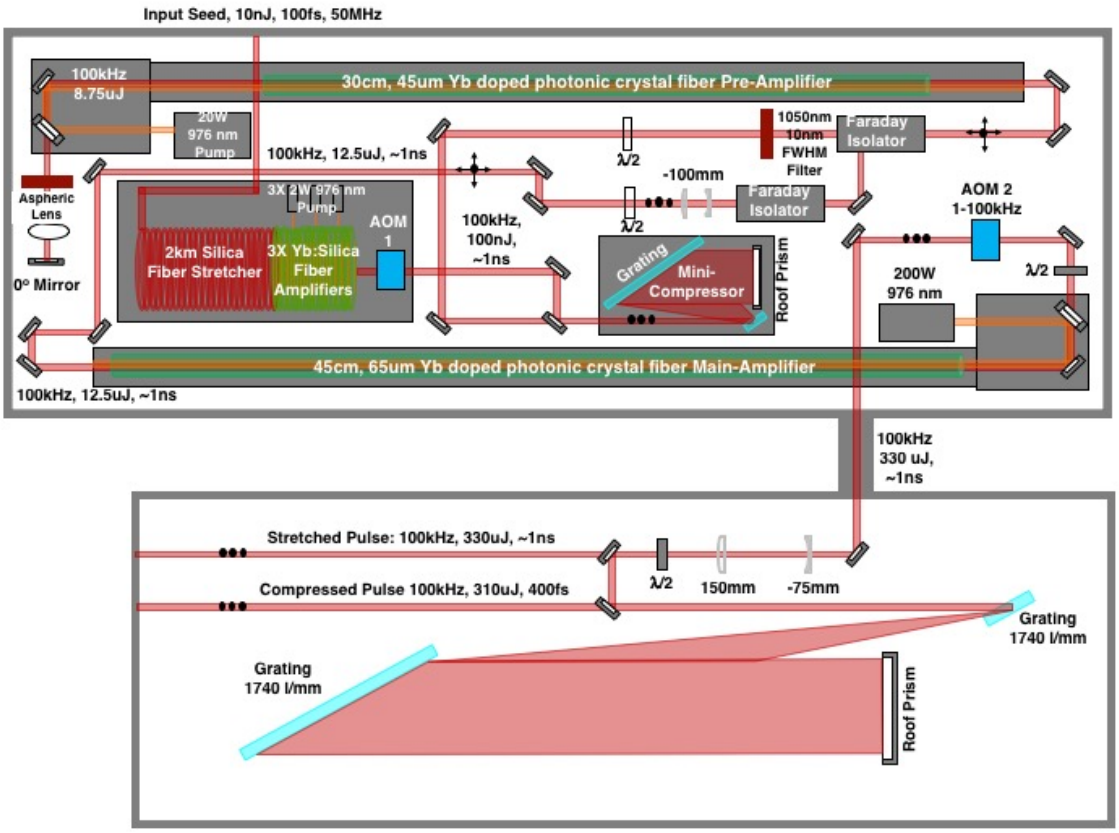

Figure 3.3 Amplifier and Compressor layouts.

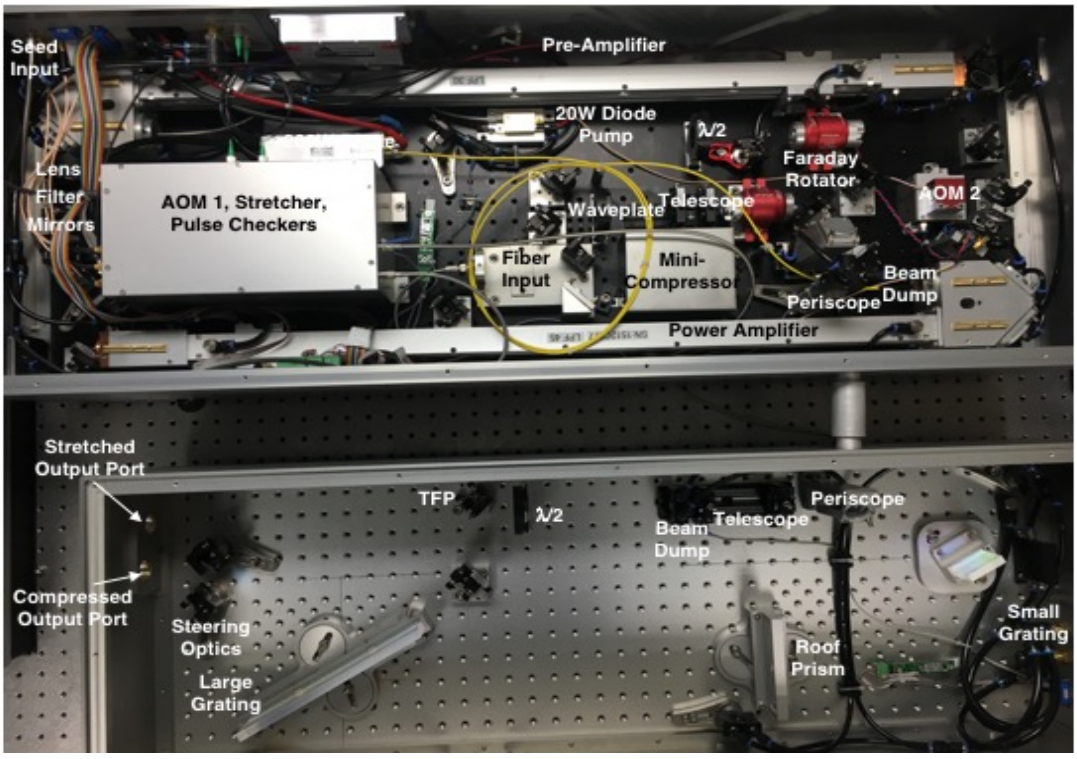

Figure 3.4 Actual system layout.

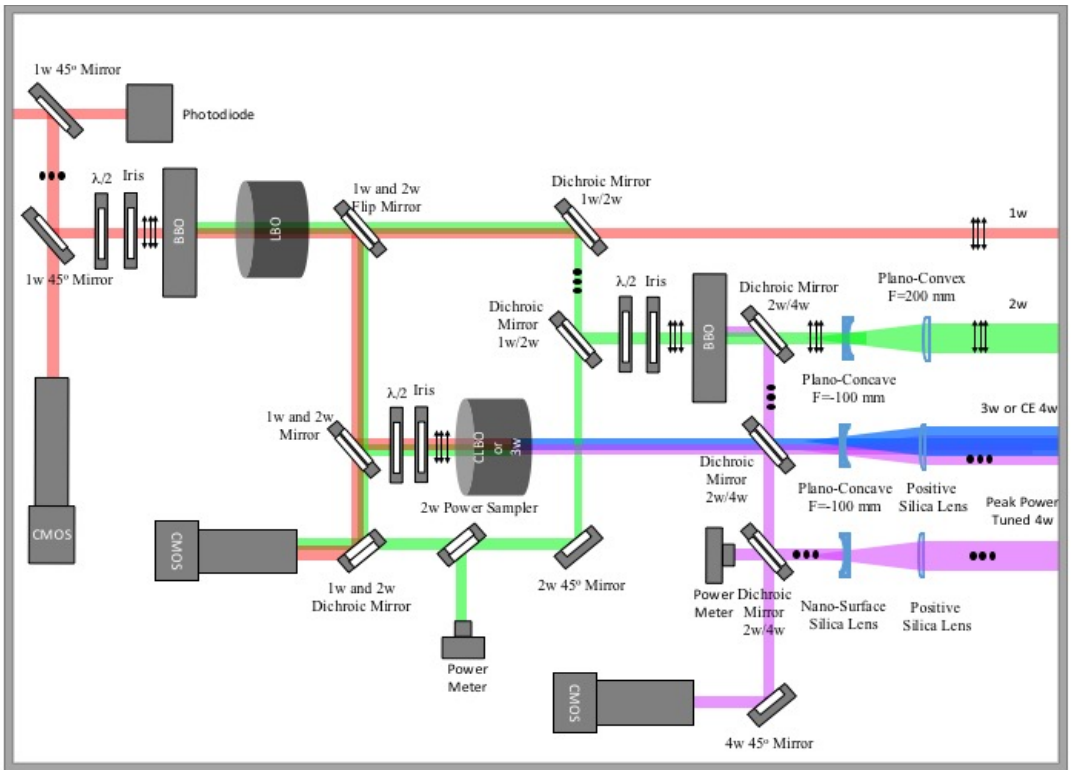

Figure 3.5 Harmonic Generation Box and Diagnostics.

In summary, we achieved 32 W of average power at 100 kHz at 1047 nm, (E_{pulse} = 320 microjoules). The pulse exhibited a FWHM of 390 fsec for a peak power of ~800 MW. We could not get the pulse shorter due to modulation of the spectrum near 1047 nm due to filters placed in the amplifier chain to suppress gain at 1030 nm. Model calculations suggests that without these filters, we could have obtained pulses ≤ 300 fsec enabling the 1 GW objective. We achieved SHG conversion efficiency exceeding 65% and 35% (of the 2ω) to the 4th harmonic. While the 2ω conversion is in good agreement with theory the 4ω was only ~75% of the initial theoretical prediction. Investigation showed that multiphoton absorption and other nonlinear processes in the BBO crystal are limiting. To my knowledge, this is the highest average and peak power) 4ω fiber laser produced to date. Combined with the near diffraction-limited (M^2<1.2) beam quality, we have achieved the highest brightness for any solid-state laser operating below 280 nm.

4. Seed Oscillator

In 1990 the discovery of Kerr-lens modelocking in titanium-doped sapphire lasers changed the way people approached short-pulse generation. Kerr-lens modelocking employs the nonlinear effect of self-focusing inside the gain crystal to produce an intensity dependent loss except for the highest intensity mode. (30) This Passive mode-locking results from amplitude instability when an intense fluctuation experiences lower losses compared to less intensive parts of radiation. The reaction time of the nonlinear element be as short as the fluctuation itself. The shortest (most intense) pulse occurs when all the modes oscillating in the resonator are in phase. "Mode-locking" refers simply to different mechanisms employed to "lock: the cavity modes in phase. In Kerr Lens mode-locking, the pulse will essentially "evolve" in the resonator until it produces the most intense (shortest) pulse supported by the nonlinear modal structure of the cavity and the gain of the medium. (17) Titanium sapphire became increasingly attractive to the ultrafast optics field due to its large gain spectrum, high thermal conductivity, short pulse duration and high peak power. Ti:sapphire has found its way into many industries since its first discovery of femtosecond pulse generation in 1990, the military, biomedicine, and telecommunications industries all have taken advantage of it. (17)

While Ti:sapphire meets many of these requirements, such systems exhibit low electrical to optical efficiency due to their need to be pumped from 515 to 540 nm. The lack of efficient pump sources in the 515 to 540 nm region results in a complex and elaborate setup which is applicable only to laboratory settings. As a result, reliable, steady, and robust oscillator sources were sought. (17)

Mode-locked fiber lasers became the next alternative. Fiber lasers exhit compactness, stability, high beam quality at the fundamental transverse mode of the fiber and significantly reduced alignment difficulty. The length of fiber produce a high surface area-volume ratio enabling efficient heat dissipation and air cooling. A fiber oscillator has only a few key components: a loop of single-mode fiber, a rare earth doped fiber section for gain, and, a saturable absorber or Kerr Lens medium which is used to modelock. (17) There are some limitations to fiber seed oscillators however. The small range of tunability, pulse energy limitation, longer pulse durations and nonlinear limitations on the pulse. Due to the fact that light travels in a guided core unlike free open-air-bulk material systems, fiber nonlinearities are enhanced by roughly four orders of magnitude. (30)

Pulsed passive mode-locking is the key to achieving short pulses with fiber lasers as well as solid state. This method of mode-locking relies on the fact that the pulse experiences a lower intracavity loss than a continuous wave solution. Under CW operation, the fiber does not have a high enough gain to overcome the loss of the saturable absorber. The emitted intensity is simply spontaneous emission with spectral content equal to the fluorescence bandwidth (17) The random fluctuations from spontaneous emission along with interference of laser modes with random phase relations leads to fluctuations of the light intensity. As the diode laser continues to pump the Yb doped fiber, the gain increases to the point where one of the intensity fluctuations rises above the cavity threshold and the pulse begins to oscillate. For fiber lasers, several distinct modes can be chosen by varying the cavity dispersion in the amplifying and connecting fibers as well as the gratings separation as well as the adjustments of the wave plates that

control the nonlinear pulse evolution. During amplification spectral narrowing occurs thus providing a smooth and broad change in amplitude fluctuations. The perfect saturable absorber would have perfect selection between the transmission of high and low intensities. It would also have instantaneous response time. The role of the saturable absorber suppresses the lower intensity light relative to the high intensity (shortest pulse) light. (17) Amplification occurs when the cavity round trip produces a net gain greater than the net losses of the system. With each passage through the gain medium the pulse will experience an intensity gain of exp(gl) where g is the gain coefficient per unit length. Oscillation threshold requires that the photon density on a round trip must be equal to the initial photon density,

$$\gamma exp(2gl) = 1$$

Where γ is the total round-trip loss. When this is equal to one the gain and the losses are balanced and laser oscillation can occur. When we include saturable loss, α, we obtain,

$$\gamma exp(g - \alpha)2l = 1$$

The illustration below gives an example of how a saturable absorber cleans up the peak pulses to form a train of single mode locked femtosecond pulses. (30)

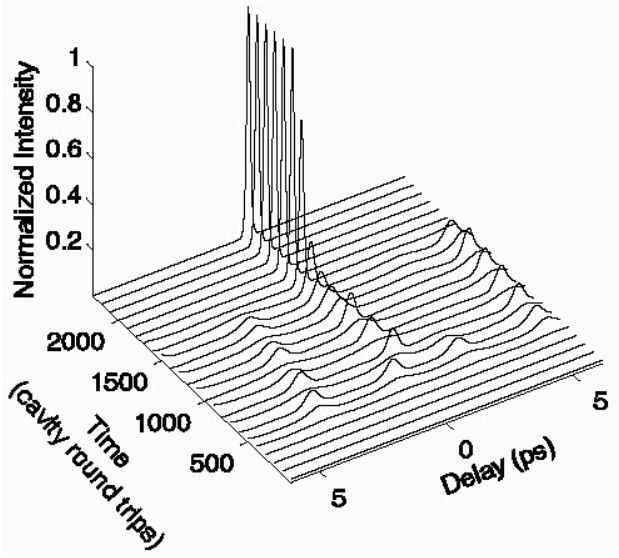

Figure 4.1. Simulation from Joel Buckley showing the buildup of a mode-locked pulse from noise. *High-Energy Ultrafast Ytterbium Fiber Lasers*, Joel Buckley Doctoral Dissertation August 2006.

Real saturable absorbers have response times on the order of picoseconds (semiconductors) to nanoseconds. As a result, femtosecond systems have evolved past mode-locking with saturable absorbers. "Artificial" saturable absorbers use the nonlinear phase shift between two interfering beams. When a proper linear phase bias is applied, the artificial saturable absorber will constructively interfere for higher intensities and destructively for lower intensities. (31)

Kerr Lens Mode-Locking

Kerr Lens mode-locking (KLM) has become dominant in the industry. By not requiring a saturable absorber and responding at the speed of the laser pulse itself, KLM has proven to be simple, robust and provides the shortest duration pulses. The Kerr effect is a well-known phenomenon which is a result of the self-focusing in optical materials. (17) As described previously, the initial embodiment was simply to place an aperture inside a Ti:Sapphire laser cavity. The size of the aperture was set to match the self-focused beam resulting in lower loss for shorter pulses. Longer pulses would experience a higher

intercavity loss and be suppressed. (17) These systems were so successful that prism and grating compressor were placed internal to the cavity to compensate for the Group-Velocity Dispersion resulting from passage through the gain medium and multilayer mirrors. Pulses as short as 10 fsec have been obtained from KLM Ti:Sapphire lasers. (17)

The application of KLM to fibers is more complicated due to the fact that the fiber core is, itself single transverse mode. In mode-locked fiber laser, the Kerr effect is used to rotated the orientation of elliptically polarized light. After traveling through the single mode fiber and amplifier the second quarter wave plate is used to adjust the orientation of the linearly polarized light as it enters the polarizer. The half wave plate is used to adjust the orientation of the linearly polarized light as it enters the polarizing beam splitter. The most intense pulses experience the most rotation and hence, have the highest transmission through the polarizer. The pulse then passes through a grating or prism pair to provide negative GVD to compensate for the positive GVD in the active and passive fiber. Pulse durations as short as 36 femtoseconds utilizing a double pair grating configuration and 28 fsec using a prism compressor have been obtained (31,32).

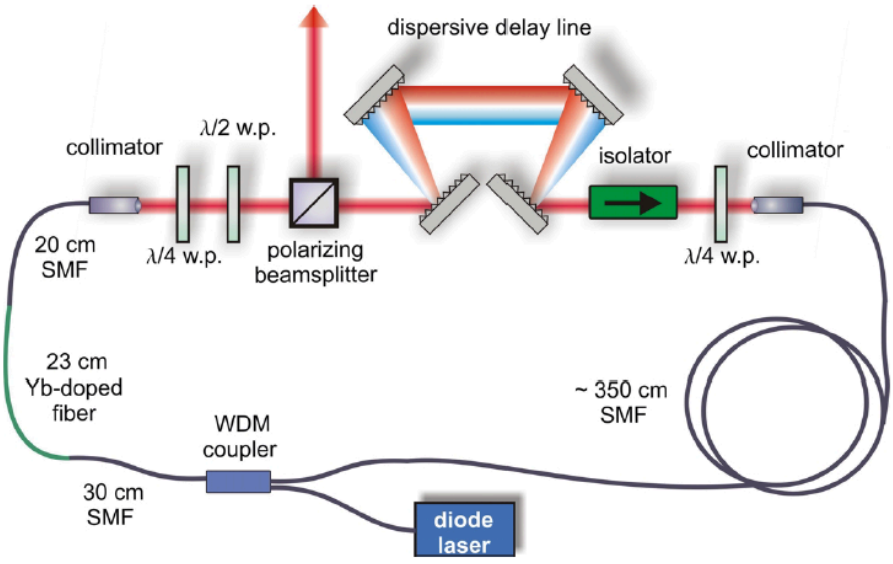

Figure 4.2 Schematic of a 36-fsec pulse Yb fiber laser with grating compression Joel Buckley et al. *Generation of 36-fsec pulses from a ytterbium fiber laser.*

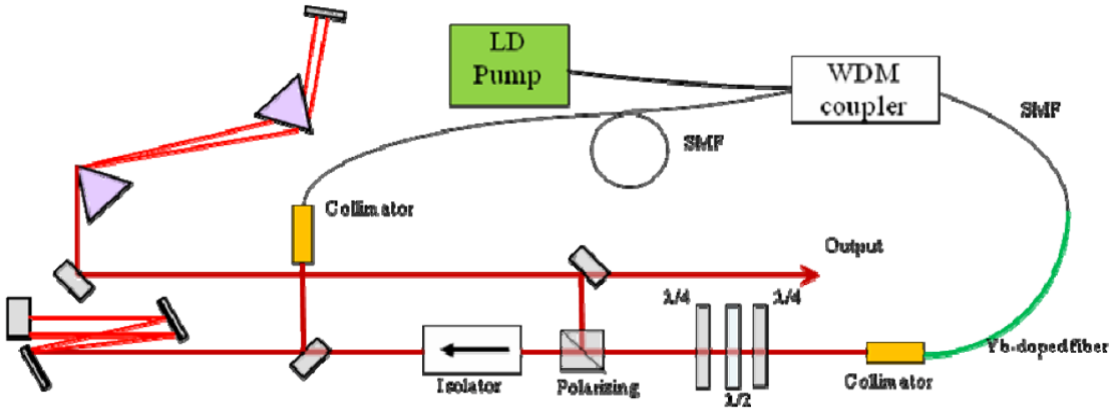

Figure 4.3 Schematic of the generation of 28.3fs pulses with prism compression. Xiangyu Zhou et al. 2008 *Generation of 28-fs pulses from a mode-locked ytterbium fiber oscillator.*

The seed oscillator for this project was designed and produced by Menlo Systems (Figure 4.4) .

The seed oscillator produces 1nJ seed at 1045nm and a 50MHz repetition rate. The pulses exiting the oscillator are chirped but can be compressed to near their transform-limit of 150 fsec. The oscillator was designed with interference filters before and after the fiber amplifier to shift the gain spectrum to near 1045 nm and suppress oscillation at 1030 nm. The spectral bandwidth and transform limit match nicely with the calculated output pulse duration and spectrum (Figure 4.6). The spectrum is tuned to 1047nm with a near Gaussian shape.

Figure 4.4 The seed oscillator. The system seeds the stretcher with 3.3mW of average power at 50MHz. The system is air cooled with a muffin fan.

Figure 4.5 The rack that houses the diode control electronics, seed oscillator, and water chiller. The water chiller operates at 22-22.1° C

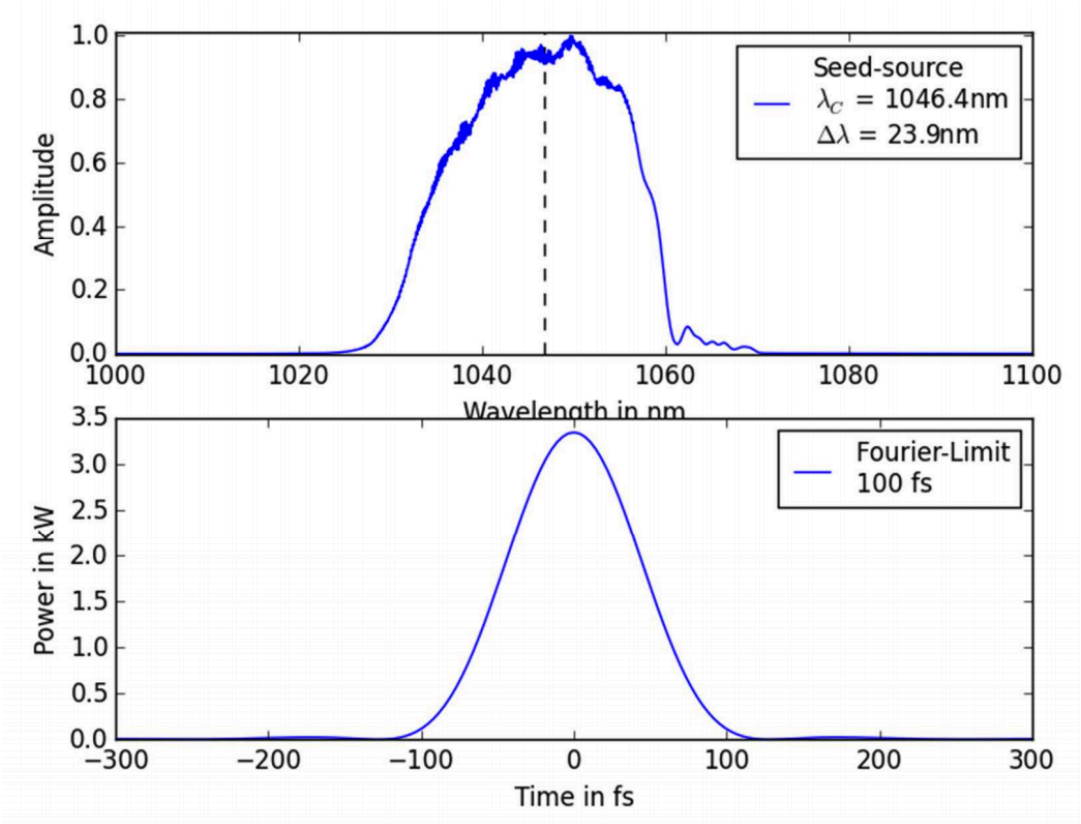

Figure 4.6 Spectrum and autocorrelation of the YLMO oscillator obtained from Menlo systems Inc. The system deploys a patented figure 9 design

5. Pulse Amplification

In this section we will discuss the amplification of the 1047nm, 100fs pulses from 1 nJ to >300uJ. This section will also discuss the theory of pulse amplification as well as comparisons and examples of solid-state vs photonic crystal fiber (PCF) amplifier systems. For femtosecond pulse, the amplifier material must exhibit broad emission lines, good absorption at diode-pump wavelengths, and a reasonably high quantum efficiency.

If we ignore fluorescence and pumping during the duration of the pulse being amplified, the population inversion, n(t), decreases according to (17)

$$\frac{\partial n}{\partial t} = -\gamma n c \sigma \phi$$

Where the c is the speed of light in the medium c, σ is the stimulated emission cross section and ϕ. Is the photon flux. Similarly, the pulse travelling through the amplifying medium grows according to the decrease in population,

$$\frac{\partial \phi}{\partial t} = cn\sigma\phi - \frac{\partial \phi}{\partial x}c$$

Frantz and Nodvik solved the photon transport equation in 1963. In the limit that γ=1, we can manipulate the above to obtain, (33)

$$\frac{\partial}{\partial t}[(\frac{1}{\phi})(\frac{\partial \phi}{\partial t}) + (\frac{c}{\phi})(\frac{\partial \phi}{\partial x})] = -2\sigma cn[(\frac{1}{\phi})(\frac{\partial \phi}{\partial t}) + (\frac{c}{\phi})(\frac{\partial \phi}{\partial x})]$$

The solution to this equation comes in a generalized form that needs to be integrated with respect to whatever pulse shape is of interest,

$$\phi(x,t) = \frac{\phi_o}{(1 - [1 - exp[-\sigma \int_0^x n(x)dx]]exp[-2\sigma c \int_0^{t-x/c} \phi_o(t)dt)])}$$

Square Pulse, $\phi_o(t) = \phi_o$ for $0<t<\tau_p$

For simplicity we will assume a square pulse is injected into the amplifier where the photon flux density can then be considered constant during the duration of the pulse and is uniform throughout the amplifier. The photon flux density can then be reduced to the following form:

$$\phi(x,t) = \frac{\phi_o}{(1-[1-exp[-\sigma n x]]exp[-\gamma\sigma\phi_o c(t-x/c)])}$$

The gain then for a pulse traveling through a medium of length L can be given by integrating the photon flux density as a function of length and time over time. (17,33) Dividing by the initial pulse duration and photon flux density this leaves the gain in the form of various input parameters that can be adjusted to use direct experimental laser parameters.

$$G = \frac{1}{c\gamma\sigma\phi_o t_p} ln[1+(exp[\gamma\sigma\phi_0 t_p c]-1)e^{n\sigma l}]$$

Writing the input energy per unit area and saturation fluence combined with the stored energy per unit volume and small signal gain coefficient from the population inversion density and emission cross section, the gain can be represented as: (17)

$$G = \frac{E_s}{E_{in}} ln[1+[exp(\frac{E_{in}}{E_s})-1]exp(g_o l)]$$

E_{in} is the input energy per unit area and E_s is the saturation fluence and J_{st} is the stored energy per unit volume:

$$E_{in} = c\phi_o t_p h\nu$$

$$E_s = \frac{h\nu}{\gamma\sigma} = \frac{J_{st}}{\gamma g_0} = \frac{h\nu n}{\gamma g_0}$$

Small Signal Gain

In the limit of low-input signal, E_{in} such that the input energy per unit area is far smaller than the saturation fluence thus $G_oE_{in}/E_s << 1$ then the above equation for G reduces to,

$$G \approx G_0 \equiv exp(g_0 l)$$

Mathematically, this limit is where there is no depletion of the excited state population by the input pulse. The excited state is a constant, $n(t) = n_o$. Here the gain is exponential with amplifier length.

Saturated Amplification

In the limit that, $E_{in}/E_s >> 1$ the energy gain that is linear with the length of the gain medium, (17)

$$G \simeq 1 + (\frac{E_s}{E_{in}}) g_0 l$$

In this case, every inverted state emits energy to the beam. The Frantz/Nodvick solutions assumed no loss in the medium. (33) The assumed pulse shape in the beginning was square to ease the derivation of the gain equation. For stretched pulses this limit holds to a good approximation and only becomes invalid when the amplified pulse shape differs greatly from the input pulse shape due to the different ends of the pulse experiencing different levels of gain. (Avizonis and Grotbeck) extended this theory to encompass the derivation without approximation resulting in: (34)

$$\frac{\mathrm{d}E(x)}{\mathrm{d}x} = E_s g_0 [1 - exp(\frac{-E(x)}{E_s})] - \alpha E(x)$$

Here the energy change as a function of traverse gain medium is written with α being the loss coefficient per unit length. This equation can only be solved analytically when the losses are assumed to be zero.

Application to Fiber Amplifiers

Ytterbium doped fibers emerged as laser amplifiers in 1997. Yb doped fibers offered broad amplification from 975 to 1200nm (Figure 5.1). (5), high output power, excellent power conversion efficiency and good beam quality. Unlike Erbium doped fibers at the time, Yb doped fibers didn't have the problems of excited state absorption, concentration quenching due to interionic energy transfer, and higher doping levels were possible.

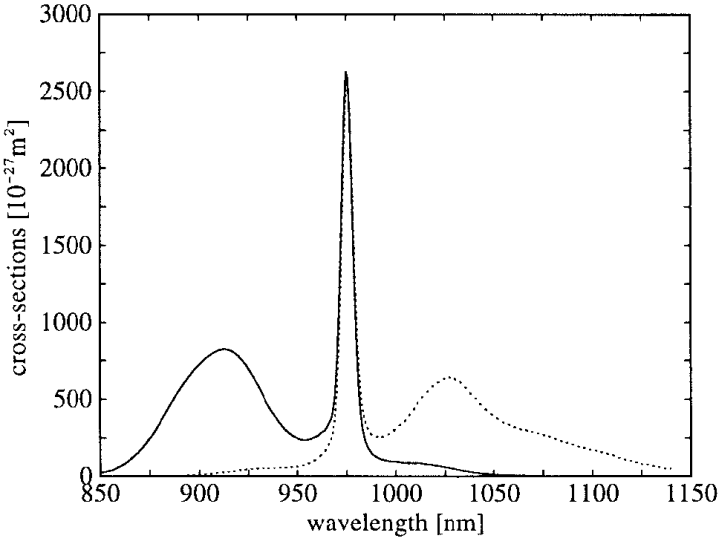

Figure 5.1 Absorption (solid lined) and emission (dotted line) cross sections of Ytterbium in germanosilicate glass. Plot is obtained from *Ytterbium-Doped Fiber Amplifiers*. Rudiger Paschotta et al. July 1997, Journal of Quantum Electronics.

Early experiments performed by Paschotta et al using a white light absorption spectrum showed identical absorption and emission cross sections at 975nm. This leads to a strong quenching if a laser was to be operated at the emission of 975nm.

Figure 5.2
Top: Absorption and emission cross sections of Ytterbium in silica.

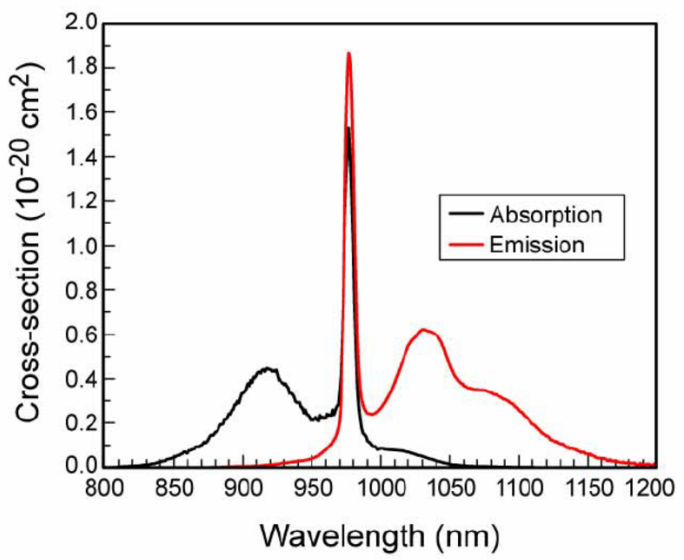

Bottom:
Relative amplification efficiency as function of wavelength.

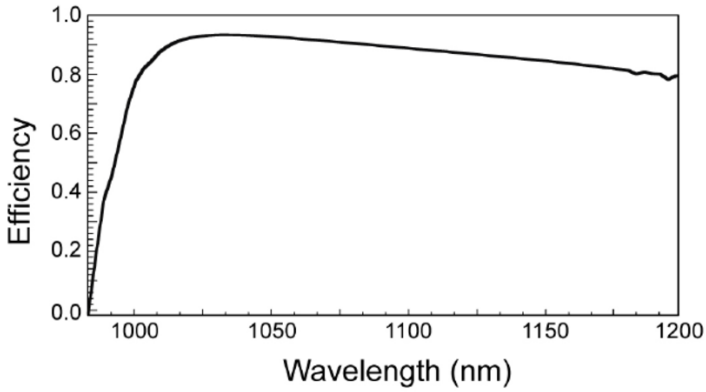

The fiber oscillator produces 1 nJ, 100fs, 50 MHz centered at 1045 nm and an average power of 50 mW. This input is stretched to ~1 nsec in a 2 km silica fiber. The output is 50 MHz and 3.3 mW (0.06 nJ). The pulses are amplified to 100nJ through three, 6 um core single-mode, polarization-preserving fibers each pumped with 976 nm 2W (Figure 5.3, 5.4). The large stretching ratio (150 fsec to ~ 1nsec) from fiber propagation results in a significant nonlinear component to the chirp. This nonlinearity will become an issue when the pulse has to be compressed from a grating stretcher which exhibits a more linear negative dispersion. This mismatch leads to the formation of wings, also known as pedestals that can be seen in the autocorrelation.

Following the fiber amplifiers, the pulses pass through an acousto-optical modulator pulse picker. The AOM can be triggered to select pulses from the 50MHz pulse train from single-shot to down to 100kHz. (9) At 100 kHz, the average power exiting the AOM is 8.1 mW or 81 nJ per pulse. The pulse train then passes to a "mini-compressor." This mini-compressor is a small double-grating compressor that is used to provide fine control of the final compressed pulse duration. It is NOT used to compress the pulse at this stage but rather to provide 25 fsec level control of the final compressed pulse. The mini-compressor exhibits a throughput of 60%. Further losses in the Faraday Rotator, and bandpass filter reduce the pulse train to 1.25 mW or 12.5 nJ per pulse.

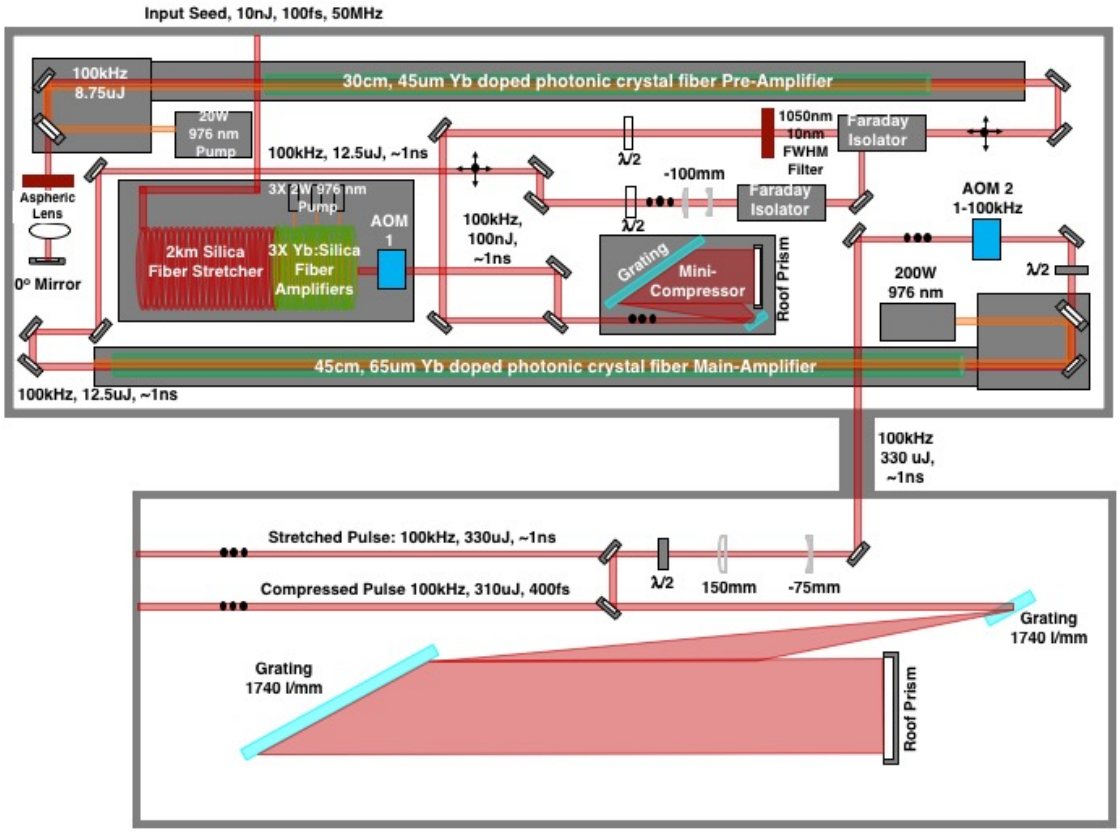

Figure 5.3 Fiber Laser System developed used in this project.

Figure 5.4
2km fiber stretcher and fiber pre-amplifier assembly. Each stage is pumped by a 2 W diode at 976 nm (Courtesy of Active Fiber Systems, GmBH)

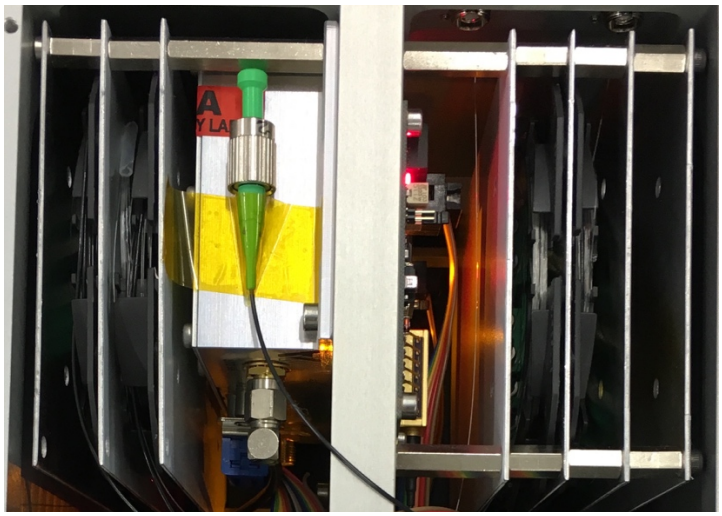

Further amplification in fibers is problematic. A 100 nJ pulse exhibits a peak fluence of 0.7 J/cm^2 in a 6 um diameter single-mode fiber. At 1 nsec, this pulse exhibits an irradiance of 700 MW/cm^2. Propagation in 1 meter of fiber would result in a nonlinear phase (B-Integral) of 1.4. Another factor of 10 would result in self-phase modulation (2). Completely separate are the nonlinear limits of Stimulated Brillouin Scattering (SBS) and Stimulated Raman Scattering (SRS). While SBS is somewhat mitigated by the large bandwidth of the chirped pulse, 20 GW/cm^2 should be considered a maximum irradiance limit for both SBS and laser damage. Special fibers have been produced which exhibit an effective core area of 15 um for 1030 to 1060 nm radiation. Researchers have obtained 50 microJoules in a 1 nsec stretched pulse from such fibers corresponding to an irradiance exceeding 50 GW/cm^2 (10). Operation at this level was plagued by damage and SBS phenomena.

A new class of “Photonic Crystal Fiber (PCF)” was introduced by Philip Russell in the late 1990’s. These “holey” fibers are essentially micro-engineered structures that shape the distribution of the refractive index within the fiber to produce a much larger core for single transverse mode operation.

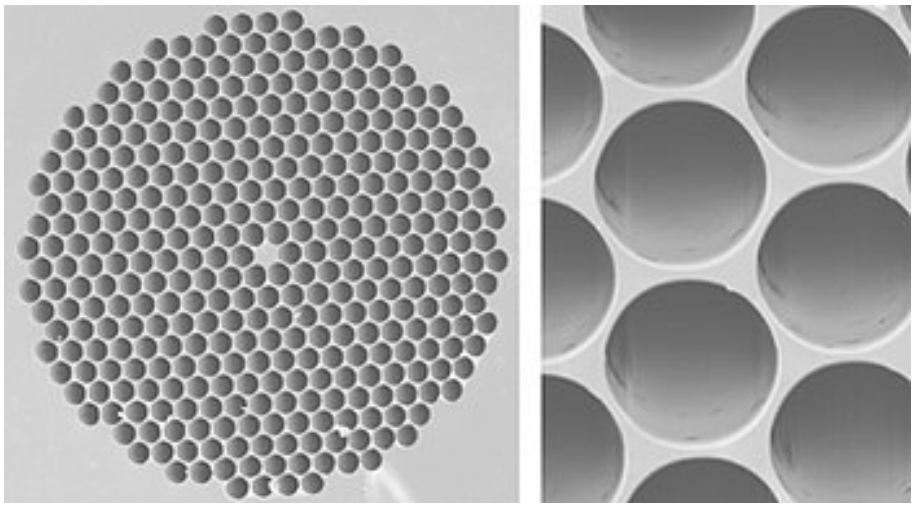

Figure 5.5
Photonic Crystal Fiber.
Holes are 4 um in diameter.
Effective core size = 30 um.

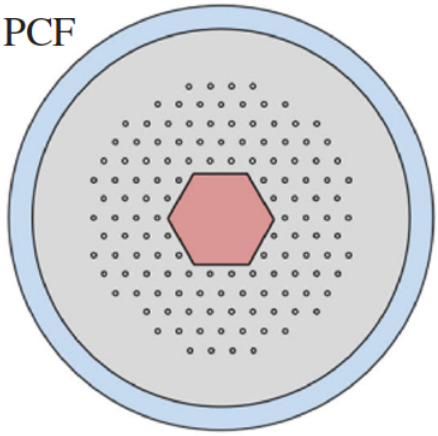

Figure 5.6
Cross section of a standard photonic crystal fiber. The red area is the core. The dark grey is air hole resonators. The light grey is fused silica and the light blue is the air clad. Image is obtained from *Photonic Crystal Fiber Amplifiers for High Power Ultrafast Fibers Lasers,* Thomas Alkeskjold et al. 2013 Science Wise Publishing and De Gruyter.

The introduction in 2014 of Photonic Crystal Fibers as amplifiers in chirped-pulse amplification enables an order of magnitude increase in the extractable power before the onset of SBS and self-phase modulation. (10). For our system, two different doped core sizes were used. For the pre-amplifier PCF a 45um core at 30cm long was acquired from NKT Photonics (Figure 5.7, 40um diameter Yb-doped index neutral core with 200um of pump cladding). The stress induced between the parts creates a polarizing waveguide structure thus allowing only one transverse mode to propagate with one polarization. The outer diameter is 450um.

Figure 5.7

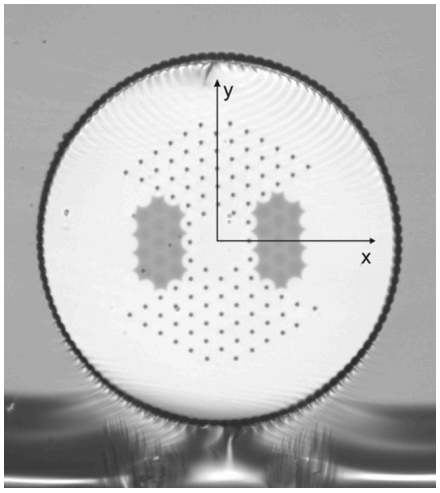

Micrograph of the DC-200/40 PZ-Yb fiber, consisting of a 40 um diameter Yb-dopped index-neutral core, 200 um pump cladding, and large stress applying parts that create a polarizing waveguide structure i.e., only one transversal mode with one polarization can propagate. The out diameter is ~450um, which effectively reduces microbend loss. Image is obtained from *Photonic Crystal Fiber Amplifiers for High Power Ultrafast Fibers Lasers,* Thomas Alkeskjold et al. 2013 Science Wise Publishing and De Gruyter.

The 45um PCF from NKT Photonics (***aeroGAIN-ROD)*** is a Ytterbium-doped PCF for high power polarization maintaining (PM) amplification. The rods feature diffraction limit beam quality with high peak power damage threshold optimized for 1030-1040nm. The pre-amplifier rod has a single core diameter of 55um with a mode field diameter of 45um. The optical to optical efficiency is ~60% with an M^2 of ~1.2. The rods operate at 20 - 25^{o}C. Figure 5.9 shows is an image on the left of the beam following double-pass amplification The image on the right is the theoretical fundamental mode formed within the rod type fibers. From 1035nm to 1055nm, the fundamental mode has high overlap with the core and enables for efficient fundamental mode amplification. There is low overlap from higher order modes thus leading to mode scrambling which suppresses the higher order modes. We use the first PCF in a double-pass configuration which uses a zero degree mirror and aspheric lens to collimate the first pass coming out of the fiber, reflect at the zero degree mirror and filter and be refocused back into the fiber (Figure 5.10).

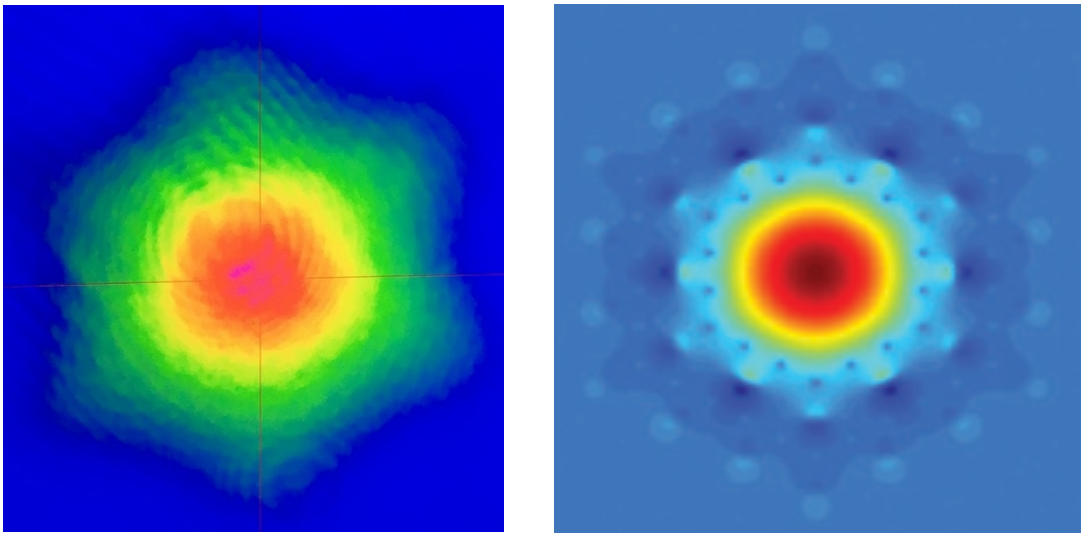

Measured Theory

Figure 5.8 Left: Stretched pulse beam profile from this system measured at 30W. Right: Calculated fundamental mode of the photonic crystal fiber amplifier. Calculation from *Photonic Crystal Fiber Amplifiers for High Power Ultrafast Fibers Lasers,* Thomas Alkeskjold et al. 2013 Science Wise Publishing

The first PCF rod amplifiers pumped by DILAS fiber-coupled laser diodes which operate at 20W and 200 W, respectively at 976nm CW. The first diode pump is driven at 8 amps of input current with a resulting 20W of output pump power. The second diode pump is driven at up to 30 Amps to produce 200 W of CW diode power at 976 nm.

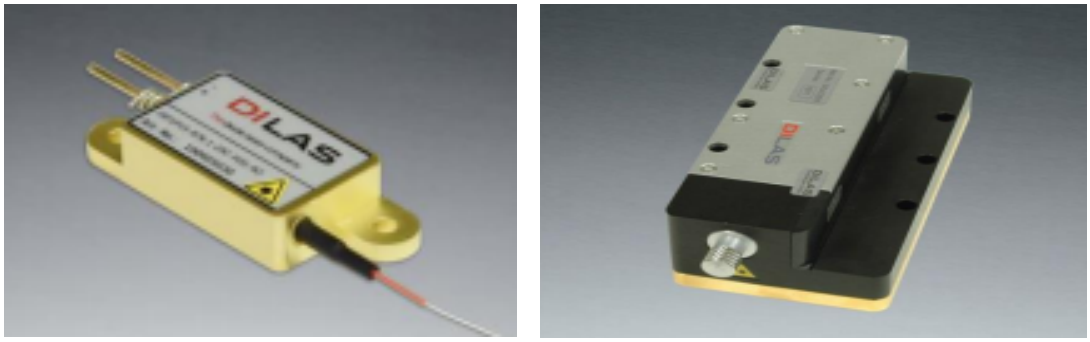

Figure 5.9 Pump diode assemblies for the pre-amplifier (left) and main power amplifier (right). The smaller diode assembly produces 20W of 976nm light which is fiber coupled into the pre-

amplifier. The larger pump assembly is 200W of CW 976nm light fiber coupled into the main power amplifier.

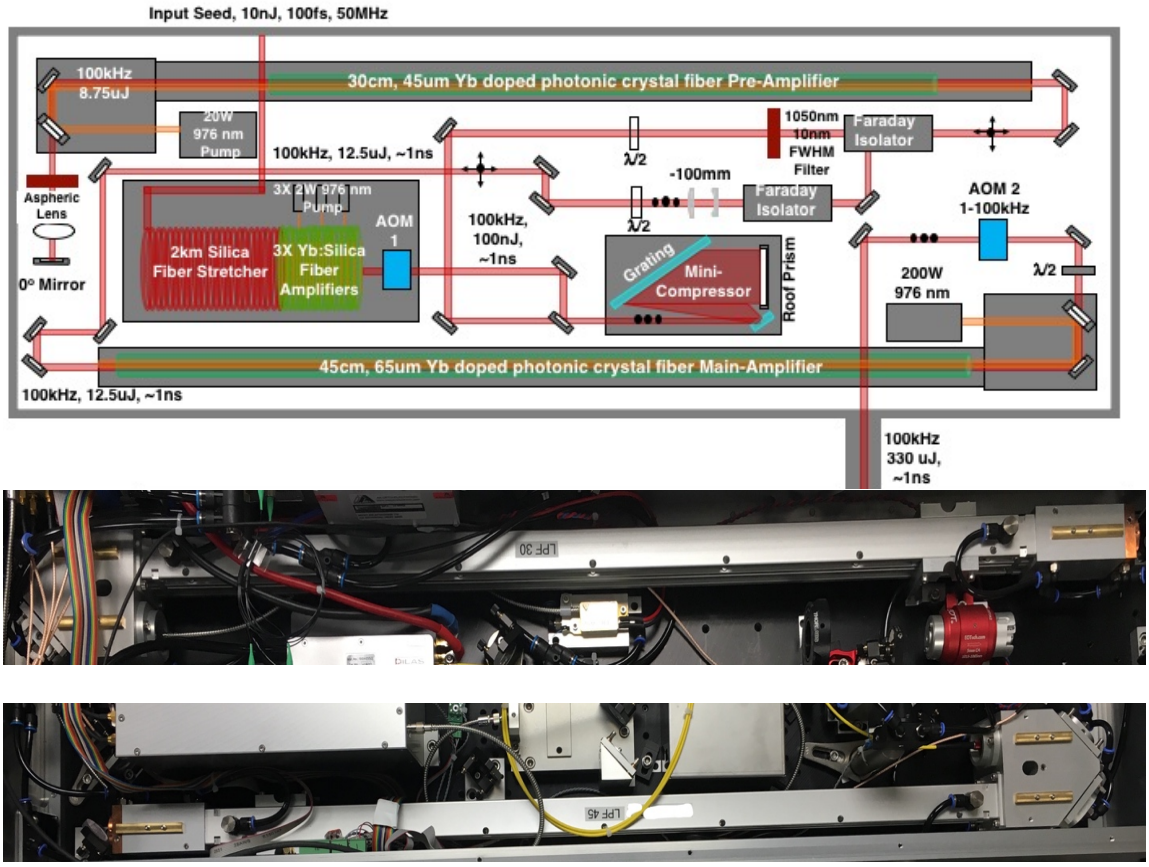

Figure 5.10 Layout of the Yb doped large pitch photonic crystal fiber amplifier section. The first PCF rod amplifier is 30cm long 45 um core. The second ("Main" amplifier) exhibits a core of 60um and is 45cm in length. The main amplifier is seeded with ~1.25W (12.5uJ) of pre-amplifier power which is amplified to ~33W (330uJ). The main amplifier is reverse pumped with 200W of cw 976nm light from a DILAS pump diode assembly.

The pre amplifier is set to run at a constant pump power of 8 W. The double pass of the pre-amplifier results in an output energy of 12.5uJ per pulse at 100kHz (1.25 W average) for the 1ns stretched pulse. The pulse passes through a Faraday isolator to prevent any parasitic oscillation and reflections from the main amplifier to the pre-amplifier and oscillator. The pulses now enter the main amplifier which is another NKT photonics crystal

fiber but this one is 45cm long, a 85um core and a mode field diameter of 65um (Figure 5.11).

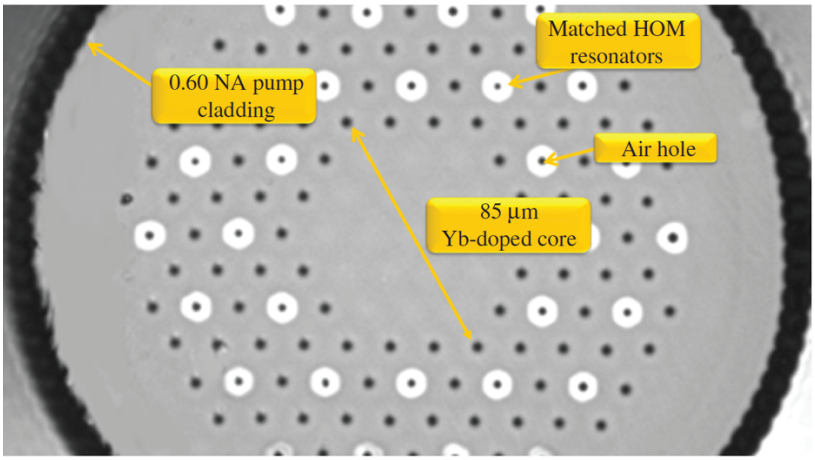

Figure 5.11 Optical micrograph of the DC-250/85-Yb-ROD fiber. The distributed mode fiber is designed utilizing both total internal reflection form the air holes and the photonic bandgaps which form coupled cladding states and are at resonance with the fundamental mode at the first wavelength region. From *Photonic Crystal Fiber Amplifiers for High Power Ultrafast Fibers Lasers,* Thomas Alkeskjold et al. 2013 Science Wise Publishing

The main amplifier is driven with a 200W, 976nm fiber coupled diode laser also from DILAS. The diodes are driven from 0 to 28 amps with 35 amps total available for the main amplifier. The diode output is linear with driver current and are operated at 80% of maximum power to increase lifetime. When the main amplifier pump diode is set to zero, the main amplifier absorbs a large amount of the input 12.5uJ reducing it to 2.5uJ. The main amplifier does not overcome absorption and losses until 3 amps of driving current are put onto the diodes resulting in 8W of pump power. This gives 1W of average power out of the main amplifier. After 3 amps the main amplifier enters the linear gain regime and climbs nearly linearly with driver current and thus pump power. The amplifier starts to enter the gain saturation regime at 63W of input pump. At 28 amps of driving

current there is 155W of pump power being delivered with a resulting G = 26 and 330uJ per pulse at 100kHz ~1ns. The full plot of pump power vs 1047nm output is shown below.

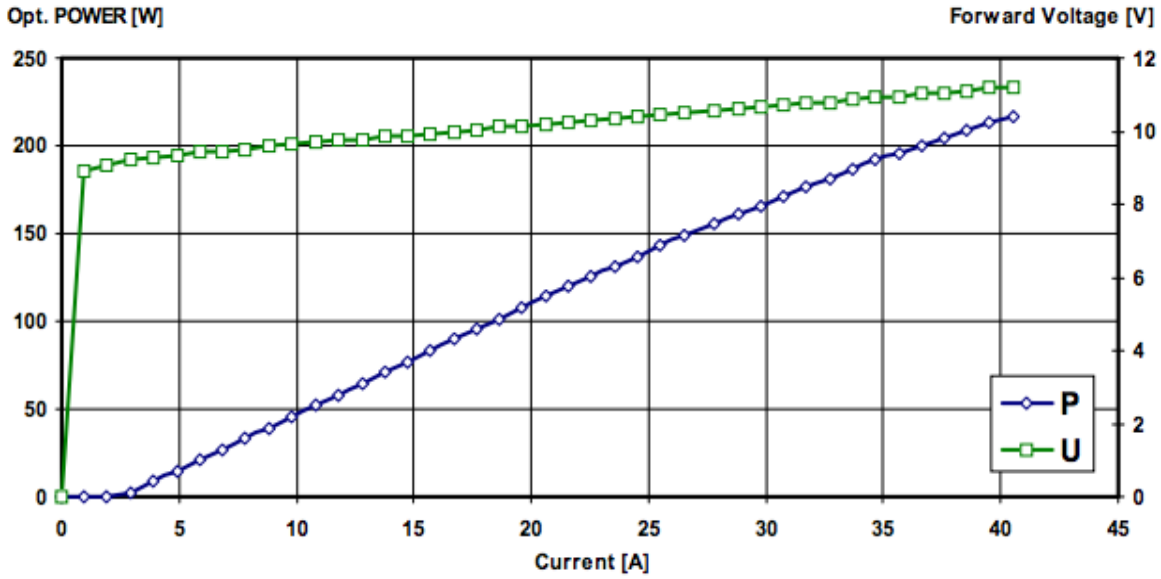

Figure 5.12 Power output as a function of driving current for the large 200W pump diode assembly. The power output of the laser is nearly linear with the pump power of the diodes shown below which is rare.

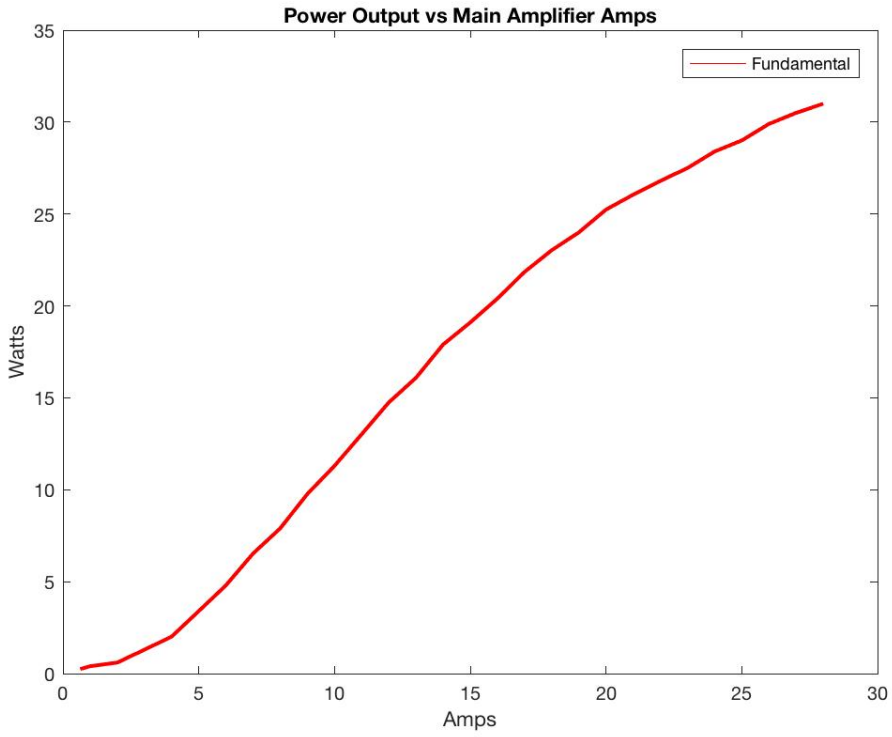

Figure 5.13 Laser power at 1047 nm as a function of main amplifier drive current. At 28 amps of driving current the measured power out of the stretched power was 33W out of the stretched port and 31.7W out of the compress port.

The fiber amplifiers maintain high beam quality with very stable output power over long durations. (1, 5-11, 30-36) T. Alkeskjold et al demonstrated with the same fiber operating at 1030nm the power fluctuation was negligible over 100hours of continuous operation time with 100W of output power. The spectrum of our final output pulse is shown below with a calculated 6.1nm bandwidth before compression. I used an Acton Spectra Pro -300i grating based spectrometer with a CMOS focal plane array (5.3 um pixels) to measure the spectrum. The spectrometer has a 600line/mm grating which produces a spot of ~1.1mm in the dispersion axis on the focal plane. We can calculate the spectrometer dispersion from the grating equation,

$$m\lambda = d(sin\theta_{in} + sin\theta_{out})$$

$$\frac{d\lambda}{fd\theta} = \frac{dcos\theta}{f} \qquad \Delta\lambda = \frac{d\lambda}{fd\theta} * \Delta L_{axis}$$

Due to the filtering before the amplifiers, the spectrum shows a shaper edge on the blue side rather than on the red. The filters had to be angle tuned to pass longer wavelengths because the gain in the amplifiers is optimized for 1030-1040nm. 2 filters were placed in the beam paths before the first pass of the pre amp, a double filter pass during second pass of the pre amp. Thorlabs bandpass filters centered at 1050nm with a FWHM of 10nm were used to shape the spectrum and center it at 1047nm rather than 1030nm.

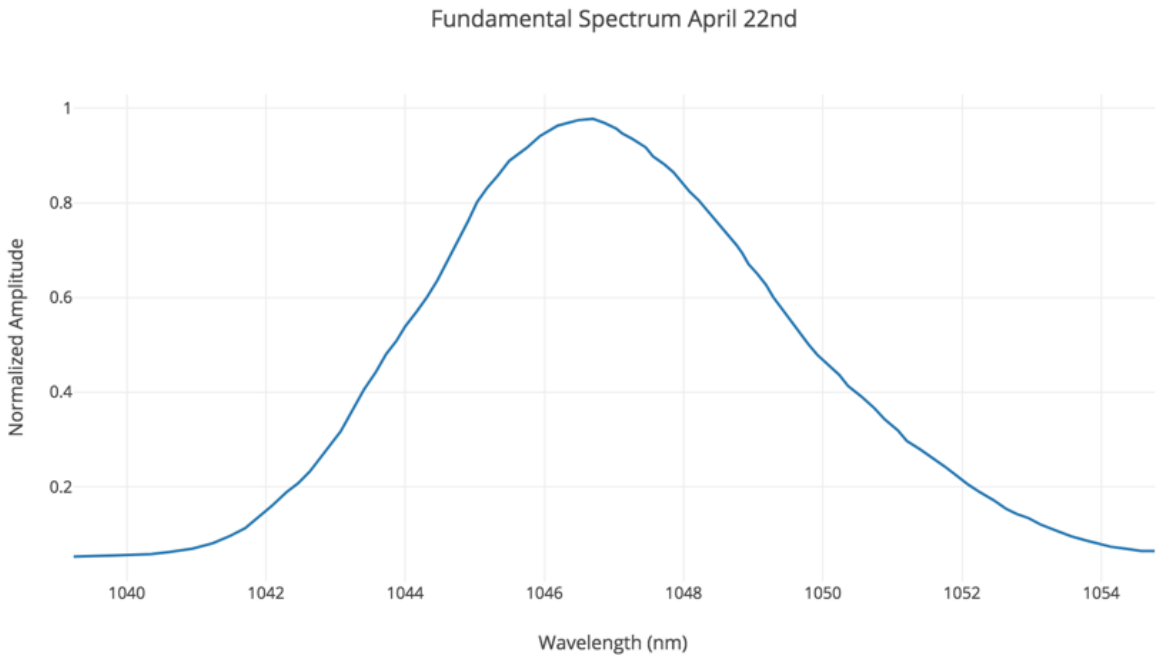

Figure 5.14 Measured spectral distribution of the compressed pulse. The FWHM is 6.1nm centered at 1046.9nm. The central wavelength and spectrum can be shifted and modulated by rotating the waveplates before the amplifiers and angle detuning the spectral filters.

In summary, we obtained 330uJ at 100kHz for the 1ns stretched pulse (average power = 33 W). Out of the photonic crystal fiber the beam is ~750um FWHM. The beam is then expanded with a Galilean telescope (-75mm input and 200mm collimating lens) to produce a beam FWHM of ~2.3 mm. At this point the pulse train is ready for compression from a double grating Treacy style compressor.

6. Pulse Compression

Treacy demonstrated the use of a pair of ruled gratings in 1985 to compress picosecond optical pulses that had acquired a previous positive group velocity dispersion.(3) The negative dispersion induced by a pair of parallel gratings creates a time delay that increases as a function of wavelength. Treacy derived the frequency dependent phase and time delay which can be used to either stretch or compress optical pulses. Ideally, the separation between the gratings is chosen such that the leading edge of the chirped pulse is delayed to overlap with the trailing edge of the pulse at the output of the grating pair. If the input chirp (time-dependent frequency) matches the inverse of the grating pair, transform-limited pulses would then be produced (no residual chirp, $\partial\omega/\partial t = 0$). A pulse that is Gaussian in spectrum transforms to a pulse that is Gaussian in time with a time-bandwidth product of

$$\Delta\tau\Delta\nu = 0.44 \qquad \text{and} \qquad \Delta\tau = \frac{0.44}{\Delta\lambda}\frac{\lambda^2}{c}$$

We measure a spectral FWHM of 6.1 nm which would result in a ~250fs pulse duration if our pulse was Gaussian. For our actual pulse shape, we would expect an ~330 fsec pulse at optimum grating separation. This means that our pulse is not transform-limited.

The use of a fiber stretcher and a grating compressor does have its limitations. Grating compressors correct mostly for quadratic phase distortions. Fiber stretchers induce group delay dispersion and other nonlinear dispersion effects such as self-phase modulation (2) and third order dispersion according to:

$$\beta(\omega) = \beta_0 + (\omega - \omega_0)\beta_1 + \frac{1}{2}(\omega - \omega_0)^2\beta_2 + \frac{1}{6}(\omega - \omega_0)\beta_3 + ...$$

$$\phi(\omega) = \phi_0 + (\omega - \omega_0)(\frac{\partial\phi(\omega)}{\partial\omega}) + \frac{1}{2}(\omega - \omega_0)^2(\frac{\partial^2\phi(\omega)}{\partial\omega^2}) + \frac{1}{6}(\omega - \omega_0)^3(\frac{\partial^3\phi(\omega)}{\partial\omega^3})$$

Here ϕ_o is a accumulated phase at the central frequency ω_o and the first term on the right is the group delay in which the pulse experiences the linear chirp given by β_1. The second term is the group delay dispersion and the third order dispersion is known as cubic phase distortion. This ultimately leads to a mismatch between the chirp of the incident pulse and that of the compressor. A number of researchers have tried to compensate for the higher order terms (e.g., third-order) by adding a small positive or negative delay line immediately after the fiber stretcher. This can be done by pre-chirping the stretched pulse via the mini-compressor. (35, 36).

Grating based compressors operate off the fundamental grating equation:

$$m\lambda = d(sin\theta_{in} + sin_{out})$$

Where the dispersive delay can be written as the change in pulse duration with respect to wavelength:

$$\frac{\partial\tau}{\partial\lambda} = \frac{m^2}{d^2}(\frac{b\lambda}{c[1 - [m\lambda - sin\theta_{in}]}$$

Here m is the mode, d is the groove spacing and b is the slant distance between the gratings. For the compressor in this project the gratings chosen have a period of 575nm or 1740 lines/mm. The gratings are aligned in a Littrow configuration in which the

incident beam and the diffracted returning beam is reflected back in the direction of the incident beam. At Littrow, the grating equation simplifies down to:

$$\theta_B = arcsin(\frac{m\lambda}{2d})$$

The compressor used in this project is shown below. The input angle is 61.1° on the small grating and returns at 61.1°.

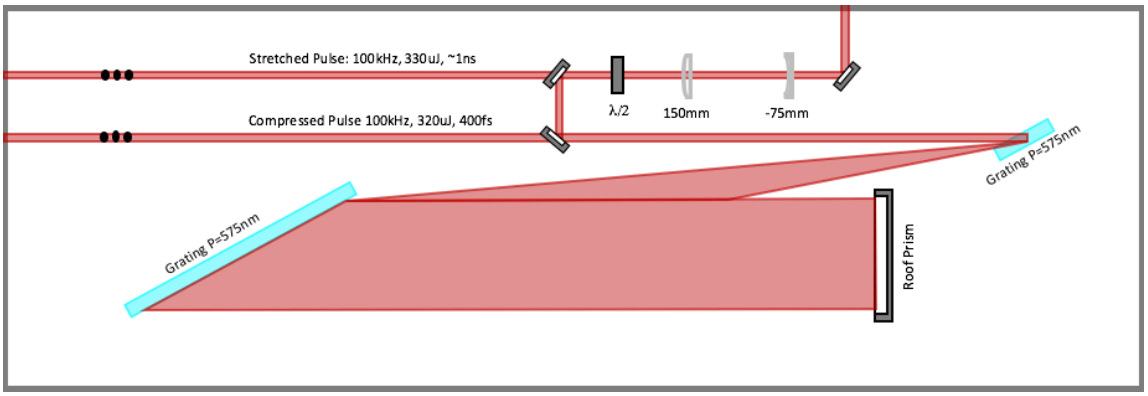

Figure 6.1: The gratings were obtained from the Fraunhoffer institute with a reflectance of 98.3% per pass. The grooves have a period of 575nm/1740 l/mm The waveplate after the telescope is used to switch the pulse into the compressor by reflection off a polarizer.

Alignment of the gratings is extremely sensitive. Misalignment of the gratings induces higher order dispersion phase correction. This in turn leads to slightly shorter pulse down at ~386fs. However, this induces a spatial chirped across the pulse which can be seen in the spectrometer output and thus lowers further harmonic conversion. For a transform limited pulse then assuming only group velocity dispersion is being taken into account, the dispersive delay then for an input angle of 61.1° the dispersive delay then is ($0.619x10^{-11}$ * b)(nsec/nm). The grating spacing is 1m making the dispersive delay 0.062 nsec/nm. The autocorrelation of the compressed pulse is shown below.

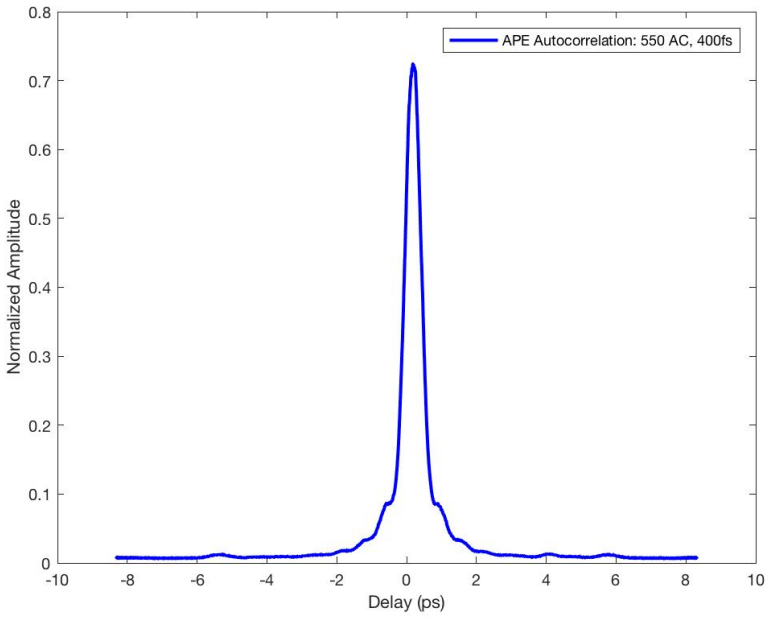

Figure 6.2 Second-Order Autocorrelation of the compressed pulse (FWHM= 400 fsec) (I used an APE second harmonic noncollinear interferometric autocorrelator).

The pulse duration can be changed from 400fs-1picosecond by tuning the mini-compressor which changes the negative chirp experienced by the stretched pulse. The wings seen in the autocorrelation are indicative of a fiber chirped pulse amplification system due to the higher order mismatch between the fiber stretcher and grating based compressor. This mismatch can be reduced by adding a prism based compressor after the grating compressor and/or a spatial light modulator after the main amplifier. Group delay dispersion has strong effects in prism-pair compression. A prism pair always has negative group delay dispersion. The angular dispersion and group delay dispersion are described here as a function of the path difference and material dispersion in the prism. (32)

$$\frac{\partial^2\phi}{\partial\omega^2} \approx -4L_{sep}\frac{\lambda_0^3}{2\pi c^2}\left(\frac{\partial n}{\partial\lambda_0}\right) + L_{prism}\frac{\lambda_0^3}{2\pi c^2}\frac{\partial^2 n}{\partial\lambda^2}$$

The first term on the right describes the total amount of angular dispersion which from a prism pair is always negative. The second term on the right describes the beam passing through some prism of length (L) and material, this term is always positive in the visible and near-IR. By varying the separation between the prisms, course group delay dispersion tuning can be done. By angle tuning the prism the prism pair can then be wavelength tuned. Finally, by increasing the path length through the prism, fine tuning of the group delay dispersion can be done. Below is an example of a 4 prism compressor used for course and fine tuning of group delay dispersion. (32)

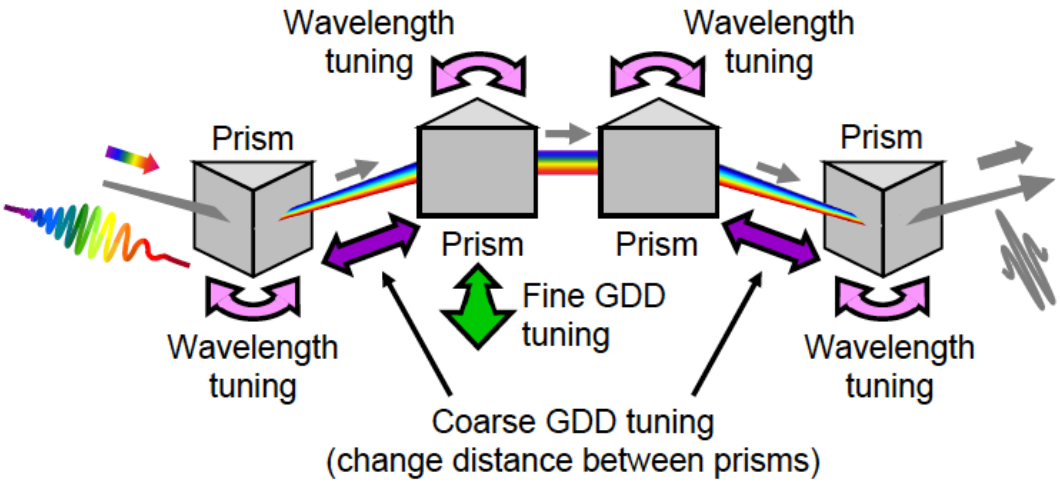

Figure 6.3 Four prism pulse compressor. A prism pairs could be used after the grating compressor to reduce the fundamental pulse duration from ~400fs to ~330fs. In the UV the dispersion terms both become negatively allowing for extreme group delay dispersion compensation in the UV. (fig. taken from Ultrafast Optics lectures by Rick Trebino)

Prism compression involves its own difficulties. Slight misalignment in the incident angles dramatically increased residual angular dispersion, spatial chirp, and pulse-front tilt in the output pulse. (32)

7. Harmonic Generation

As discussed in Chapter 1, exposure of optical materials to strong electromagnetic fields creates a polarization of the material, P, that exhibits both linear and nonlinear response to the applied electric field, E

$$P = \epsilon_o(\chi_1 + \chi_2 E + \chi_3 E^2 + ...)E = P^{(1)} + P^{(2)} + P^{(3)} + ...$$

The first term is the normal linear response with a dielectric susceptibility, $\varepsilon = \varepsilon_0\chi_1$. The second term, $\varepsilon_0\chi_2 E{:}E$, represents the lowest order nonlinear response. We can see that the if the dielectric response tensor is large enough, the polarization will have a significant component oscillating at double the frequency of the fundamental applied field (1). This is known as 2nd harmonic generation. Energy flow between polarization waves to the EM waves can be characterized by its coherence length, given by $\pi/\Delta\mathbf{k}$. The longer the 2ω polarization wave is in phase with the 2ω EM wave, the larger is the transfer of energy (2). Nonlinear polarization and the driving term for the formation of harmonic radiation is discussed in chapter 3. For Second Harmonic Generation, a second-order polarization radiates at angular frequency, ω_3 and a corresponding wave vector, $\mathbf{k}_3$. Constructive interference requires that both energy and momentum are conserved:

$$\omega_3 = \omega_1 + \omega_2 \qquad\qquad \mathbf{k}_3 = \mathbf{k}_1 + \mathbf{k}_2$$

Energy Conservation: Momentum Conservation (Phase Matching):

The Phase Matching Condition is achieved in three-wave mixing (harmonic generation) in birefringent materials by selecting the polarization and propagation directions to

minimize $\Delta k = k_3 - (k_1 + k_2)$. While there can be up to five phase matching types, only two are common.

Type I: Signal and Idler have the same Polarization, Pump is opposite.

Uniaxial crystal: Signal (ordinary), Idler (ordinary), Pump (extraordinary)

Type II: Signal and Idler have the orthogonal Polarization, Pump is can be either or both

Uniaxial crystal: Signal (ordinary), Idler (extraordinary), Pump (both)

In Type 1 harmonic generation, both fundamental waves have the same polarization and Type 2 they have orthogonal polarizations. Type II SHG is performed by placing the incident light at 45 deg to the crystal axis to obtain an equal mixture of ordinary (E||c) and extraordinary (E_|_c) radiation. (16)

While Phase matching is the most important factor in harmonic generation, there are several problems that must be faced. Dispersion in the nonlinear crystals results in the 1ω and 2ω pulses travelling at different speeds. Dispersion becomes a significant factor as pulse durations enter the femtosecond regime. First order dispersion causes a pulse envelope to propagate with a group velocity that generally differs from the phase velocity. This has no effect on the shape of the propagating envelope but leads to separation between the fundamental and the harmonic wave. 2nd order dispersion, known as group delay dispersion, is also a key factor for femtosecond pulses. Group delay dispersion reshapes the propagating pulse envelope. If wave mixing is also very strong the the pulse will change in amplitude and phase as well. (16)

The effects of Group velocity walk off in our system are shown in Figure 7.1. The plot shows the output of a 400 femtosecond pulse compared to that of a 1 nanosecond pulse below it of the same central wavelength. The nanosecond pulses experience almost

zero walk-off due to the long pulse duration which is why longer pulses achieve higher conversion efficiencies than shorter pulses at pico and femtosecond durations. As the red (red1, red2) walk-off from the green (blue) pulse in the femtosecond regime, the pulse continues to harmonically convert along the edge of the input fundamental pulse leading the creation of a trailing energy foot. This foot can include significant power. Further dispersion continues to spreads the foot temporally. This foot becomes a problem for optimization of the UV peak power and average power shown later.

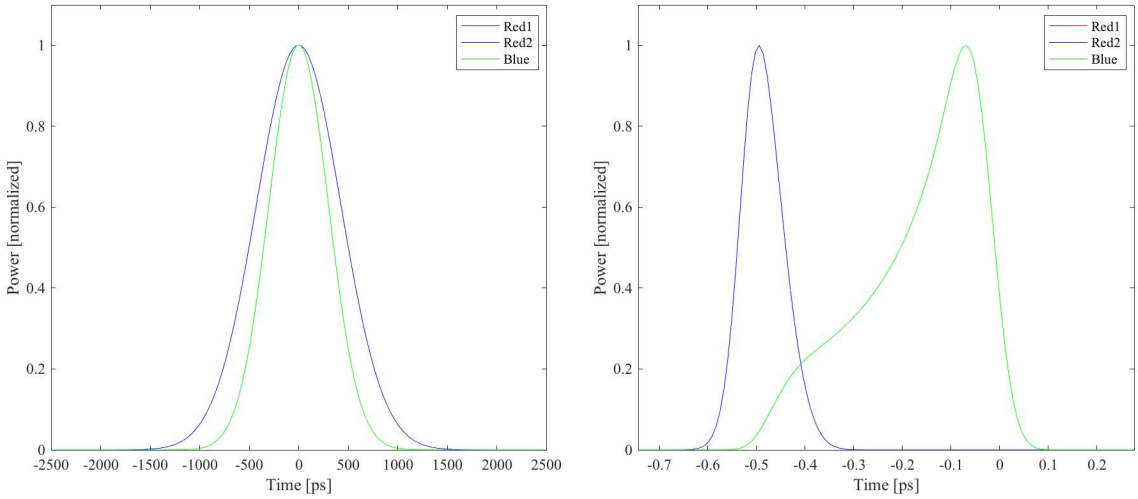

Nanosecond Harmonic Generation 100 fsec Harmonic Generation

Figure 7.1 Harmonic Generation with 1 nsec (left) and 100 fsec (right) pulses at 1047nm utilizing a 10 mm long LBO crystal. Red1 and Red2 are simply the fundamental pulse with each having ½ the energy of the fundamental pulse.

Higher order effects come as a result from using shorter and shorter pulse durations. Group Delay Dispersion chirps the second-harmonic pulse (Figure 7.2). We can see as expected the 523.5 output in the nanosecond regime acquired no chirp. However, we can see in the 523.5 output of the 400 femtosecond pulse, it has acquired a slight chirp which is attributed as before to group delay dispersion.

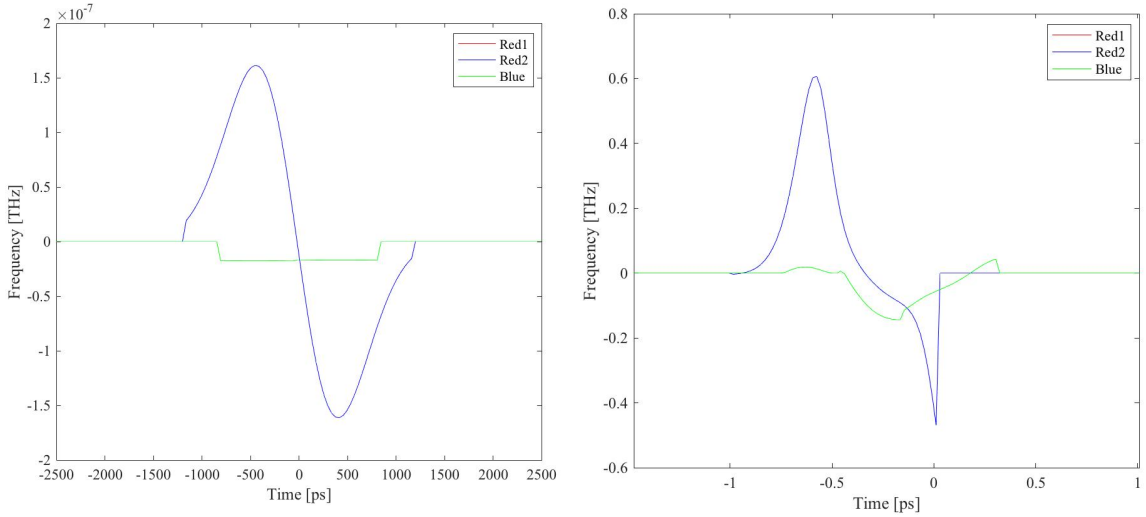

Nanosecond Harmonic Generation

400 fsec Harmonic Generation

Figure 7.2 1 nanosecond 1047nm 10mm LBO normalized frequency (Left) and 400 fsec (right). The nanosecond pulse acquires a very slight linear chirp across the entire pulse. Note the difference in scale on the ordinate.

Group velocity walk-off has a noticeable impact on the conversion efficiency within the crystal. If we take the crystal and slice it into slices along the propagation axis we can determine the effects of each z-slice individually and how it effects the overall efficiency of the crystal. Each piece along the propagation axis radiates a pulsed 2^{nd} harmonic field with duration τ with an amplitude proportional to the square of the fundamental field. As we saw above the group velocity walk-off spreads the radiated pulses over time. If $\Delta k = 0$, then the time integral of the radiated 2^{nd} harmonic field is independent of the time stretching of the second harmonic pulse. For increasing values of temporal walk off we can see the harmonic field becomes that of a flat top hat (Figure 7.3).

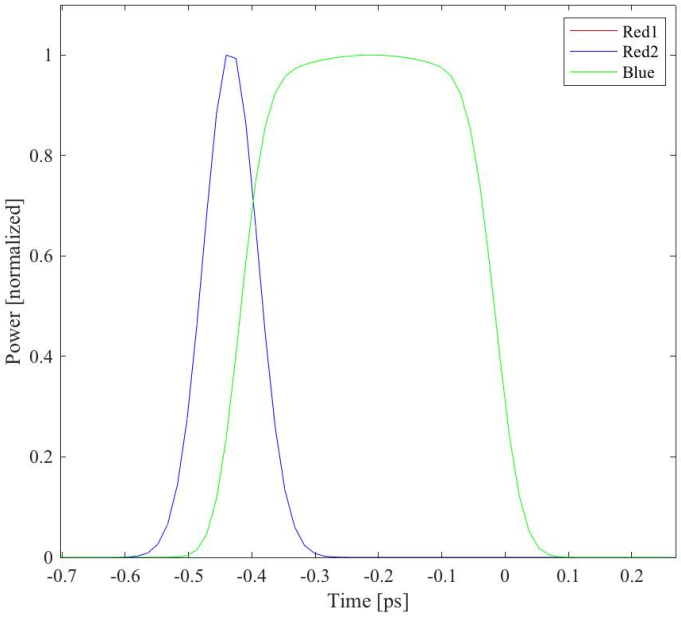

Figure 7.3 100 Femtoseconds 1064nm 10nJ 5mm BBO Normalized Irradiance vs Pulse Duration. In BBO pulses experience a larger walk-off than in LBO. In BBO using the same 100 fsec pulse, walk-off and group delay dispersion is so large that the pulse broadens in time. The walk-off can be adjusted to modulate the walk-off experienced between the two colors.

The 2nd harmonic efficiency falls with increasing group velocity walk-off between the 2nd harmonic pulse and the fundamental pulse. If Δk does not equal 0, destructive interference of the second harmonic pulses created by different slices of the fundamental pulse also jeopardize the doubling efficiency. This is easily demonstrated by taking the above pulse and adding in a large amount of phase mismatch (Figure 7.5). The first plot is with a crystal phase mismatch of 0 mrad and only the effects of group dispersion. The second plot shows the effects of 1 mrad of phase mismatch. This is best demonstrated in the spectral output of the fundamental and 2nd harmonic pulses.

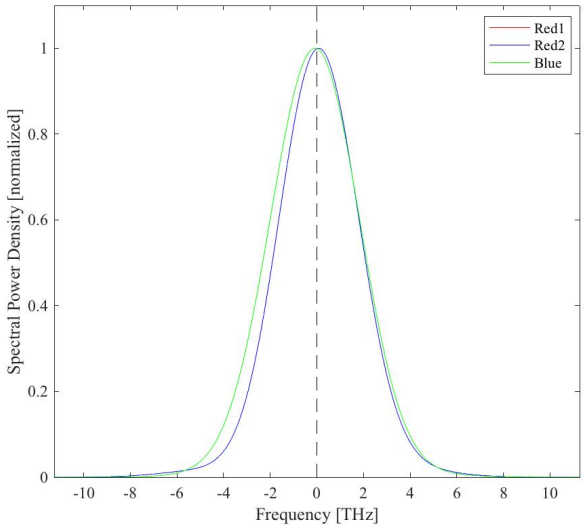

Figure 7.4 100 Femtoseconds 1064nm 10nJ 5mm BBO Normalized Irradiance vs Pulse Duration, 0mrad. The walk-off is set to zero. The spectral broadening here is due to group delay dispersion being higher in BBO in the green than the infrared. This is also why the green spectrum shows a slight tilt to the left with a sharper edge than the longer wavelength side.

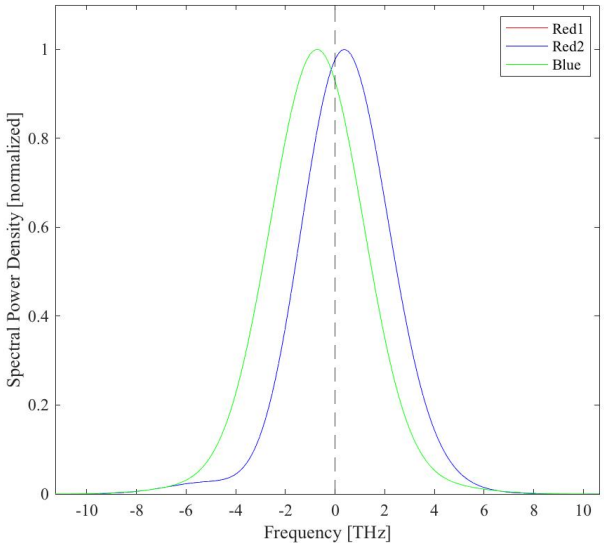

Figure 7.5 100 fsec 1064nm 10nJ 5mm BBO Normalized Irradiance vs Pulse Duration, 1mrad. This now shows the critically phase matched walk-off achievable in BBO. The spectral width is nearly the same due to BBO the pulse broadens as it travels through. The green walks-off form the infrared significantly. Both spectrums experience higher order nonlinearities associated with the mixing of ultrashort pulses in longer crystals which also leads to spectral tilt and the creation of feet as seen in the figure.

For the purposes of this Master's Thesis I have chosen to utilize the crystals LBO, BBO and CLBO. These refractive indices in BBO for example are given as $n_x = n_y = n_o$ and $n_z = n_e$ where n_e and n_o are the extraordinary and ordinary indices. In uniaxial crystals like BBO, waves with polarization along x and y are called ordinary and those along z are called extraordinary. These ordinary waves then interact only with index of refraction n_o while extraordinary waves experience an index dependent on the wave vector and the z-axis. Now in Biaxial crystals none of the indices are equal to one another making this a more complicated problem. We start by determining what the Sellmier equations are for LBO for each of the n_x , n_y , n_z axis. If we compare the literature, there are varying coefficients that have been determined by various groups. Kato et. al published values of: (37)

$$n_x^2 = 2.4542 + \frac{0.01125}{\lambda^2 - 0.01135} - 0.01388\lambda^2$$

$$n_y^2 = 2.5390 + \frac{0.01277}{\lambda^2 - 0.01189} - 0.01848\lambda^2$$

$$n_z^2 = 2.5865 + \frac{0.01310}{\lambda^2 - 0.01223} - 0.01861\lambda^2$$

K Kato et. al. Tunable UV generation to 0.2325um in LiB3O5

These values out the the 3rd decimal place are quite agreed upon in the community. However, when comparing to others such as Velsko et al. (39) we see slight variations. When comparing the Chens (38) work we see a very different set of Sellmier equations as well. The community has more recently settled upon Velskos work seen below compared to Chens.

$$n_x^2 = 2.4517 - \frac{0.01177}{0.00921 - \lambda^2} - 0.00960\,\lambda^2,$$

$$n_y^2 = 2.5279 + \frac{0.01652}{0.005459 + \lambda^2} - 0.01137\,\lambda^2,$$

$$n_z^2 = 2.5818 - \frac{0.01414}{0.01186 - \lambda^2} - 0.01457\,\lambda^2,$$

Chen et. al. New nonlinear-optical crystal LiB3O5

TABLE II
SELLMEIER COEFFICIENTS FOR LBO AT 20°C

	A	B	C	D
n_x	2.4543E + 00	1.1413E − 02	−9.4981E − 03	−1.3900E − 02
n_y	2.5382E + 00	1.2830E − 02	−1.1387E − 02	−1.7034E − 02
n_z	2.5854E + 00	1.3065E − 02	−1.1617E − 02	−1.8146E − 02

Figure 7.6 Sellmeier Coefficients for LBO at 20°C The equations are given in the text. This table was obtained from *Phase-Matched Harmonic Generation in Lithium Triborate (LBO)*, Stephan Velsko et. al. 1991, Journal of Quantum Electronics. (38)

Its clear that in the span of two years conclusions were settled on mainly for LBO and we will be considering Velskos coefficients. The Sellmier coefficients are dependent on the material and the temperature as well. This becomes a large factor in considering non-critically phase matched harmonic generation,

My simulations were performed with the Sandia Non-Linear Optics (SNLO) Code and script that I wrote in MatLab. The Matlab program models the full transverse beam profile and temporal pulse profiles of a wave mixing event. The model includes spatial walk-off, diffraction, group velocity dispersion, group delay dispersion and self-phase modulation. I focused on the following parameters for my simulations both in the femtosecond regime and the nanosecond regime to compare conversion efficiencies but 1st order vs 2nd order effects as well. I used a 400fs pulse duration with pulse energies

ranging from: 1uJ – 250uJ. Central fundamental wavelength of 1047nm and a 2nd harmonic at 523.5nm. It is well known (43) that LBO maximizes its efficiency in lower power regimes (<2GW/cm^2) cannot exceed ~70% conversion efficiency. I have examined phase mismatch parametrically in the nanosecond pulse before moving to the femtosecond regime. Here we have used 1047nm and 523.5 as fundamental and 2nd harmonics respectively. Indices of refraction were calculated from the Sellmier equations given type 1 SHG with fundamental polarization directions in the x/y planes. Crystal absorption/mm is given in (37-56) going with the lowest absorption. Pulse energies vary from 1uJ to 250uJ. I set the FWHM of the beam to 3.5mm to assume a 6x6mm entry face on the crystal given by Newlight Photonics. Radii of curvature are given from (16). Crystal length varying from 5, 10, and 15mm. Peak Irradiance is calculated in W/cm^2. The above parameters can be used to give an example of the conversion efficiency, walk off, spectral distribution etc.

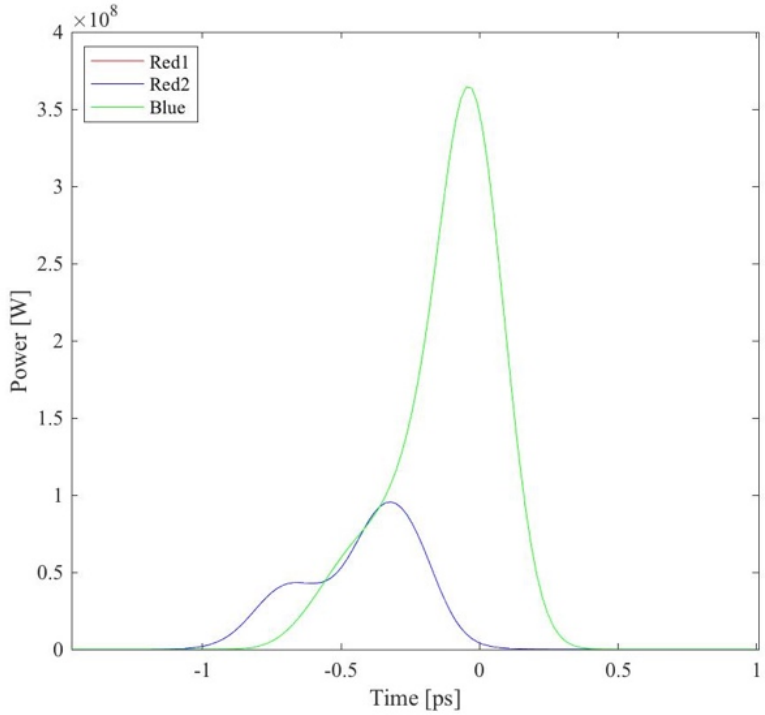

Figure 7.7 Calculated 2ω output of 400 sec, 1047nm 250uJ pulses through 10mm LBO. Beam Size = 2.2 mm FWHM

Two paths were taken when considering second harmonic generation and fourth harmonic generation. One path would utilize long crystal noncritically phase matched LBO and CLBO for high conversion efficiency. This path leads to an energy foot developed at the end of the pulse due to longer crystal lengths and dispersion. The other path focuses on optimizing peak power optimization of the second harmonic and fourth harmonic without the creation of the energy foot. This path utilizes critically phase matched very thin BBO for both the second and fourth harmonics. Two lines were setup to operate then both harmonics by flipping mirrors into and out of the beam path to choose either for peak power or conversion efficiency.

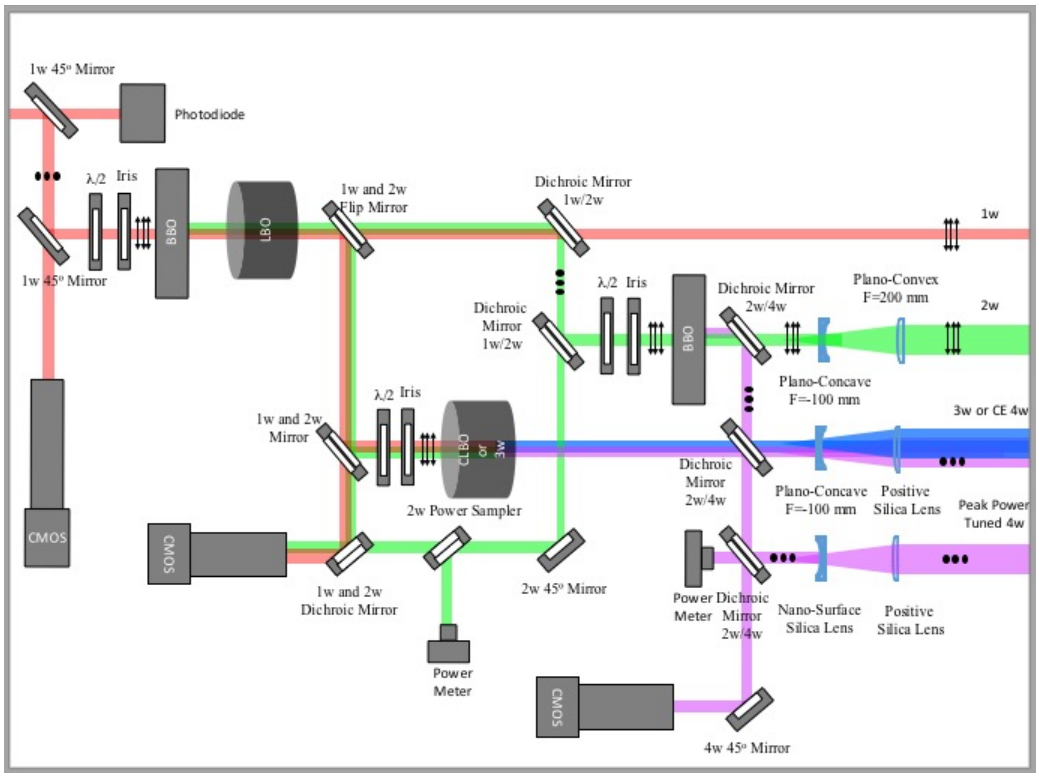

Figure 7.8 CMOS cameras are installed to monitor the beam profile at each harmonic. The beams are expanded exiting the box to avoid color center formation and continuum generation through fused silica optics after the box. Flip mirrors are placed to swap between peak power path and peak conversion efficiency path.

The fundamental light comes in with vertical (S-pol) polarization. The pulse train is measured by a fast photo diode to monitor the fundamental 100kHz. A Thorlabs cmos camera is aligned after the second turning mirror to monitor the beam quality coming from the compressor. The beam profile leaving the compressor still maintains a slight hexagon demonstrating that the compressor is well aligned. Below is the beam profile imaged at the entry plane of the second harmonic crystal.

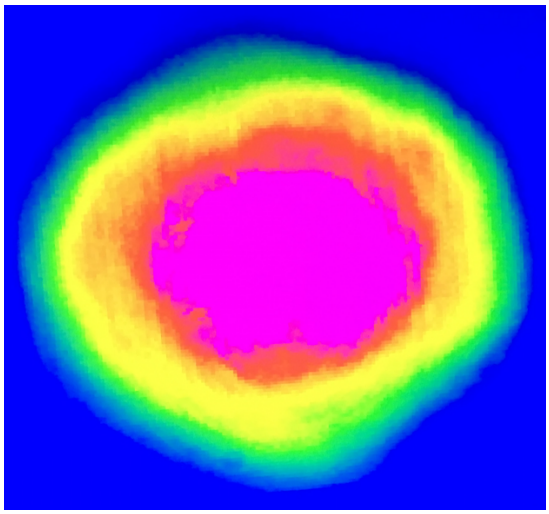

Figure 7.9 Beam profile (FWHM=2.3 mm) of the fundamental (1ω) at the entry plane of the SHG crystal.

A half wave plate is used to rotate the polarization such that the crystal receives horizontally (P-Pol) polarized light and emits second harmonic generation in vertical polarization (Type I SHG). A copper iris is placed in front of the second harmonic crystals to ensure no edges can be clipped and that uniform heating can occur within the crystal without diffraction problems.

For optimum conversion efficiency, we used non-critically phase matched LBO. Various lengths of LBO were tested from 3mm and 7mm. The LBO crystals were placed in a Crystal oven with a temperature controller enabling operation from 25.0 to 200.0^{o}C. The crystals are mounted in a brass cartridge for easy installation into the ovens (Figure 7.10).

Figure 7.10
4x4x10mm LBO crystal mounted in a oven for non-critical phase matching. The image also shows the early onset of harmonic generation at just the 1W of input fundamental power. The crystal is mounted in a brass housing.

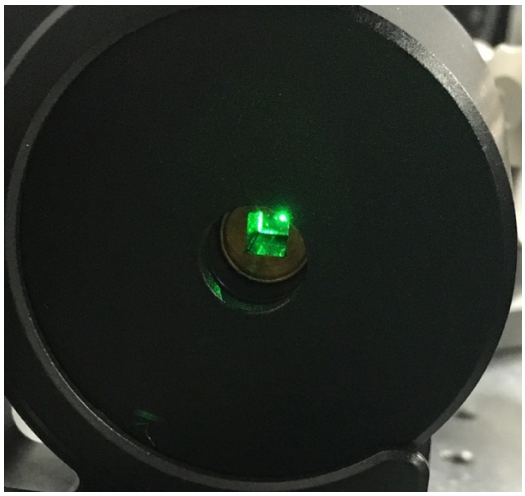

Figure 7.11
Second Harmonic beam profile at full power (>16 W at 523 nm).
The ellipticity is expected to occur due to walk-off between the harmonics in longer crystals and input slightly elliptical Gaussian beams.

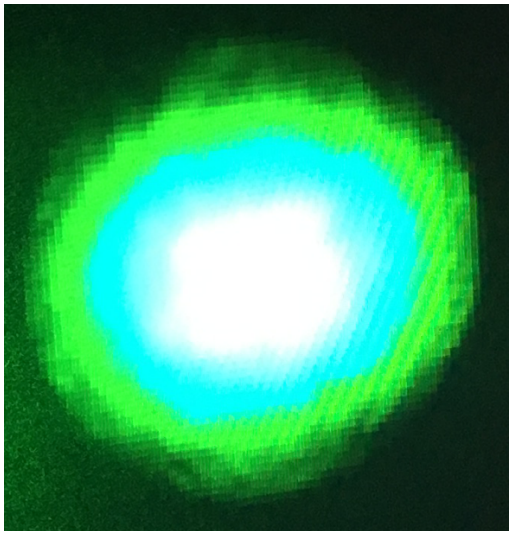

I used a CMOS camera imaged at the back plane of the LBO crystal to both enable precision alignment of the fundamental beam going through the LBO and to examine the 2ω beam quality (Figure 7.11). The beam profile is consistent with the literature. Peng et al. (32) demonstrated a high power cw Nd:YLF laser system that formed an elliptical beam with a nearly Gaussian input beam. The 2ω exhibits some ellipticity independent of the beam Gaussian input (Figure 7.12). The ellipticity in the beam is more significant in the 1053nm cw beam due to the longer crystal length as

well. The ellipticity is also due to the walk-off between the fundamental and second harmonic and lastly due to the thermal lensing of anisotropic LBO.

Figure 7.12
Beam profiles (top) the input fundamental at 1053nm and the second harmonic (bottom) at 526.5nm generated in 30mm, NCPM LBO. (32)

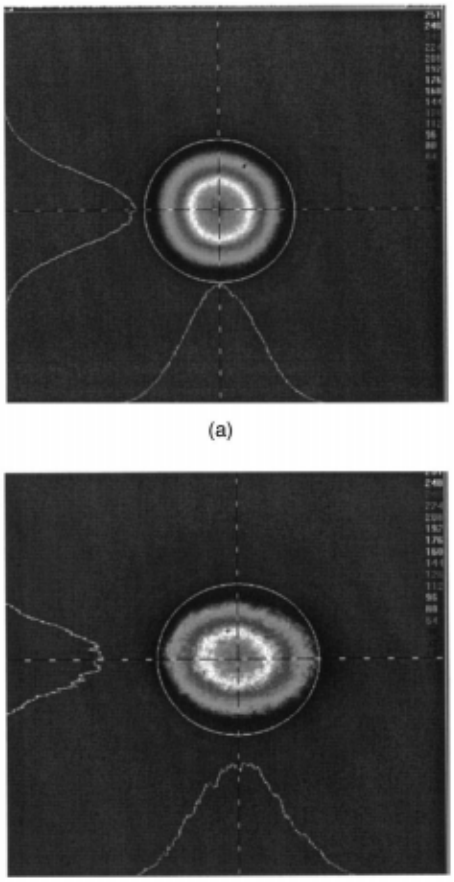

Once the harmonic system was aligned with the 4x4x10mm LBO, two other LBO crystals, 6x6x3mm and 6x6x7mm were employed. The 6x6x7mm LBO was first tested for peak conversion efficiency. The mini-compressor was tuned to allow for pulse durations from 400fs to 1ps in the conversion efficiency regime which optimized the pre-chirp before compression which led to quite dramatic effects in the conversion efficiency. At ~600fs and a mini-compressor spacing of 15.6 mm, the maximum conversion achieved from the 6x6x7mm LBO crystal was 18.6W at 29W of input fundamental resulting in 64% conversion efficiency to the second harmonic. This matched closely to the

theoretical model for 6x6x7 LBO which was 19.6W at 29W input. Dergachev et al (52) showed also that LBO for ns pulses was phase matched at 170°C operating at 1047nm Nd:YLF. They achieved 68% conversion efficiency using 20mm long LBO resulting in 45W of 523nm.

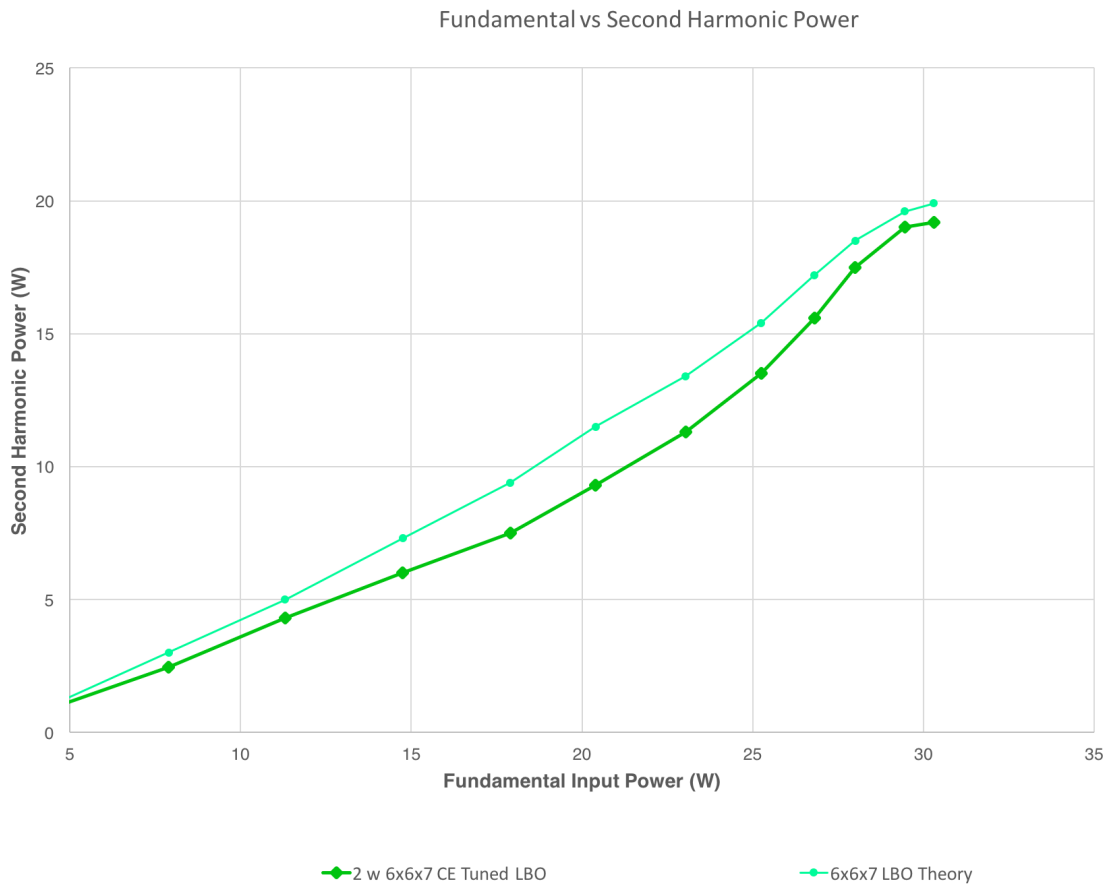

Figure 7.13 Output 2ω vs input 1ω for the 6x6x7 mm Non-Critically Phase Matched LBO crystal and comparison with theory. Input pulse duration = 400 fsec, 1047 nm, FWHM = 2.2 mm

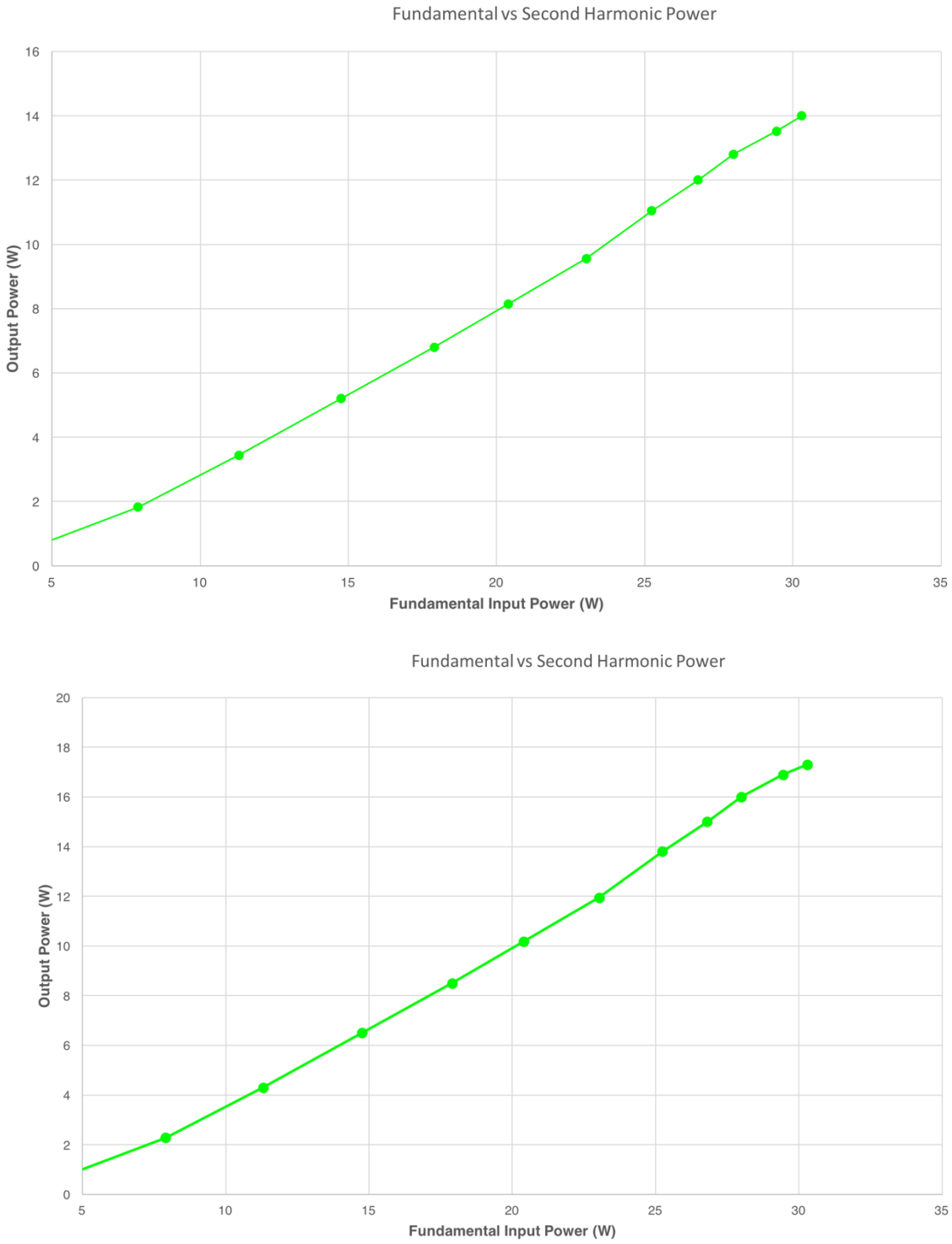

Figure 7.14 Output 2ω vs input 1ω for Type I BBO crystal. Top: 6x6x1.5 mm, Bottom: 6x6x2.0 mm, Input pulse duration = 400 fsec, 1047 nm, FWHM = 2.2 mm

Note that the 2ω pulse is not quite Gaussian due to multiple nonlinear effects experience by the femtosecond pulse in a picosecond crystal. The pulse forms a "foot" due to walk-off between the 1047nm and 523nm pulses. As the pulse travels through the crystal the initial peak power walks-off while the pulse continues to generate second harmonic light. The other large factor in play here is the reconversion of 523nm pulse back into 1047nm.

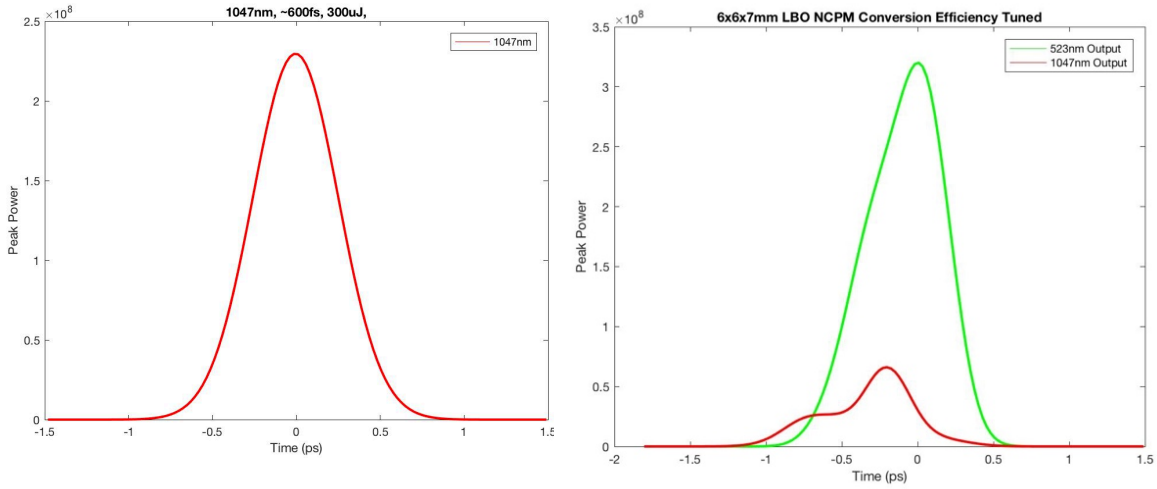

Figure 7.15 Left: Input fundamental 1ω. FWHM 600fs, 300uJ, 1047nm 750MW peak power incident on a 6x6x7 mm NCPM LBO. Right: Output 2ω (green) and residual fundamental pulse (red) 523nm pulse.

In LBO the indices of refraction for 1047nm and 523nm were 1.606 and 1.606 respectively with group velocity indices given by 1.626 and 1.640. The group delay dispersion was set to 18.5fs^2/mm and 89.7fs^2/mm. The GDD experienced in LBO is about half of that in BBO leading to a higher peak power formed in LBO which will be discussed later. Input and output reflectivity was set to 1% with 1% absorption/mm. The given self-phase modulation n_2 values for 1047nm were ~0.5×10^{-16} cm^2/W and 523nm ~1.0×10^{-15} cm^2/W. The self-phase modulation terms for IR are typically 5-10x lower than green and UV. Self-phase modulation becomes a large factor with the UV as seen later. Two-photon absorption was not included in this calculation as the two photon absorption

energies for even two green photons do not meet the 180nm transmission cut-off of LBO making this term rather negligible. Pulse energy was set to 300uJ total. Beam diameter was set to 2.2 mm with a walk-off of 1.15 mrad after non-critically phase matching. Deff was 0.851pm/V with a phase mismatch of $\Delta k = 0.05/mm$. Peak powers are shown in the plot above. The green pulse is shorter than the input IR pulse.

NCPM allows for minimal alignment difficulties and out of the box temperature tuning. Below is a temperature tuning plot for input 1ω average power of 3.5W, pulse energy 35uJ. This is consistent with most publications on the temperature dependent phase matching. (list publications)

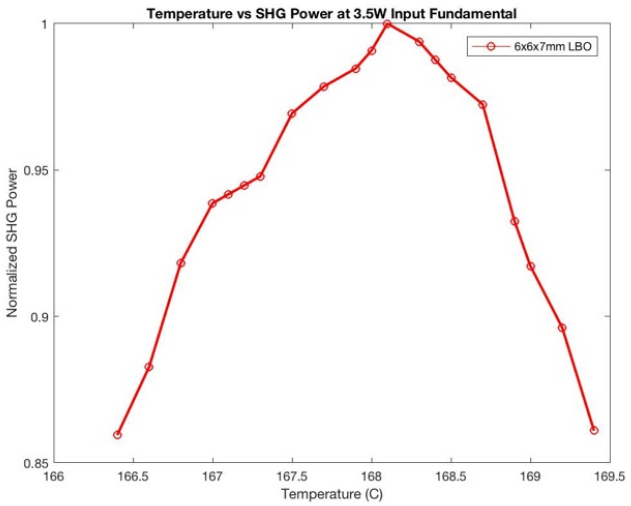

Figure 7.16 Temperature tuning plot for 6x6x7mm LBO. At 3.5W the crystal was phase matched at 168.1°C. At 30 W average power input, the oven temperature was dropped to 166.9°C for optimum conversion. This is thought to be due to heating in both the crystal and the mount.

At 3.5W, 35uJ of input 1047nm 400fs pulses the temperature is peaked at 168.1°C. When the power is increased to 30W, 300uJ, the temperature rises due to absorption in the LBO crystal therefore the temperature had to be reduced to 166.9° when operating for long periods. This phase matching temperature worked consistently with the 3mm LBO crystal and 166.9° was also used as the peak power temperature. Our NCPM temperature

is in good agreement with Ukachi et al. who measured the non-critical phase matching temperatures given various IR wavelengths in LBO for SHG.

In conclusion the 7mm LBO crystal due to the length of the crystal experiences more linear and nonlinear dispersive effects than the thin crystals. Walk-off and reconversion are more severe than that experienced by the thinner crystals. The pulse broadens due to temporal walk-off and dispersion between the 1047nm and 523nm pulses. The leg that is produced in the green and the residual hump given in the red indicate that the pulse underwent reconversion at 4.5mm peaking at 3mm and re-peaking after the first reconversion cycle back at 7mm. The beam was moved around the aperture of the crystal and the oven was placed in an θ–ϕ rotation mount to allow for slight misalignment going into the crystal. This misalignment of milliradians has been shown to slightly increase conversion efficiency due to forced higher order phase mismatch correction by misaligning the input beam from a perpendicular input. Our data (19.6 W of 2ω) is in good agreement with our model calculation (20.4 W predicted). The 7mm crystal is optimized maximum conversion efficiency, not for maximum peak power.

The key to maintaining peak power is to minimize walk-off and crystal length and before the first reconversion cycle. 6x6x3mm LBO was therefore employed as the next crystal to be optimized for peak power rather than overall conversion efficiency. The theoretical model predicts a conversion efficiency of 56% at 16.6W of 523nm from 30W of 1047nm input for the 3 mm long crystal (Figure 7.22). This matches closely to the experimental values at 15.5W with ~7% error.

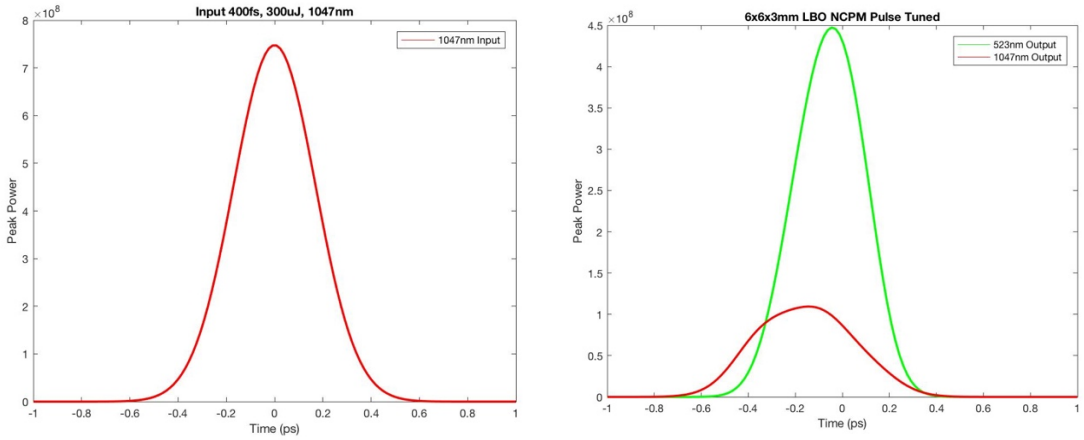

Figure 7.17 Left: Input fundamental 1ω. FWHM 400fs, 300uJ, 1047nm 750MW peak power incident on a 6x6x3 mm NCPM LBO. Right: Output 2ω (green) and residual fundamental pulse (red) 1047 nm pulse.

Unlike the output green pulse from the 6x6x7mm LBO, the pulse from the 3mm LBO show no creation of a foot. Efficient conversion has happened before spatial walk-off and reconversion can occur. The pulse is optimized for peak power. The resulting peak irradiance is 9.4 GW/cm^2 at 523nm. The pulse duration is ~390fs due to the spectral broadening from initial harmonic conversion. The peak power is 450MW. Here self-phase modulation becomes a limiting factor. Driving higher peak irradiance induces earlier reconversion at shorter crystal length also reducing conversion efficiency. This could be avoided by going to shorter crystals. A smaller beam size could be used to increase input irradiance but is limited by increasing self-phase modulation terms as peak irradiance climbs above 10GW/cm^2. In the case of peak power optimization, it is clear the green pulse is shorter than the input red pulse for the short, 3 mm crystal. The red pulse has also experienced walk-off which results in a temporally shift spectrum and pulse duration relative to one another. Below is a normalized spectral distribution plot where its clear the green spectrum has been broadened by initial harmonic generation but has not undergone significant walk-off and dispersion such that the pulse broadens. \

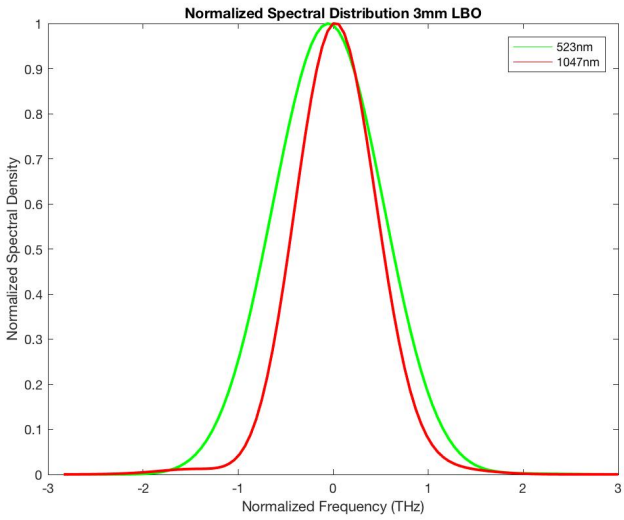

Figure 7.18 Normalized Spectral Distribution for 6x6x3mm LBO

In this case the 3mm LBO has been optimized for peak power conversion. The crystal is long enough to allow for maximum peak conversion before the onset of dispersion in the green broadens the pulse and also before the first reconversion cycle allowing the pulse to maintain a near-Gaussian profile. The 3mm LBO is therefore the crystal of choice for peak power optimization for non-critically phase matched second harmonic generation. The average power achieved was 15.5W experimentally with 16.6W theoretically resulting in 450MW of peak power at 523nm.

Critical Phase Matching

Critically phase matched second harmonic generation requires angle tuning to compensate for phase mismatch in the crystal rather than raising the temperature. Critical phase matching second harmonic generation was done experimentally and theoretically using BBO. BBO is far less hydroscopic than LBO. Unlike LBO, BBO is a uniaxial crystal meaning that 2 of 3 principal indices of refraction are equal, in the case of BBO $n_x = n_y = n_o$ and $n_z = n_e$. In critical phase matching requires that the crystal be be set at an angle such that the refractive index of the fundamental pulse becomes equal to that of the

extraordinary refractive index. In uniaxial crystals the extraordinary refractive index can be solved once the Sellmier equation is solved as mentioned earlier. The input angle dependent extraordinary index of refraction can be calculated by Ralchenko et al. (54)

$$n_e^{2\omega}(\theta) = \frac{1}{\sqrt{\left(\frac{cos(\theta)^2}{(n_o^{2\omega})^2} + \frac{sin(\theta)^2}{(n_e^{2\omega})^2}\right)}}$$

Given the Sellmier parameters from Davis et al. the phase matching angle to be 24.1^o at 1047nm in BBO. As mentioned before Boyd and Kleinman (see that paper above) described that a slight offset of phase matching angle for small crystal length actually helped increase conversion efficiency. This is a very small amount of offset in alignment of the crystal so overall design remains the same.

Critical phase matching like non-critical phase matching can be thought of as a two-step process. The incident light drives a small nonlinear polarization perturbation that oscillates at twice the frequency of the input light. The second step involves the the generation of the second harmonic light. The input wave generates a set of dipoles within the crystal that all radiate weakly at double the frequency of the input wave. Phase matching involves then the assurance that the induced dipoles then all radiate in phase adding up constructively rather than destructively which leads to the reconversion as seen in the long LBO crystal.

BBO exhibits larger walk-off, group delay dispersion, and group velocity dispersion than LBO. Tamosauskas et al. (56) redefined the Sellmeier equations for BBO and collected all the current literature on phase matching of BBO. The phase matching angles are good down to 188nm UV generation far exceeding the required

523nm and 262nm later. The Sellmeier equations are shown below for the range of 0.188 – 5.2um. (56)

$$n_o^2(\lambda) = 1 + \frac{0.90291\,\lambda^2}{\lambda^2 - 0.003926} + \frac{0.83155\,\lambda^2}{\lambda^2 - 0.018786} + \frac{0.76536\,\lambda^2}{\lambda^2 - 60.01},$$

$$n_e^2(\lambda) = 1 + \frac{1.151075\,\lambda^2}{\lambda^2 - 0.007142} + \frac{0.21803\,\lambda^2}{\lambda^2 - 0.02259} + \frac{0.656\,\lambda^2}{\lambda^2 - 263},$$

Here wavelength is in micrometers.

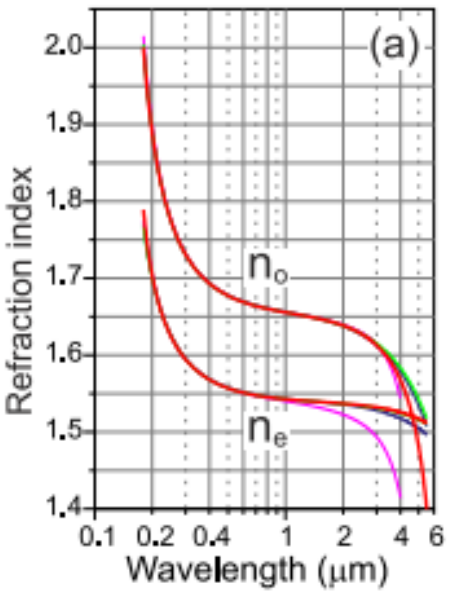

Figure 7.19
Dispersion curves are for both extraordinary and ordinary refractive indices in BBO. The curves have matched experimental data exactly in the range of 0.253 – 2.325um. (56)

BBO was next tested for peak power optimization. The mini-compressor was tuned to 15.775mm to use 400fs pulse durations. BBO crystals were kept thin due to the larger walk-off and GDD than in LBO. At 1047nm BBO has group velocity indices of 1.674 and 1.701 for 1047nm and 523nm, respectively. The group delay dispersion is more than double in the IR in BBO than in LBO and nearly double in the green at 523nm. Group delay dispersion at 1047nm was 45.7fs^2/mm and 131.2fs^2/mm. Similar to LBO input and output coating reflectivity was set to 1%. Absorption was set to 1%/mm. Self-phase modulation term n_2 for 1047nm was 5e-16cm^2/W and for 523nm it was 1e-

15cm^2/W. For IR to green second harmonic conversion two photon absorption can still be neglected as it is below the required pulse energies of 190 nm combined. Pulse energies were set to 300uJ. As with the LBO the pulse energy is split in two to allow for wave mixing to occur within calculation. The plots for one half input pulse and the full output second harmonic pulse with the residual IR.

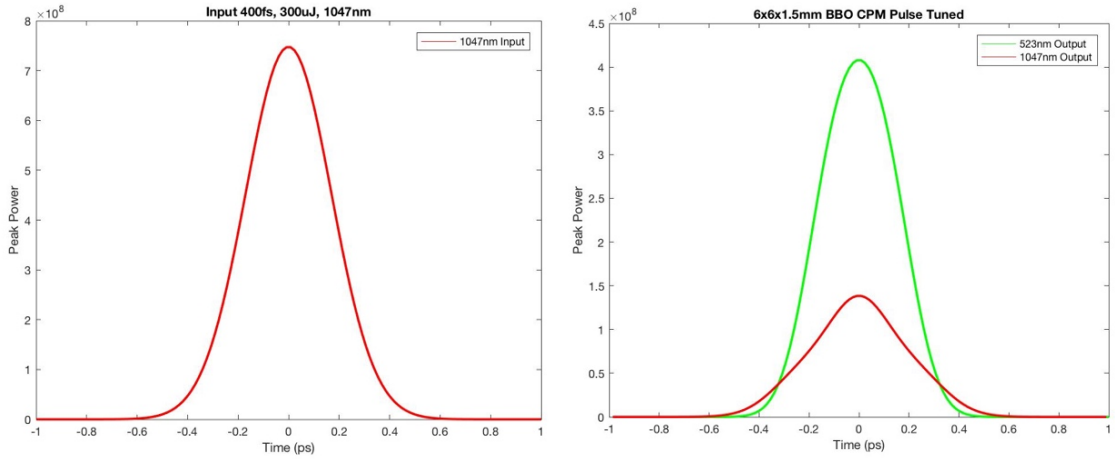

Figure 7.20 Left: Input fundamental 1ω. FWHM 400fs, 300uJ, 1047nm 750MW peak power incident on a 6x6x1.5 mm Type I BBO. Right: Output 2ω (green) and residual fundamental pulse (red) 1047 nm pulse. Beam input FWHM = 2.2 mm

Beam diameter was set to 2.2mm input with a calculated compensated walk-off was 56.4mrad at room temperature and a d_{eff} of 2.01pm/V. 1.5mm BBO shows the peak power obtainable before dispersion and walk-off sets in and the pulse begins to broaden. The resulting second harmonic pulse is again narrower with a broader spectrum than the input fundamental. The pulse shows clean conversion to 523nm with very minimal walk-off between the input and second harmonics. The resulting peak power in the green was 410MW with 161uJ pulse energy. The results in a pulse duration of 392fs as expected. Below is the plot of the normalized spectral distribution which confirms the shorter pulse duration in the green than in the IR. The residual IR maintains a semi-Gaussian shape due the very short crystal length.

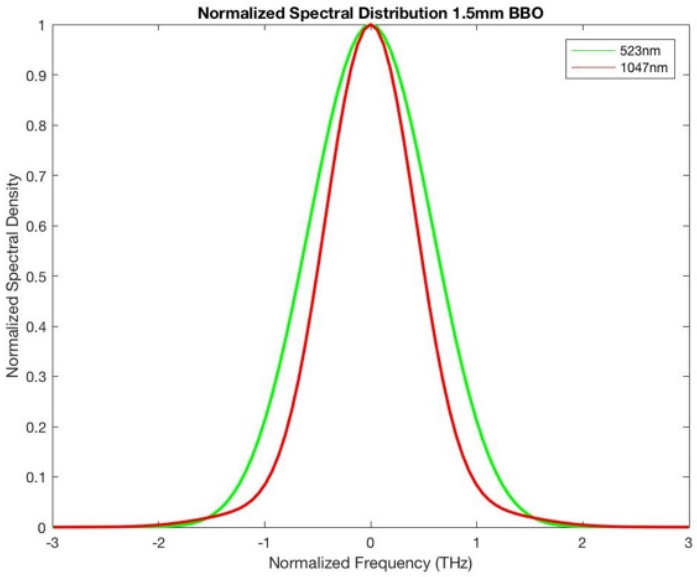

Figure 7.21 Normalized Spectral Distribution for 6x6x1.5mm BBO

For second harmonic conversion to 523nm BBO was obtained from Eskma Optics in Lithuania. 1.5mm and 2mm crystals were all obtained with plots shown later for 2mm.

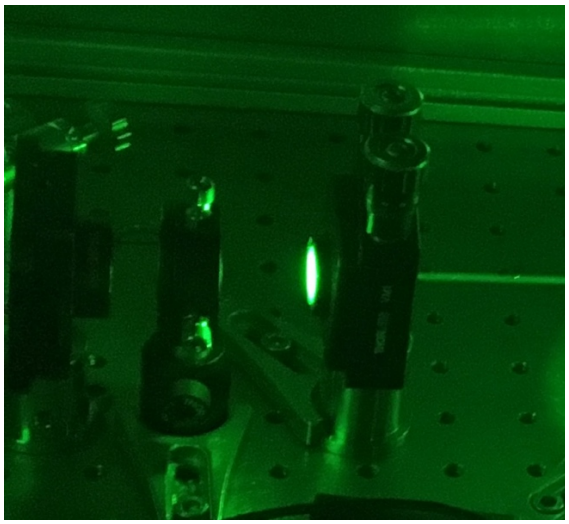

Figure 7.22 Image of critically phase matched BBO operating at 15W of average power. The BBO is placed in a vertical mount for ease of tuning at high powers.

The experimental power achieved with 1.5mm crystal was only 14W at 523nm. This is 2W or 13% less than the theoretical calculations. There are a few reasons the calculations are different from experiment. As with the LBO the input beam is assumed

to be perfectly Gaussian which it is not and has slightly amount of ellipticity. The input fundamental pulse also has higher order dispersion terms that do not give a transform limited pulse. This has been shown to dramatically reduce conversion efficiency in thin crystals as longer crystals can make up for higher order dispersion terms in means of conversion efficiency. It is clear then for 400fs pulse durations BBO crystals longer than 1.5mm should be used to achieve more than 50% conversion efficiency in experiment. 47% was achieved with the 1.5mm BBO crystal. The 1.5mm crystal therefore should not be recommended for high conversion efficiency if the next harmonic stage is the be doubled again. However, 1.5mm BBO does present a viable option for 3rd harmonic generation. Third harmonic requires 50% input IR and 50% input green making 1.5mm BBO at 400fs a great option. The next crystal that was tested was the 2mm BBO (Figure 7.23).

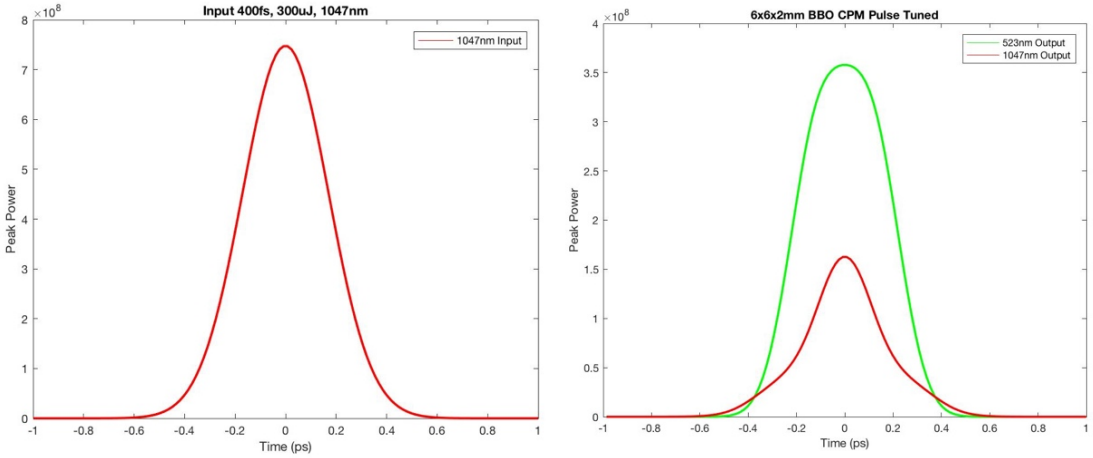

Figure 7.23 Left: Input fundamental 1ω. FWHM 400fs, 300uJ, 1047nm 750MW peak power incident on a 6x6x2.0 mm Type I BBO. Right: Output 2ω (green) and residual fundamental pulse (red) 1047 nm pulse. Beam input FWHM = 2.2 mm

The green pulse has broadened in comparison to that of the 1.5mm green pulse. This reduces the peak power but achieves higher average power. The pulse broadens due to walk-off again between the red and green pulse and the dispersion of the green in BBO

is almost double that of LBO. This is why in 3mm LBO the Gaussian peaked pulse maintains its shape whereas in 2mm BBO dispersion is high enough already that the green pulse broadens after 1.5mm. It should be noted that the walk-off and dispersion is slower than in LBO such that the pulse broadens rather than generating a foot. The green pulse in this case generates 16.4W theoretically. These parameters did not change between the 1.5mm BBO and 2mm BBO but the experimental results were shocking. 17.8W was achieved from the 2mm BBO resulting in over 23% increase going from 1.5mm to 2mm. 2mm BBO resulted in 178uJ pulse energy and 59% conversion efficiency to the green. This allowed for BBO to be the most optimized crystal in terms of peak power. The resulting calculated pulse duration was 400fs in the green giving 445MW of peak power. This is highly comparable to the peak power achieved with 3mm LBO being at 450MW. The pulse through the LBO however is ~390fs therefore shorter and does not start to take a flat top pulse shape like in the BBO.

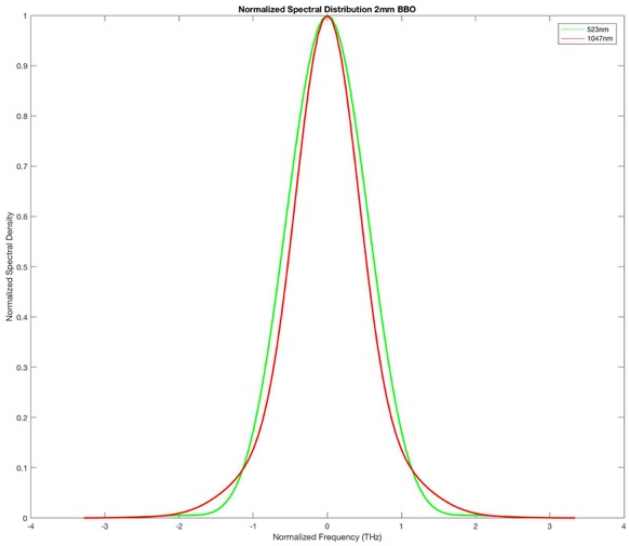

Figure 7.24 Normalized Spectral Distribution for 6x6x2mm BBO

In conclusion, the 2mm BBO seems to be the better option optimizing 4^{th} harmonic power over the 1.5mm BBO crystal. The theoretical model shows the much smaller difference in conversion efficiency than the experimental data. The BBO was easily critically phase matched due to the wide acceptance angle. BBO will also be used to convert the green now to the UV.

8. Fourth Harmonic Generation

BBO and CLBO are the two most commercially available nonlinear optical crystals for UV harmonic generation. Each crystal has distinct advantages. CLBO is non-critically phase matched where the BBO is critically phase matched. The CLBO crystal optimizes for conversion efficiency while BBO is optimized for peak power at 4 ω. The measured transparency range of CLBO is 180nm to 2750nm. (CLBO properties papers). The absorption edge of CLBO is 10nm and 20 nm shorter than that of BBO at 190nm and LBO at 200nm, respectively. CLBO exhibits very high bulk laser damage threshold of 26 GW/cm^2. BBO only exhibits about half of that at 13.5GW/cm^2. The Sellmier equations for wavelengths 240nm – 1064nm are,

$$n_o^2 = 2.2049 + \frac{1.10259 \times 10^{-2}}{\lambda^2 - 1.18119 \times 10^{-2}} - 6.95625 \times 10^{-5}\lambda^2$$

$$n_e^2 = 2.05936 + \frac{8.64948 \times 10^{-3}}{\lambda^2 - 1.28929 \times 10^{-2}} - 2.67532 \times 10^{-5}\lambda^2$$

$$633\ \text{nm} \leq \lambda \leq 1064\ \text{nm}$$

$$n_o^2 = 2.14318 + \frac{1.58749 \times 10^{-1}}{\lambda^2 + 1.37559} - 6.2375 \times 10^{-4}\lambda^2$$

$$n_e^2 = 2.04195 + \frac{2.73245 \times 10^{-2}}{\lambda^2 + 2.86672 \times 10^{-1}} - 3.42718 \times 10^{-4}\lambda^2$$

The resulting dispersion curves for ordinary and extraordinary refractive indices are given below as well as the walk-off angle for CLBO and BBO. The walk-off in CLBO at 1.83^o is less than half of the walk-off experienced in BBO at 4.8^o at 532nm. CLBO also exhibits larger angular bandwidth and spectral bandwidth at 532nm than BBO. CLBO is however extremely hygroscopic and therefore is used here only in noncritical phase matching at elevated temperature.

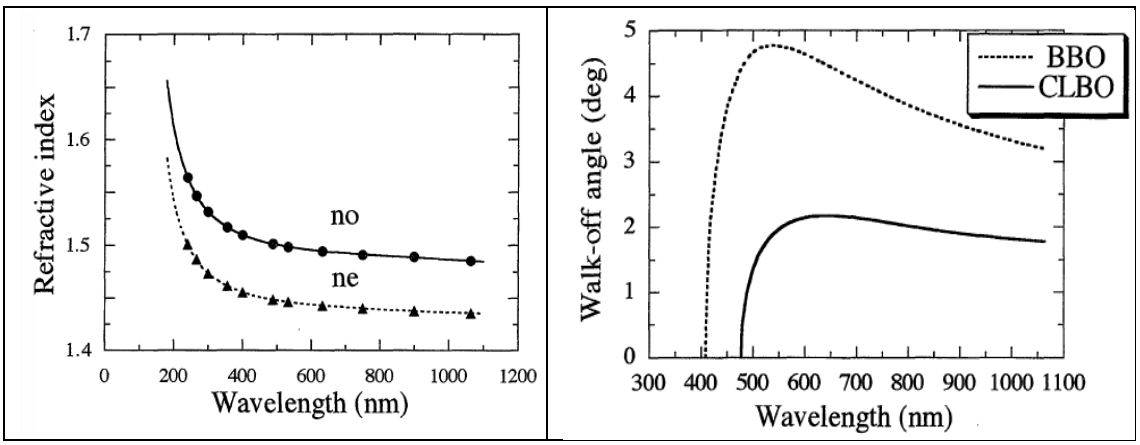

Figure 7.25 Left: Refractive indices vs for CLBO. Right: Walk-off angle for type 1-SHG as a function of wavelength. (58)

The highest average power UV fiber laser system to date is from late 2017. The Fraunhofer Institute group achieved 4.6W of average power at 258nm from fourth harmonic generation in BBO with a 800kHz 80W average power fiber laser system operating at 1030 nm and 250fs pulse duration. With an estimated pulse duration of 150fs at 258nm this system produced the highest peak power achieved to date, 38 MW but only achieved a conversion efficiency of 5.7%. They note that thermal lensing and two-photon absorption are limiting. We seek to achieve a peak power of more than 100 MW and more than 40 microjoules per pulse at 262 nm. This is nearly an order of magnitude higher pulse energy with a comparable average power of ~5 W.

BBO was the first NLO crystal to be tested. BBO was kept thin at 1mm and 1.5mm due to increased dispersion and walk-off in the UV. The beam diameter is 2.2 mm FWHM. The input pulse duration from the second harmonic is ~390fs. We included two photon absorption and self-phase modulation in our model calculations. Note that two photon absorption is important for both two 262 nm photons and for a single 262 nm

photon combined with a single 523 nm photon. Both paths reach above the absorption edge at 190 nm in BBO. With two-photon absorption included in the calculations the conversion efficiency drop by 30% (71) The two-photon absorption causes inhomogeneous heating of the crystals resulting in thermal mismatches and decreased phase mismatching. When the two-photon absorption becomes intense, the creation of color centers becomes apparent which increases linear (single-photon) absorption of both 262 and 523 nm radiation. Self and cross phase modulation also reduce harmonic conversion in the realm of femtosecond mixing. n_2 values for green are on the order of $1x10^{-15}$ cm^2/W and $1.5x10^{-15}$ cm^2/W for the UV in this case. (SNLO notes) For nanosecond pulses and longer, these are not significant issues as the irradiance is too low for significant two-photon absorption and self-phase modulation to occur. Note that long crystals and low irradiance is not possible for FHG since the crystal length must be <~2 mm to prevent walk-off and pulse broadening from group velocity dispersion. The cross phase-modulation terms were not included in calculation. The two-photon absorption term for the UV was $2x10^{-9}$ cm/W given that input irradiance was $6.8GW/cm^2$ and the output peak irradiance in the UV is $>2.5GW/cm^2$ at 2.2mm beam diameter. The group velocity indices were 1.724 and 1.905 for the green and UV respectively. The group delay dispersion is dramatically higher in green to UV than IR to green at $139.5fs^2/mm$ and $447.4\ fs^2/mm$ respectively for green and UV. Absorption was set to 2% and 3%. The d_{eff} was 1.73(pm/V). The first crystal was 6x6x1mm BBO. The input pulse energy was 160uJ and 390 fs pulse duration (Figure 7.28). Thermal gradient distortions were not taken into account which can be a large phase detuning factor in fourth harmonic generation. The resulting calculations predict an output pulse energy of 62.8uJ at 262nm and 76.2uJ at

262 nm, and a peak irradiance of 2.84 GW/cm^2 (Figure 7.28). The experimentally achieved value was 4.0W average power resulting in 40uJ at 262nm on the first full input energy test. This results in a difference with our model calculations of 36%.

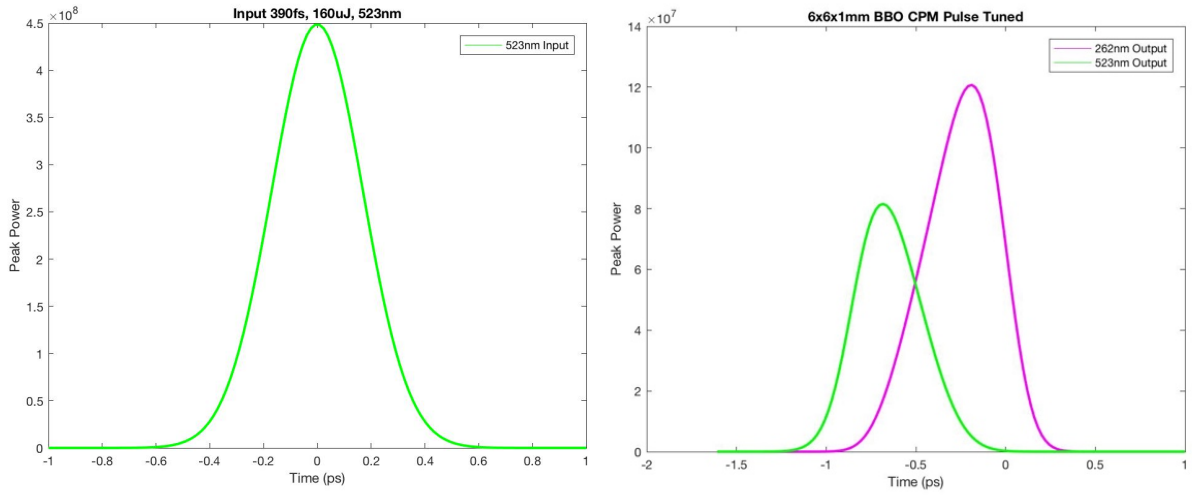

Figure 7.26 Left: Input 2ω. FWHM 390fs, 160 uJ, 523 nm 410 MW peak power incident on a 6x6x1.0 mm Type I BBO. Right: Output 4ω (purple) and residual fundamental pulse (green) 523nm pulse. Beam input FWHM = 2.2 mm

The BBO crystal was used four times with ~2-minute durations at 160uJ input pulse energy from the second harmonic during the first experiment. On the second experiment the output power had dropped to 3.8W. The same crystal was run for 4 separate, 2-minute full power runs. On the third experiment the power had dropped to 3.5W and bright orange specs started to form within the crystal and the coatings. These orange specs were, in fact, color centers that had formed and were visible to the naked eye. As the density of color centers increased the power output in the UV dropped as well as the green.

1.5mm BBO

We next ran a 1.5 mm a thick BBO crystal to compare to the 1.0 mm results. With the 1.5mm crystal, dispersion and walk-off again becomes significant enough to start the generation of a foot (Figure 7.29). The same parameters went into calculating the

conversion plots for the 1.5mm as the 1mm BBO. The resulting peak power is slightly decreased due the dispersion and walk-off at crystal lengths longer than 1mm.

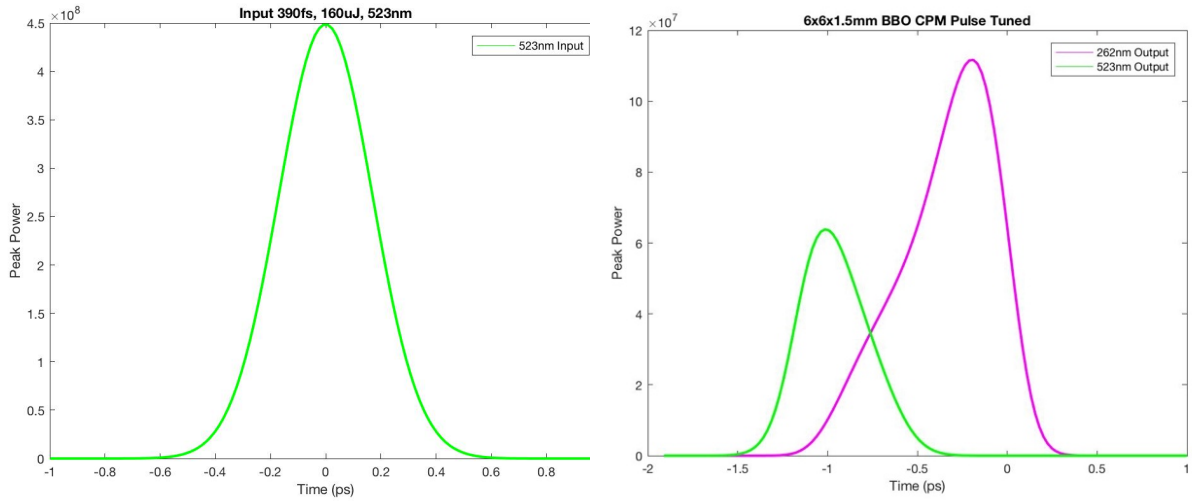

Figure 7.27 Left: Input 2ω. FWHM 390 fs, 160 uJ, 523 nm 410 MW peak power incident on a 6x6x1.5 mm Type I BBO. Right: Output 4ω (purple) and residual fundamental pulse (green) 523nm pulse. Beam input FWHM = 2.2 mm

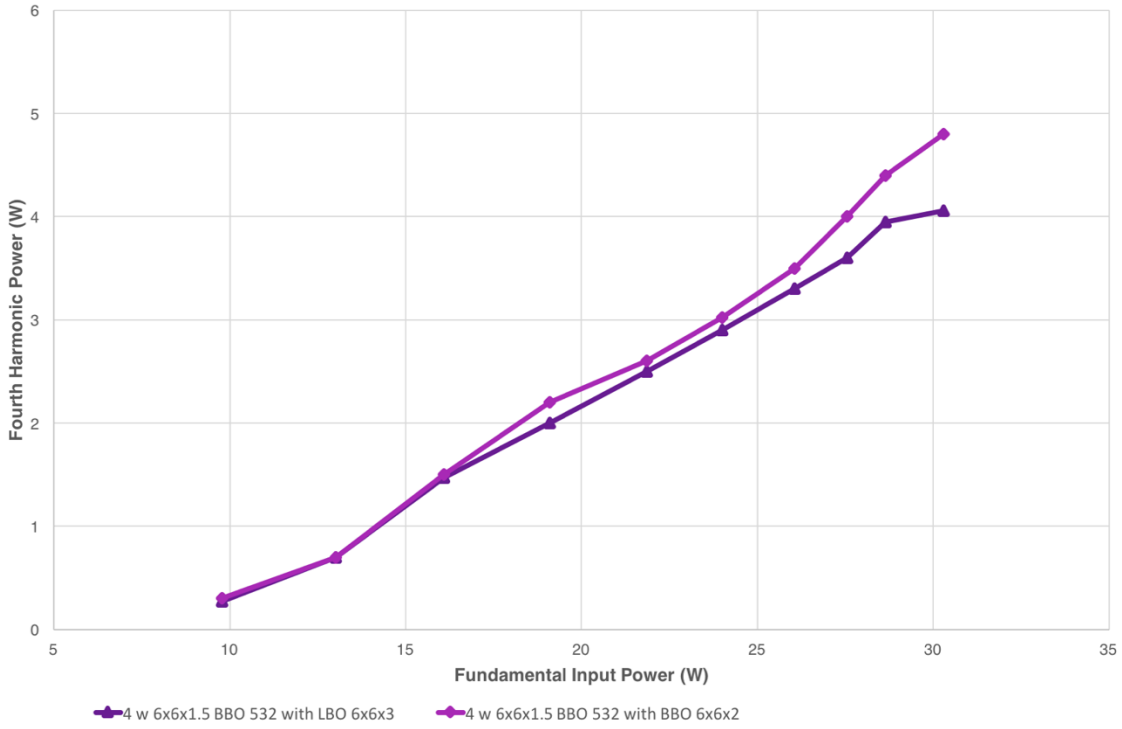

Figure 7.28 Measured Fourth Harmonic Output vs Fundamental (1ω) input FWHM 390 fs and Pulse Repetition Frequency = 100 kHz

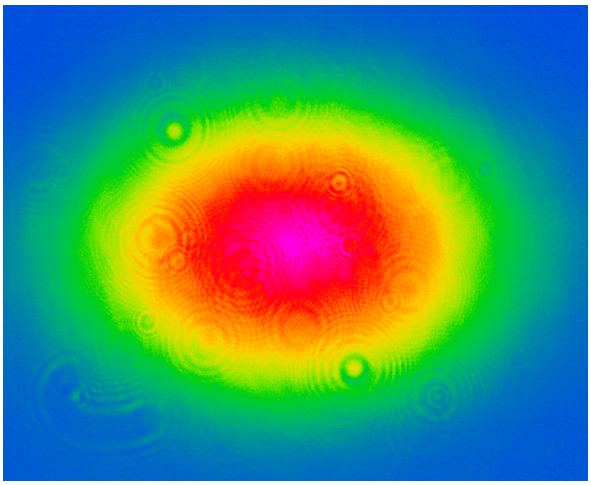

Figure 7.29 Fourth Harmonic beam profile at full power (>5 W at 262 nm). The ellipticity is expected to occur due to increased walk-off between the 2nd and 4th harmonics compared to that of the fundamental and second harmonic. Note the input 2nd harmonic beam is slightly less elliptical. Spots are dust on diagnostic optics.

Both crystals enable an average pulse energy to be maintained above 50 microjoules and an average power of >5 W. No autocorrelation experiments were performed to directly measure the UV pulse duration. Theoretically the 1.5mm BBO crystal results in 7.1W of average power at 100kHz with a peak irradiance of 2.46GW/cm^2.

The same limitations observed in 1mm BBO were seen in 1.5mm BBO. Bright orange color centers formed quickly with extended use. 1.5mm BBO was used for 10 experiments at full input second harmonic power. This time each experiment was run for single 5 minute intervals. The first run of the BBO crystal resulted in 5.3W of average power. With each successive experiment the crystal UV output dropped by ~0.15W resulting in a tenth experiment run of 3.7W output power in the UV. This is consistent with the data observed from Kei Takachiho et al. Color center formation again increased with decreasing output power that was visible to the naked eye. The observation of color center formation indicates that the peak power is indeed far above 100MW/cm^2 for two-photon absorption in BBO. (cite tpa papers) This results in very rapid BBO degradation. These were not the only factors driving conversion efficiency down. At energies above

100uJ the BBO began to exhibit a white glow at the center with trailing orange Gaussian profile. This is the onset of continuum generation and severe self-phase modulation.

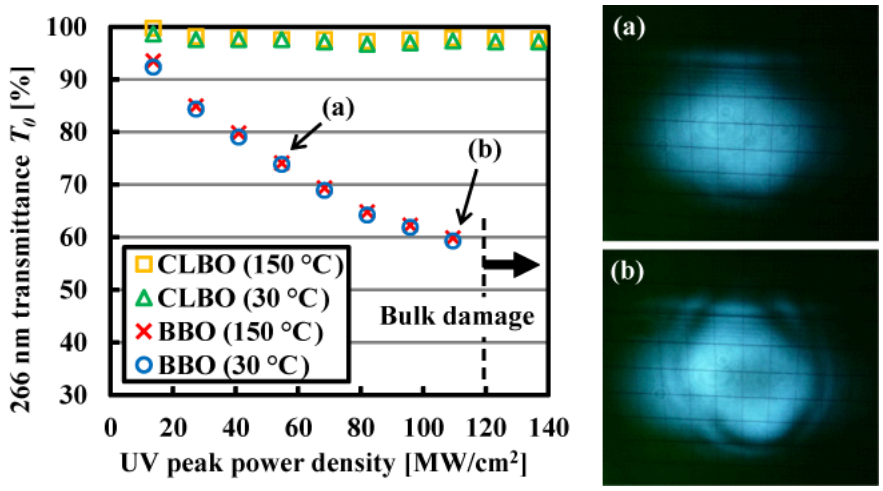

Figure 7.30 Left: UV peak power density dependence of 266nm transmittance for CLBO and BBO. Right: UV beam transmitted through BBO at (a)55 MW/cm^2 and (b)110MW/cm^2 (72)

Continuum and Raman generation was observed through the coatings and the BBO crystal itself. This also led to a reduction in conversion efficiency that was not included in model. Color center creation resulting in thermal distortion and absorption combined with continuum generation to reduce the conversion efficiency from 523 to 262 nm.

The UV pulses are so intense (>2.5GW/cm^2) at 2.2mm that the UV exhibited continuum and Raman generation in the coatings of the harmonic splitters and ALL transmissive optics downstream. A beam sampler was placed for 10% split off for power measurements. The sampler was UV-grade fused silica AR coated for 262nm. The UV beam was so intense, supercontinuum generation extending from 200 to over 800 nm was exhibited through the UV grade fused silica beam sampler (Figure 7.31, 32).

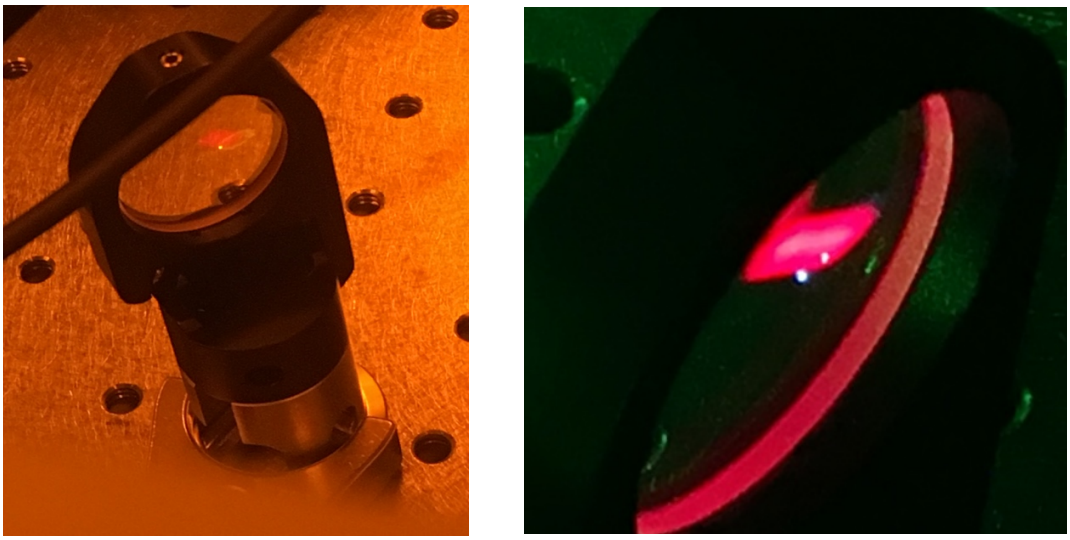

Figure 7.31: Red glow from Raman and Continuum Generation and Two-Photon Fluorescence

The first image above shows the beam sampler at low power 0.11W of UV. The red in the center is the onset of continuum generation due to the two-photon ionization of the fused silica. The yellow ring that forms on the edges is Raman generation being exhibited in the coating of the beam sampler. The next image above on the right is is 1W of UV power. The continuum becomes much brighter white at the center trailing off blue and then into red. The Raman generation no longer is visible to the naked eye and is flooded by the continuum exhibited by the fused silica.

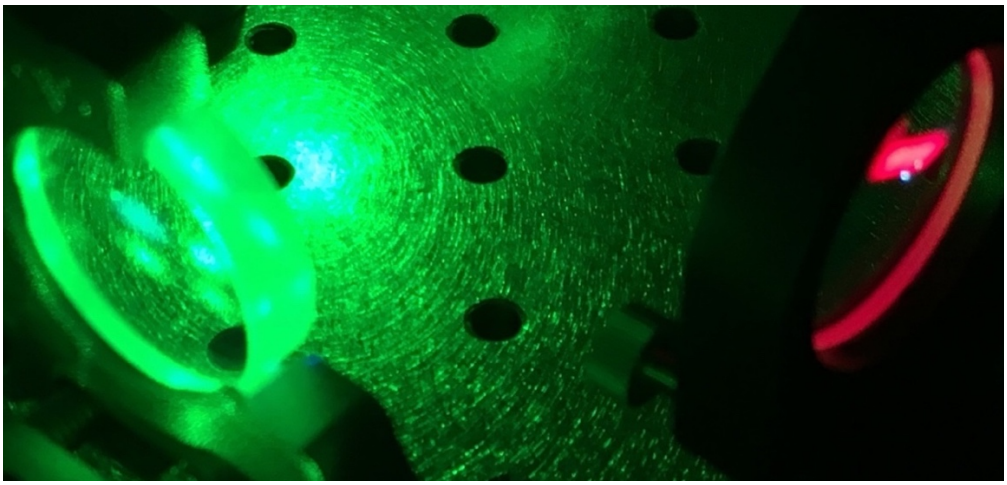

Figure 7.32: Passage of the UV light through fused silica optics at 1W

The above image shows the UV beam being turned 90^{o} by a harmonic beam splitter that passes the residual 1% after the first turn beam splitter. The UV is so intense enough that it forms a blue Gaussian profile on the UV-green beam splitter from CVI optics which is more distinct in the image below. The above image shows the continuum generation at 2W of UV power. The image below is at 4W of average UV power. The onset of white light super continuum from fused silica is now visible to the naked eye.

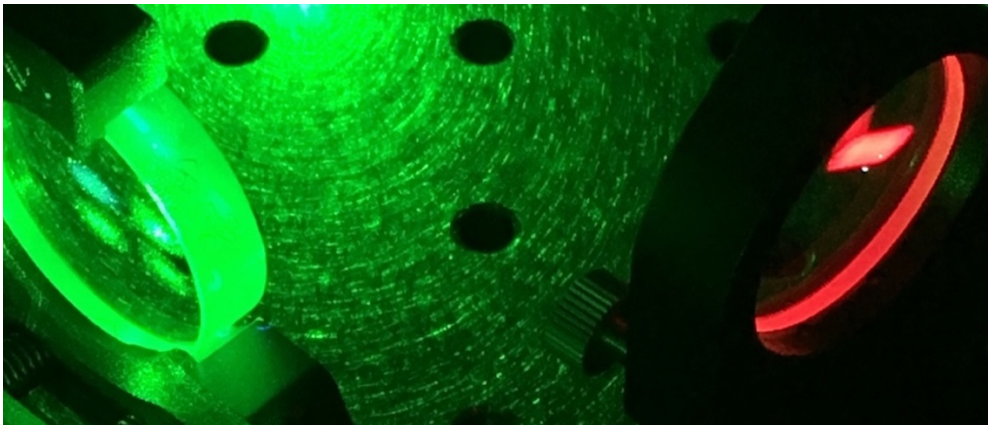

Figure 7.33: Passage of the UV light through fused silica optics at 4W

Figure 7.34 Supercontinuum conical emission in fused silica. $1.21 \times 10^{12} W/cm^2$. 40fs pulses at 805nm and 3mJ. This is consistent with the emission observed in our experiments but with UV light.

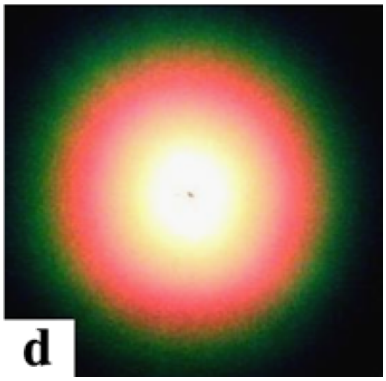

Due to the observation of super continuum generation through fused silica, an Nd:YAG laser crystal was placed in the beam path in two configurations. One configuration allowed for propagation down the long axis of the crystal with a collimated beam. The other configuration allowed for filamentation to occur through Nd:YAG. The

below images show the beam passing through the Nd:YAG laser crystal. The first image is at 0.11W of input UV.

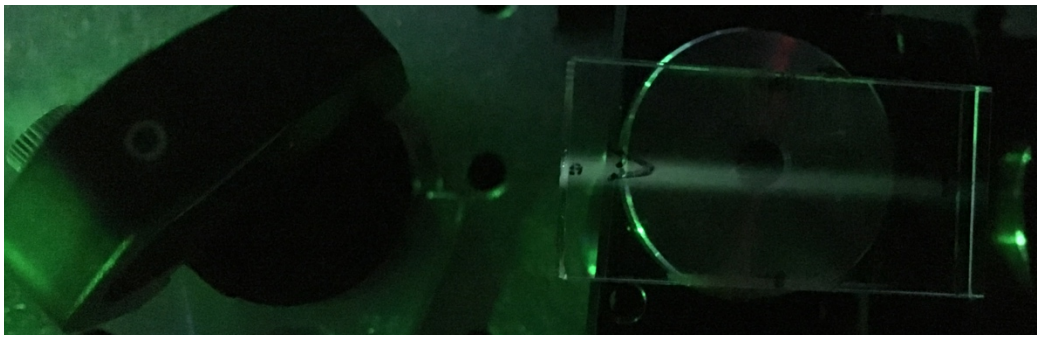

Figure 7.35 Onset of White light supercontinuum at 0.11W of UV

The power was then increased then to 4W of UV. The first image below shows the collimated beam passing through the long axis of the Nd:YAG laser crystal. The YAG exhibits incredibly bright broadband white light super continuum.

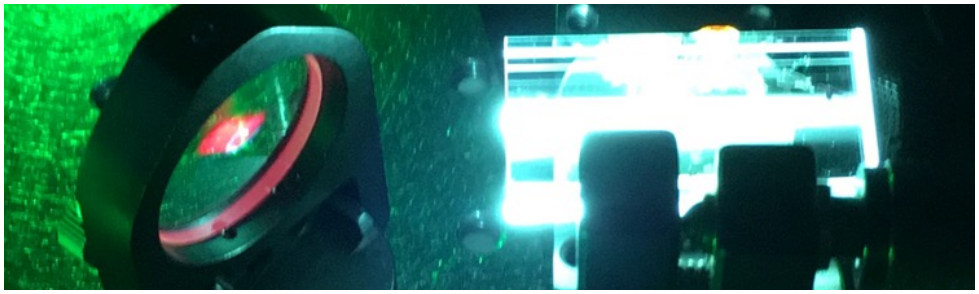

Figure 7.36 White light supercontinuum generation at 4W of UV.

At the center of the YAG, UV filaments are formed and are partially reflected back at the beam sampler which displays the signature of UV filaments. The reflected beam profile is white on the edges with a bright white peaked ~150um FWHM center. This is indicative of UV filamentation (80,81). Next the UV beam was focused in air using a 1m focal length lens. The beam collapsed to ~150um at 95cm and maintained the tight diameter for 10cm. A tight hole remained at the size of ~150um while the outer beam continued to disperse. This was maintained for 45cm until the filaments had lost enough energy and

the hole at the center of the beam became uniform again. The YAG was placed adjusted to 80cm to allow for filamentation through the YAG to occur.

As the crystal was walked through the focus, the filament plasma channel became clearer in the YAG. The filaments maintained a tight, white 150um diameter profile at distances of 20cm past the focus while propagating through the YAG. The filaments stayed concentrated with small deviation from the core of the beam even at 2m past the focus. The image below shows the beam profile 2m after the YAG being placed at 80cm. Its clear the peak intensity is still maintained at long distances well after the focus. These experiments ultimately damaged the YAG crystal. The filaments created burned out channels through the YAG that appear as tight brown lines that extended starting from 5mm into the crystal and extend throughout to the other end. The rings at the center of the image are indicative of filamentation through the YAG crystal and through air. (74-80).

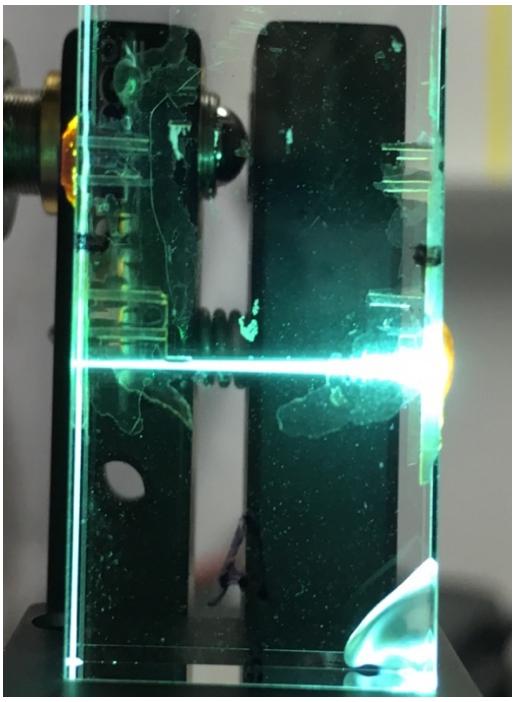

Figure 7.37 UV filaments generated in YAG Laser Crystal

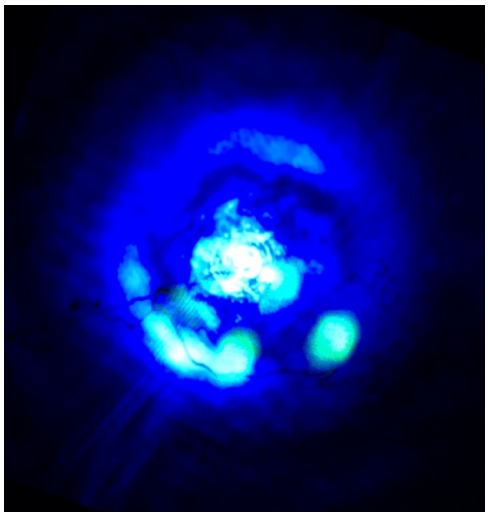

Figure 7.38 Beam profile at 2m after the YAG. Rings at the center indicate UV Filamentation.

The CLBO crystals did not arrive in time to provide experimental measurements. Theoretical calculations for the fourth harmonic generation in 10 mm CLBO are provided Noncritically phase matched CLBO has decreased walk-off and absorption and lower group delay dispersion than BBO. The 2ω input pulse duration is optimized at 600 fs for this crystal length. We achieve this by detuning the mini-compressor to add slight residual third order dispersion to the pulse. Self-phase modulation and two photon absorption terms are taken into model calculations. In CLBO however, the absorption edge is ~180nm vs 190nm in BBO, this allows for two photon absorption of 523 and 262 nm to have a smaller effect than in BBO. Self-phase modulation terms were kept at $1x10^{-15}$ cm^2/W and $1.5x10^{-15}$ cm^2/W. Input irradiance was ~5.6GW/cm^2 with an output fourth harmonic irradiance of 1.22GW/cm^2. The group velocities indices were 1.526 and 1.630 in the green and UV respectively. (16) The group delay dispersion was set to 79.4 fs^2/mm and 240.8fs^2/mm for the green and UV respectively. Absorption in CLBO is kept at 0.02mm^{-1} and 0.03mm^{-1}. The resulting pulse energy is 91uJ resulting in an average power of 9.1W theoretically not including thermal distortion from two-photon absorption at 262nm.

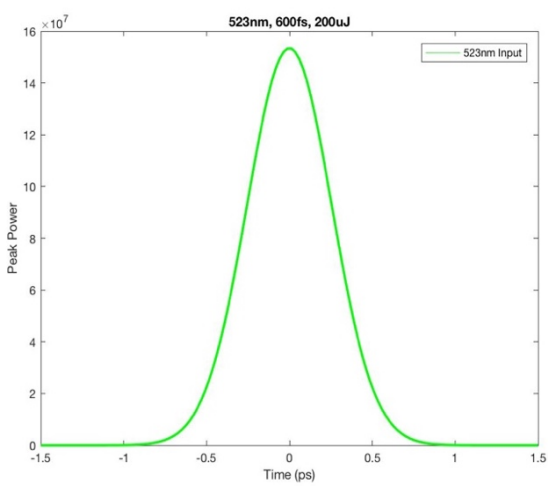

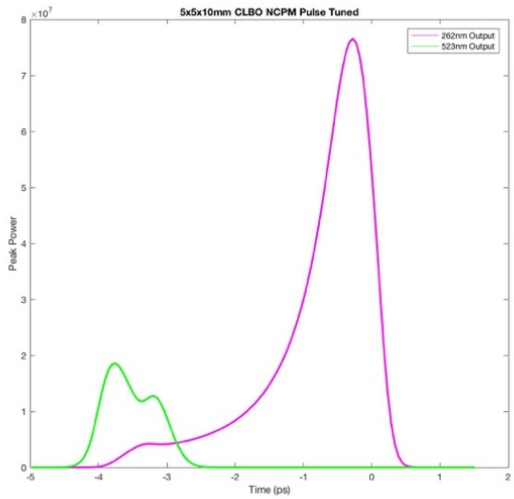

Figure 7.39 Left: Input 2ω. FWHM 600fs, 200 uJ, 523 nm 320 MW peak power incident on a 6x6x10mm CLBO. Right: Output 4ω (purple) and residual fundamental pulse (green) 523nm pulse. Beam input FWHM = 2.2 mm

As seen with the long LBO crystal and 1.5mm BBO, increased crystal length and increased walk-off in the UV generate an energy foot that extends after the pulse. This foot contains up to 40% of the energy in long crystals but does not contriubute to increased peak power at 4ω. Long crystal CLBO generally exhibits ~30% higher conversion efficiency than short crystal BBO. (60-72) CLBO also has the advantage of being kept at ~150^{o}C for non-critical phase matching. Keeping the crystal heated after use could potentially anneal out color center generation in the crystals after each use and will be investigated further.

9. Conclusion

We have developed a compact, diode-pumped fiber based high average and peak power UV femtosecond laser system. The chirped pulse amplification, fiber laser produces >30W average power at 400fs pulse duration. The second harmonic efficiency for maximum peak power (no pulse broadening) was 55%. Non-critically phase matched LBO was shown to produce a higher peak power with lower dispersion and walk-off than critically phase matched BBO. LBO reached 68% SHG conversion efficiency but had to be operated with 600 fsec pulses to prevent dispersive pulse broadening. We achieved a maximum conversion efficiency of 26% from the 2ω (523 nm) to the fourth harmonic at 262 nm with 450 fsec pules. The resulting fourth harmonic output exhibited 5.4 W average power and 120MW per pulse at 100kHz (Figure 8.1). Continuum generation and two-photon absorption were found to be limiting factors in fourth harmonic generation.

To our knowledge, this is the highest peak and average power deep ultraviolet system produced from a fiber-laser system. Further improvement in peak power is possible by compensating for the dispersive broadening in the crystal and/or reducing the pulse duration of the fundamental:

1) A prism pair can be used to provide negative dispersion to cancel the residual group delay dispersion in the conversion crystal. The UV pulse duration could be reduced to nearly ~260fs resulting in an increase of ~50 % in peak power.

2) The fundamental pulse is limited to ~400 fsec by spectral filters used to force operation at 1047 nm. Allowing the system to operate at the peak of the

Yb Silica gain has been shown to prpduce pulses as short as 250 fsec from systems employing the same type of Photonic Crystal amplifiers.

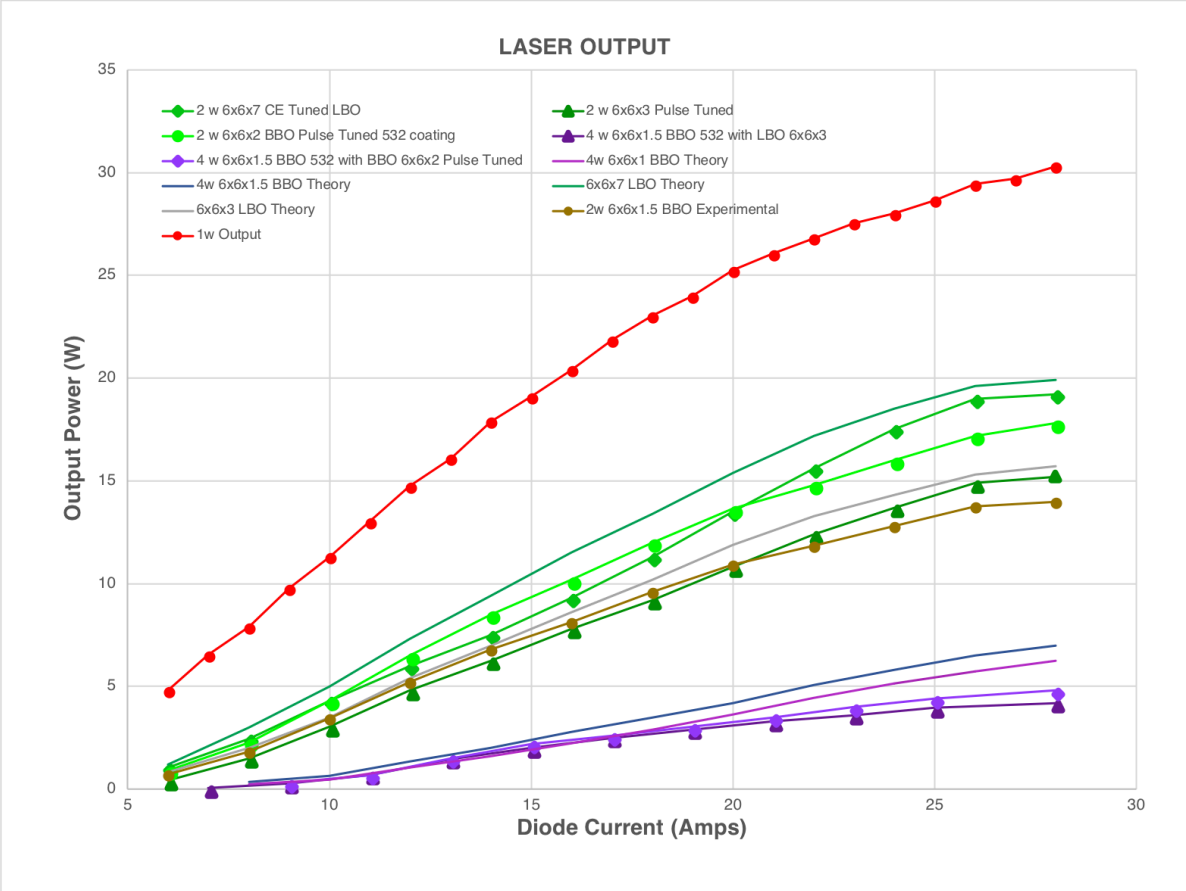

Figure 8.1 Fundamental, second and fourth harmonic output of the 1047 nm fiber laser system at 100 kHz. Beam diameter was 2.2 mm FWHM and the pulse druation varied from 390 to 406 fsec.

References

Introduction

1. Q. Fang, W. Shi, Y. Qin, X. Meng, Q. Zhang, "2.5kW monolithic continuous wave (CW) near diffraction-limited fiber laser at 1080nm," Laser Phys. Lett. 11(2014) 105102 (3pp)

2. M. Perry, T. Ditmire, B. Stuart, "Self-phase modulation in chirped-pulse amplification," Optics Letters, Dec 15, 1994, Vol. 19, No. 24

3. D. Strickland, G. Mourou, "Compression of Amplified Chirped Optical Pulses," Optics Communications, Dec 1, 1985, Vol. 56, No. 3

4. P. Maine, D. Strickland, P. Bado, M. Pessot, G. Mourou, "Generation of Ultrahigh Peak Power Pulses by Chirped Pulse Amplification," Journal of Quantum Electronics, Feb 2. 1988, Vol. 24, No. 2

5. R. Paschotta, J. Nilsson, A. Tropper, D. Hanna, "Ytterbium-Doped Fiber Amplifiers," Journal of Quantum Electronics, Jul 1997, Vol. 33, No. 7

6. P. Russell, "Photonic Crystal Fibers," Science, Jan 2003, Vol 299

7. J. Maeda, M. Yoshida, "Photonic Crystal Fiber Amplifiers," Optical Society of America, OFB1, 2005, 060.2320

8. C. Brooks, F. Teodoro, "Multimegawatt peak-power, single transverse-mode operation of a 100um core diameter, Yb-doped rodlike photonic crystal fiber amplifier," Applied Physics Letters, 89, 111119, Sep 15, 2006.

9. T. Eidam, J. Rothhardt, F. Stutzki, F. Jansen, S. Hadrich, H. Carstens, C. Jauregui, J. Limpert, A. Tunnermann, "Fiber chirped-pulse amplification system emitting 3.8GW peak power." Optical Society of America, 060.2320, Dec 22, 2010.

10. T. Alkeskjold, M. Laurila, J. Weirich, M. Johansen, C. Olausson, O. Lumholt, D. Noordegraaf, M. Maack, C. Jakobsen, "Photonic crystal fiber amplifiers for high power ultrafast fiber lasers," Nanophotonics 2013; 2(5-6): 369-381.

11. H. Chen, J. Lim, S. Huang, D. Schimpf, F. Kartner, G. Chang, "Optimization of femtosecond Yb-doped fiber amplifiers for high-quality pulse compression." Optical Society of America, 060.2320, Dec 10, 2012.

Theory of Nonlinear Optics

12. D. Griffiths, “Introduction to Electrodynamics,” Prentice Hall, 1999
13. P. Lorrain, D. Corson, F. Lorrain, “Fundamental of Electromagnetic Phenomena,” W.H. Freeman and Company, 2000
14. G. Agrawal, “Nonlinear Fiber Optics,” Academic Press, 2013
15. Y.Shen, “Principles of Nonlinear Optics,” Wiley Interscience Publications, 1984
16. A. Smith, “Crystal Nonlinear Optics,” AS-Photonics, 2015
17. W. Koechner, “Solid-State Laser Engineering,” Springer, 2006
18. N. Hodgson, H. Weber, “Laser Resonators and Beam Propagation,” Springer 1999
19. G. Agrawal, “Fiber Optic Communication Systems,” Wiley, 2010
20. B. Saleh, M. Teich, “Fundamentals of Photonics,” Wiley, 2007
21. V. Dmitriev, G. Gurzadyan, D. Nikogosyan, “Handbook of Nonlinear Optical Crystals,” Springer, 1999
22. G. Agrawal, “Optical Pulse Propagation in Doped Fiber Amplifiers,” Physical Review A, Jun 1991, Vol. 44, No. 11

Overview of the System

23. M. Perry, D. Pennington, B. Stuart, G. Tietbohl, J. Britten, C. Brown, S. Herman, B. Golick, M. Kartz, J. Miller, H. Powell, M. Vergino, V. Yanovsky, “Petawatt Laser Pulses,” Optics Letters, Feb 1, 1999, Vol. 24, No. 3
24. T. Ditmire, M. Perry, “Terawatt Cr:LiSrAlF$_6$ Laser System” Optics Letters, March 15, 1993, Vol. 18, No. 6
25. M. Perry, G. Mourou, “Terawatt to Petawatt Subpicosecond Lasers” Science, May 13, 1994, Vol. 264
26. W. White, J. Hunter, L. Woerkom, T. Ditmire, M. Perry, “120-fs terawatt Ti:Al2O3/Cr:LiSrAlF6 laser system,” Optics Letters, August 1, 1992, Vol. 17,

No.15

27. M. Perry, D. Pennington, B. Stuart, G. Tietbohl, J. Britten, C. Brown, S. Herman, J. Miller, V. Yanovsky, “125-TW Ti:Sapphire/Nd:Glass Laser System,” Optics Letters, Feb 15, 1997, Vol. 22, No. 4

28. F. Patterson, R. Gonzales, M. Perry, “Compact 10-TW, 800-fs, Nd:Glass Laser” Optics Letters, July 15, 1991, Vol. 16, No. 14

29. B. Stuart, M. Feit, A. Rubenchik, B. Shore, M. Perry, “Laser-Induced Damage in Dielectrics with Nanosecond to Subpicsecond Pulses,” Physical Review Letters, 74, 2248, March 20, 1995

Seed Oscillator

30. J. Buckley, “High-Energy Ultrafast Ytterbium Fiber Lasers,” Doctoral Dissertation, August 2006

31. F. Ilday, J. Buckley, L. Kuzenetsova, F. Wise, “Generation of 36-femtosecond pulses from a ytterbium fiber laser,” Optical Society of America, Optics Express, December 2003, Vol. 11, No. 26

32. X. Zhou, D. Yoshitomi, Y. Kobayashi, K. Torizuka, “Generation of 28-fs pulses from a mode-locked ytterbium fiber oscillator,” Optical Society of America, Optics Express, May 2008, Vol. 16, No. 10

Pulse Amplification

33. L. Frantz, J. Nodvik, “Theory of Pulse Propagation in a Laser Amplifier,” Journal of Applied Physics, March 1963, Vol. 34, No. 5

34. P. Avizonis, R. Grotbeck, “Experimental and Theoretical Ruby Laser Amplifier Dynamics,” Journal of Applied Physics, 1966, Vol. 37, No. 2

35. H. Chen, J. Lim, S. Huang, D. Schimpf, F. Kartner, G. Chang, “Optimization of femtosecond Yb-doped fiber amplifiers for high-quality pulse compression,” Optical Society of America, Optics Express, May 2012, Vol. 20, No.27

36. J. Zhao, W. Li, C. Wang, Y. Liu, H. Zeng, “Pre-chirping management of a self-similar Yb-fiber amplifier towards 80W average power with sub 40-fs pulse generation,” Optical Society of America, Optics Express, Dec 2014, Vol. 22, No. 26

Second Harmonic Generation

37. K. Kato, "Tunable UV Generation to 0.2325 um in LBO" Journal of Quantum Electronics, July 1990, Vol. 26, No. 7

38. C. Chen, Y. Wu, A. Jiang, B. Wu, G. You, S. Lin, "New nonlinear-optical crystal: LiB3O5," Optical Society of America B 1989, Vol. 6, pp, 616-621

39. S. Velsko, M. Webb, L. Davis, C. Huang, "Phase-Matched Harmonic Generation in Lithium Triborate (LBO)," Journal of Quantum Electronics, Sept 1991, Vol. 27, No. 9

40. Q. Liu, F. Lu, M. Gong, C. Li, D. Ma, "15W output power diode-pumped solid-state lasers at 515nm," Laser Physics Letters 4, No. 1, 30-32, 2007

41. K. Regeleskis, J. Zeludevicus, N. Gavrilin, G. Raciukaitis, "Efficient second-harmonic generation of a broadband radiation by control of the temperature distribution along a nonlinear crystal," Optical Society of America, Optics Express, Dec 2012, Vo. 20, No. 27

42. B. Wu, F. Xie, C. Chen, "Type-1 and Type-2 noncritical phase matching of LiB3O5 crystal," Journal of Applied Physics, Jun 1993, 73 (11)

43. D. Eimerl, "High Average Power Harmonic Generation," Journal of Quantum Electronics, May 1987, Vol –QE23, No. 5

44. F. Xie, B. Wu, G. You, C. Chen, "Characterization of LiB3O5 crystal for second-harmonic generation," Optics Letters, Aug 1991, Vol. 16, No. 16

45. Z. Liu, J. Lin, Z. Whang, C. Chen, M. Lee, "Mechanism for linear and nonlinear optical effects in LiB3O5, CsB3O5, and CsLiB6O10," Physical Review B, July 2000, Vol 62, No.3

46. J. Li, C. Duan, Z. Gu, D. Wang, "First-principle calculations of the electronic structure and optical properties of LiB3O5, CsB3O5 and BaB2O4 crystals," Physical Review B, March 1998, Vol. 57, No. 12

47. A. Borsutzky, R. Brunger, C. Huang, R. Wallenstein, "Harmonic and Sum-Frequency Generation of Pulsed Laser Radiation in BBO, LBO, and KD*P" Applied Physics B, July 1990, 52, 55-62

48. S. Lin, B. Wu, F. Xie, C. Chon, "Phase-matching retracing behavior: New features in LiB3O5," Applied Physics LettersJune 1991, 59(13)

49. J. Zhang, J. Huang, H. Wang, S. Wong, G. Wong, "Second-harmonic generation from regeneratively amplified femtosecond laser pulses in BBO and LBO

crystals," Optical Society of America B, Jan 1998, Vol. 15, No.1

50. I. Begishev, M. Kalashnikov, V. Karpov, P. Nickles, H. Schonnagel, I. Kulagin, T. Usmanov, "Limitation of second-harmonic generation of femtosecond Ti:Sapphire laser pulses." Optical Society of America, Feb 2004, Vol. 21, No. 2

51. X. Peng, L. Xu, A. Asundi, "High-Power efficient continuous wave TEM_{00} intracavity frequency-doubled diode-pumped Nd:YLF laser," Applied Optics Feb 10, 2005, Vol. 44, No. 5

52. A. Dergachev, P. Moulton, "Short-Pulse, High-Repetition Rate, High-Power Nd:YLF MOPA system," Optical Society of America, 140.3480, 2004

53. T. Ukachi, R. Lane, W. Rosenberg, C. Tang, "Measurements of noncritically phase-matched second-harmonic generation in a LiB3O5 crystal," Applied Physics Letters, 1990, 57, 980

54. Y. Ralchenko, F. Jou, D. Kelleher, A. Kramida, A. Musgrove, J. Reader, *NIST Atomic Spectra Database,* National Institute of Standards and Technology, Aug 2000, [Online]

55. G. Boyd, D. Kleinman, "Parametric Interaction of Focused Gaussian Light Beams," Journal of Applied Physics, 1968, 39, 3597-3639

56. G. Tamosauskas, G. Beresnevicius, D. Gadonas, A. Dubietis, " Transmittance and phase matching of BBO crystal in the 3-5um range and its applications for the characterization of mid-infrared laser pulses," Optical Materials Express, May 2018, (160.4330) #325788

UV Harmonic Generation

57. Y. Mori, I. Kuroda, S. Nakajima, T. Sasaki, S. Nakai, "New Nonlinear Optical Crystal: Cesium Lithium Borate," Applied Physics Letters, 1995, 67, 1818

58. Y. Mori, I. Kuroda, S. Nakajima, T. Sasaki, S. Nakai, "Nonlinear Optical Properties of Cesium Lithium Borate,"

59. Y. Yap, S. Kida, T. Aoyama, Y. Mori, T. Sakai, "High Power Solid State UV Laser by means of CLBO crystal and its application for pulsed laser deposition," *CLEO*, 1998, 147, CTuM25

60. H. Xuan, H. Igarashi, S. Ito, C. Qu, Z. Zhou, Y. Kobayashi, "High-Power, Solid-State, Deep-Ultraviolet Laser Generation." Applied Sciences, Feb 2018, 8, 233

61. W. Zhou, Y. Mori, T. Sakai, S. Nakai, "High-efficiency intracavity continuous wave ultraviolet generation using crystals CLBO, BBO, LBO," Optics

Communications, Feb 1996, 123, 583-586

62. G. Bhar, P. Kumbhakar, U. Chatterjee, A. Rudra, A. Nagahori, "Widely tunable deep ultraviolet generation in CLBO," Optics Communications, Mar 2000, 176, 199-205

63. S. Kumar, J. Casals, J. Wei, M. Zadeh, "High-power, high-repetition-rate, performance characteristics of BBO for single-pass picosecond ultraviolet generation at 266nm," Optics Express, Oct 2015, Vol. 23, No. 21

64. Y. Kap, T. Inoue, H. Sakai, Y. Kagebayashi, Y. Mori, T. Sakai, K. Deki, M. Horiguchi, "Long-term operation of CLBO at elevated crystal temperature," Optics Letters, Jan 1998, Vol 23. No.1

65. Y. Kap, Y. Mori, S. Haramura, A. Taguchi, K. Nishijima, T. Inoue, A. Miyamoto, H. Sakai, Y. Kagebayashi, T. Sakai, "Stable operation temperature of CLBO crystal for laser frequency conversion at elevated temperature." *CLEO*, 1997, CFM4

66. L. Sharma, H. Daido, S. Nakai, Y. Kato, T. Zhang, Y. Mori, T. Sakai, "UV Generation of ultrashort Nd:Glass Laser Pulses," *CLEO*, 1997, CMF5

67. D. Gerstenberger, T. Trautmann, M. Bowers, Noncritically phase-matched second harmonic generation in cesium lithium borate," Optics Letters, July 2003, Vol. 28, No. 14

68. T. Kojima, S. Konno, S. Fujikawa, K. Yasui, K. Yoshizawa, "20W ultraviolet-beam generation by fourth-harmonic generation of an all-solid-state laser," Optics Letters, Jan 2000, Vol. 25, No. 1

69. D. Brown, M. Withford, "High-average-power (15-W) 255nm source based on second harmonic generation of a copper laser master oscillator power amplifier system in cesium lithium borate," Optics Letters, Dec 2001, Vol. 26, No. 23

70. M. Muller, A. Klenke, T. Gottschall, R. Klas, C. Rothhardt, S. Demmler, J. Rothhardy, J. Limpert, A. Tunnerman, "High-average-power femtosecond laser at 258nm," Optics Letters, Jul 2017, Vol. 42, No. 14

71. O. Novak, H. Turcicova, M. Smrz, T. Miura, A. Endo, T. Mocek, "Picosecond green and deep ultraviolet pulses generated by a high-power 100kHz thin-disk laser," Optics Letters, Nov 2016, Vol 41. No. 22

72. K. Takachiho, M. Yoshimura, Y. Takahashi, M. Imade, T. Sasaki, Y. Mori, "Ultraviolet laser-induced degradation of CLBO and BBO," Optical Materials

Express, March 2014, Vol. 4, No.3

73. G. Kurdi, K. Osvay, J. Klebniczki, M. Divall, E. Divall, A. Peter, K. Polgar, J. Bohus, "Two-photon-absorption of BBO, CLBO, KDP, and LTB crystals," Optical Society of America, 2005, 160.4330, MF18

74. S. Wu, G. Blake, S. Sun, H. Yu"Two-photon absorption inside BBO crystal during UV nonlinear optical conversion," SPIE Proceedings, Mar 2000, Vol. 3928

75. V. Kandidov, S. Shlenov, O. Kosareva, "Filamentation of high-power femtosecond laser radiation," Quantum Electronics, 2009, 39(3) 205-228

76. S. Tzortzakis, D. Papazoglou, J. Zergioti, "Long-range filamentary propagation of subpicosecond ultraviolet laser pulses in fused silica," Optics Letters, March 2006, Vol. 31, No. 6

77. J. Kasparian, J. Wolf, "Physics and applications of atmospheric nonlinear optics and filamentation," Optics Express, Jan 2008, Vol. 16, No.1

78. L. Zhang, T. Xi, Z. Hao, "Multiple refocusing of femtosecond filamentation in air, Experiment and simulation," Optik Elsevier GmbH, 2017,144 70-75

79. Z. Liu, X. Lu, Q. Liu, S. Sun, X. Liu, B. Ding, B. Hu, "Ultraviolet conical emission produced by high-power femtosecond laser pulse in transparent media," Applied Physics B, Jul 2012, 108: 493-500

80. C. Lu, Y. Tsou, H. Chen, B. Chen, Y. Cheng, S. Yang, M. Chen, C. Hsu, A. Kung, "Generation of intense supercontinuum in condensed media," Optica, Dec 2014, Vol.1 No.6

81. A. Dubietis, G. Tamosauskas, R. Suminas, V. Jukna, A. Couairon, "Ultrafast supercontinuum generation in bulk condensed media," Physical Review Journals, Jun 2017, 42.65.Jx, 42.65.Re